Multiscale modelling and measurements for powder compaction.

Choi, Jinnil Lee

Multiscale Modelling and Measurements for Powder Compaction

by

Jinnil Lee Choi B.Eng. (Hons.)

Thesis submitted to the University of Wales Swansea
for the degree of Doctor of Philosophy

2008

School of Engineering
University of Wales Swansea

Declaration

This work has not previously been accepted in substance for any degree and is not being concurrently submitted in candidature for any degree.

Signed (candidate): _____

Date: 06 / FEB / 2008

Statement 1

This thesis is the result of my own investigations, except where otherwise stated. Other sources are acknowledged by the use of explicit references. A bibliography is appended.

Signed (candidate): _____

Date: 06 / FEB / 2008

Statement 2

I hereby give consent for my thesis, if accepted, to be available for photocopying and for inter-library loan, and for the title and summary to be made available to outside organisations.

Signed (candidate): _____

Date: 06 / FEB / 2008

Acknowledgements

I would like to thank the following people and organisations, who have helped me in the work undertaken for this thesis:

First and foremost,

Professor D.T. Gethin, my Supervisor, for his invaluable guidance, unlimited support, and encouragement;

Dr. T.V. Korochkina and Dr. C.J. Wright for their help and support, especially in AFM experiments;

Mr. P. Matthews for his continuous help and support with the experimental program;

The Technical staff at the Mechanical Engineering workshop for helping and making sure my design was successfully manufactured;

Mr. Kyung-Jai Lee and Dr. Eui-Kwan Koh, Korea Basic Science Institute, Seoul, for their help and support for AFM experiment, and allowing me to use the equipment on such a short notice;

And lastly, my parents for giving me the opportunity and their endless support and encouragement throughout.

Summary

In this thesis, experimental investigations into friction between powder and die (macro scale), numerical modelling of a micro scale friction measurement method by atomic force microscopy, and numerical modelling of compaction and friction processes at a micro scale are presented.

The experimental work explores friction mechanisms by using an extended sliding plate apparatus for low load running over a longer distance to measure frictional characteristics between powder compact and target surface with variation of powders, loads, surface finishes, and speed. The behaviour of the static and dynamic friction of both ductile and brittle powders was explored and important factors in the friction mechanisms were identified with regard to particle size, particle shape, material response (ductile or brittle), and surface topography.

Numerical modelling of AFM experiment is presented with the aim of exploring friction mechanisms at the micro scale. As a starting point for this work, comparisons between FE (finite element) models and previously reported mathematical models for stiffness calibration of cantilevers (beam and V-shaped) are presented and discrepancies highlighted. A colloid probe [1] model was developed and its normal and shear interaction were investigated exploring the response of the probe accounting for inevitable imperfections in its manufacture. The material properties of the cantilever had significant impact on both normal and lateral response, even local yielding was found in some areas. The sensitivity of the response in both directions was explored and found that it was higher in normal than in lateral. In lateral measurement, generic response stages were identified, comprising a first stage of twisting, followed by lateral bending, and then slipping. This was present in the two cantilever types explored (beam and V-shaped). Additionally, an emulation model was designed to explore dynamic sensitivity by comparing the simulation of a hysteresis loop with previously reported experiment

[1] A colloid probe comprises a plain cantilever on which a particle is adhered.

and the results show good agreement in response pattern. The ability to simulate the scan over an inclined surface representing the flank of an asperity was also demonstrated.

The compaction stage of the experiment was numerically modelled using a combined discrete and finite element modelling scheme to explore compaction mechanisms further. A number of simulation factors and process parameters were investigated. Comparisons were made with previously published work showed reasonable agreement and the simulations were then used to explore process response to the range of particle scale factors. Models comprising regular packing of round particles exhibited stiff response with high initial density. Models with random packing were explored to account for a more practical initial density and this was confirmed.

Numerical modelling of the compaction stage was extended to account for the shearing stage of the extended sliding plate experiment. This allowed micro scale simulations of the friction mechanisms seen within the experimental programme. The frictional response with similar stress level in the normal direction as reported for the experiment was first emulated and explored and qualitative agreement was achieved showing similar pattern. The factors identified from the experiments were considered and explored on smooth and rough surfaces highlighting each effect. It was confirmed that the rough surface clearly leads to higher friction coefficient since it accounts for both plain friction and topographical effects and the average stress distribution increased against the restraining die wall when the rough surface was introduced for the model with round regular packing of particles. Random packed models again showed a better reflection of the experimental conditions. A wider distribution of stress was observed because of the further rearrangements. Interlocking was observed for the models with irregular shaped particles on a rough surface, which led to increase in normal stress on the top punch. This would lead to dilation in the case where a punch was force level controlled as for the experiment.

Table of Contents

List of Figures

List of Tables

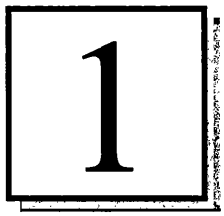

INTRODUCTION

1.1 POWDER COMPACTION MANUFACTURING

The powder compaction process can be described as the forming of any type of powder material by compaction in a container into a desired single cohesive mass.

Powder compaction is widely used to manufacture products with different materials, some of which are itemised in Table 1.1.

Products	Materials
Cutting tools and wear parts	Hard metals
Filters and oil-retaining bearings (self-lubricating bearings)	Porous materials
Heavy-duty applications	Composite (eg. copper, iron) powders
Electrical components	Carbon powders
Magnetic components	Metal powders
Structural parts	Metal powders (mainly iron based)
Wear and corrosion resistant products	Ceramic powders
Pharmaceutical tablets	
Food products (eg. sweets, stocks)	

Table 1. 1 Examples of Products from Powder Compaction

There are a number of reasons for using powder compaction to make engineering components. For some components, it is either the only route to produce or it is widely used for economic purposes. Respective examples are

cutting tools and structural parts. Powder compaction is a continually and rapidly evolving technology where it is a highly developed method of manufacturing reliable components. The European Market alone has an annual turnover of six billion Euros, with annual worldwide metal powder production exceeding one million tonnes [EPMA website, 2006]. The powder compaction industry is growing largely because of the cost saving aspect when compared with other metal forming processes such as casting and forging. This is because powder metallurgy generally uses more than 95 percent of the starting raw material in the finished part. It is also suited to high volume component production requirements and has long-term performance reliability in critical applications. Additionally powder metallurgy consumes less energy compared with forging and machining, reducing the number of process steps.

Although powder compaction manufacturing can produce components more quickly than other methods since it requires minimal need of further processing steps, the equipment for forming and sintering represent high capital investment.

1.2 MANUFACTURING PROCESS OF POWDER COMPACTION

The whole manufacturing process of powder metallurgy is shown in flow chart Figure 1.1 from [EPMA website, 2006].

There are four main processes, which are:

- Powder Preparation (including Mixing)
- Forming
- Sintering
- Optional Manufacturing and Finishing Steps

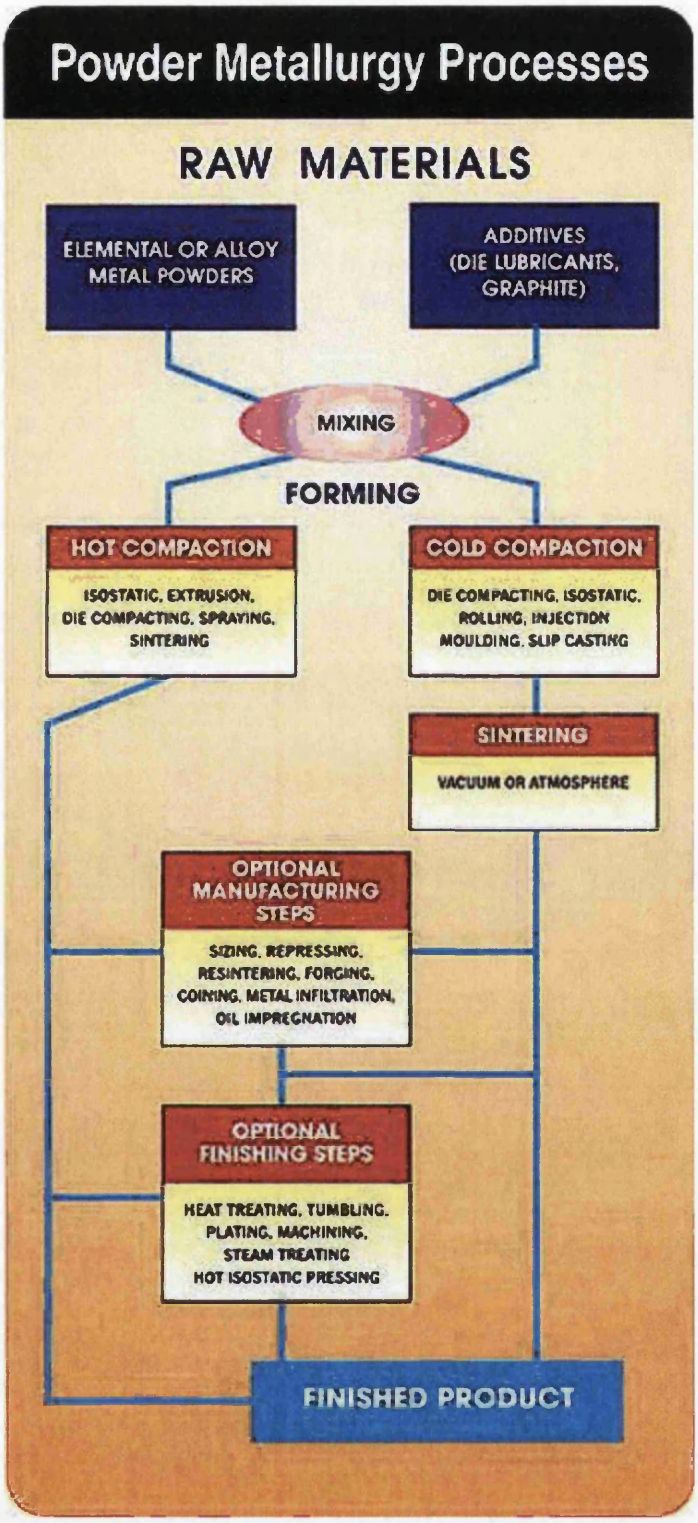

Figure 1. 1 The Processes of Powder Metallurgy [EPMA website, 2006]

1.2.1 Powder Preparation

There are many ways for metals to be produced in powder form as seen on Figure 1.1. The most popular methods for metal powders are solid state reduction, electrolysis, and atomisation. The solid state reduction is mainly used for iron powders and electrolysis for copper powders, where atomisation of molten metal could be used for range of metal powders. Once the raw materials are in powder form, additives such as die lubricants and binders are added to aid cohesion of the powder in the green state. Adding lubricant reduces the friction between powder and tooling promoting the achievement of uniform density throughout the compact and reducing ejection loads that will reduce the likelihood of cracking in some part shapes. This stage in powder preparation is facilitated by mixing, where the main purpose is to produce a homogeneous system.

1.2.2 Forming

The powder mixture is loaded into a rigid die and pressure applied through a punch system, which results in a compact. The issue of importance before applying pressure is die filling, where good flow is essential for filling the powder into the die. Compaction is a critical process where the level and uniformity of the final density determines the final shape and mechanical properties of the compact. In order to continue to the next stage, sintering, the compact is required to be strong enough to withstand ejection from the die. This unsintered compact with sufficient cohesion is also referred as a green compact.

1.2.3 Sintering

Sintering is a heat treatment of a compact in order to increase bonding of particles and provide sufficient strength to the compact to sustain its working load. This is conducted in a protective atmosphere, at a temperature below the melting point of the dominant material that is present.

1.2.4 Optional Manufacturing and Finishing Steps

For some powders, some further steps are required to obtain desired product such as sizing, coining, forging, machining, impregnation, infiltration and plating.

1.3 AIM OF THE WORK

Powder compaction manufacturing is a continually and rapidly evolving industry involving most metallic and alloy materials, and a wide variety of shapes. However, this evolution has led to the requirement for a more thorough understanding of the process.

Numerical modelling offers many advantages, such as enabling further understanding of the compaction process and providing insight for the design of new components. However, in order to obtain high accuracy from the modelling, the quality of powder characteristics becomes essential. The powder properties include yield and friction data.

The interaction between powders and the tooling is identified through coefficient of friction. Friction has been investigated previously for various die materials and finishes, but in order to explore its behaviour further for low loads and for extended sliding distances, a sliding plate apparatus was designed and experiments conducted as set out in Chapter 3. This experiment yields friction at a global level, less information is available about friction at the particle scale and experimental equipment is becoming available to conduct experiments at this level.

Atomic force microscopy (AFM) represents a possible route for friction measurement at the particle scale. It is already used extensively for investigating surfaces topography and material surface development, principally adhesion at the particle scale. The AFM belongs to a family of non contact measurement devices that resolve to the nano scale. Others include the Scanning tunnelling microscope (STM) which was invented in 1981 by G. Binnig and H. Rohrer [Molecular Imaging website, 2005]. STM is limited to imaging conducting surfaces, but the AFM is a more versatile tool enabling surface and surface material studies. Its ability to image the topography of the surface as well as a measuring force at the nano scale has led to unique insights into surface studies. Principally, the AFM consists of a tip attached to a cantilever, which performs a raster scan over the surface. The changes in displacement are captured by a photo-diode and converted into surface topography and force measurements. Lateral force microscopy (LFM) uses a four segments photo-diode to enable measurement of the torsion of the cantilever. Chemical force microscopy (CFM) combines LFM with treatments to the tip to customise its interaction with the sample. The research in Chapter 4 will focus on the issue of calibration of the AFM cantilever and identify the factors that may affect the force measurements in both normal and lateral force by application of numerical modelling. Emphasis will be placed on lateral response, because, to date, this has received limited attention and presents a significant challenge to obtain a realistic calibration from which, for example, inter-particle friction may be estimated.

Finally, numerical models have been designed for the powder compaction process to explore existing mechanisms at the particle scale rather than the continuum level. Chapter 5 focuses on the pressing stage of the compaction and explores the impact of particle scale data on the compaction response of the particle assembly.

The numerical models for compaction process were extended to include the shearing stage to explore frictional mechanisms at the particle scale in Chapter 6, through emulation of sliding plate experiment reported in Chapter 3.

1.4 LAYOUT OF THE THESIS

The layout of the thesis following the current chapter is as follows:

Chapter 2 Literature Review

This chapter includes a review of the most relevant work for friction measurement methods (macro scale), compaction and friction modelling, and AFM modelling (micro scale).

Chapter 3 Macro Scale Friction Measurement Method

In this chapter experimental work with the newly designed extended sliding plate apparatus is introduced. Consistency, control stabilisation, and data reduction issues are explored for the equipment. Comparisons with previous work are also included.

Chapter 4 Atomic Force Microscopy Modelling

In this chapter, the calibration of cantilevers used in AFM experiments is explored by introducing numerical models to compare with mathematical calibration methods reported previously. Modelling capable of simulating the friction measurement process for AFM is designed and factors of importance explored.

Chapter 5 Compaction Modelling

This chapter shows modelling of the compaction stage of the experimental work for friction measurement in Chapter 3. Compaction modelling provides further understanding of compaction process and mechanisms in existence at the particle scale are explored by various case studies.

Chapter 6 Friction Modelling

This chapter is continuous from the compaction modelling chapter, where friction measurement via the shear plate experiment is numerically modelled as an extension to the compaction stage reported in Chapter 5. Friction mechanisms are explored further to confirm and identify issues of importance found in Chapter 3.

Chapter 7 Conclusions and Recommendations

This chapter shows conclusion of the work presented and recommendations for future work in the area are suggested.

2

LITERATURE REVIEW

2.1 INTRODUCTION

Powder compaction has been considered by many researchers focusing on experimental work, modelling or a combination of both to understand the mechanisms that exist within this manufacturing process. This work has highlighted the key process parameters, these include:

- Fill Density [Demetry, 1998]
- Material Behaviour [Rowe, 1995]
- Tool Kinematics [PM Modnet, 2002]
- Friction

Each of these has an impact on the density variation through the compact and the forces that are required to compress the powder.

Friction is consistently found to have a significant impact on pressed part quality and motivates the work being reported in this thesis. Friction may be investigated at both micro and macro levels and a review of friction measurement methods at both scales and modelling of powder compaction and friction will be presented in this chapter. To summarise, the literature review investigates the studies in the following areas:

- Friction Measurement Methods (Macro Scale)
- Compaction / Friction Modelling
- Micro Scale Friction Measurement using AFM

2.2 FRICTION MEASUREMENT METHODS (MACRO SCALE)

Two main methods of measuring friction in powder compaction at the macro scale have been investigated and reported in the literature:

- Indirect Friction Measurement
- Direct Friction Measurement

2.2.1 Indirect Friction Measurement

Indirect friction measurement involves the use of uniaxial compaction apparatus instrumented with load cells (instrumented die). Measurement of axial stresses at both top and bottom faces of the compact and radial stress variation over its height are made, where the relationship between shear and radial stress at the die surface are analysed and the coefficient of friction derived.

One of the first works was reported by [Gethin, 1994] in which results of die pressing tests for iron, bronze, ceramic and carbon powders were described. The focus was to investigate the compaction mechanism of a simple bushing part during which a complete force balance was recorded. The results showed progressive increase in force as compaction proceeded which indicated the rearrangement phase of the particles. The effect of applying a lubricant to the powder was also reported. The importance of die wall friction in long compact geometries was highlighted. It also confirmed that friction variation depends on the relationship between radial and axial stress, identifying that this needs to be accurately defined.

The measurement of radial stress in die compaction has been attempted using a number of equipment configurations that can be divided into three types. The first is a thin walled die instrumented with strain gauges to capture hoop strain [Korachkin, 2006], the second is a rigid die that incorporates a liner on which strain is measured at discrete points [Guyoncourt, 2001], and the third is through pins that penetrate the wall of the die and remain flush with it [Cocks, 2006]. The latter allows direct contact between the powder and pressure sensing device.

Experimental results from an instrumented die test are reported in [PM Modnet, 2002]. Different equipment and experimental techniques were used to characterise the yield and friction properties of the powder. These include triaxial, instrumented die, and shear plate apparatus. The results, especially density distribution, from these tests were compared with simulation of the compression stage of the forming process. It was reported that the differences that were highlighted were attributed to equipment type, test procedure, and the powder filling condition for the triaxial tests. The equipment design, in terms of radial stress measurement, rigidity, sample size, and surface finish of the die were all considered to have some influence. The results regarding shear plates will be discussed in the section below for direct measurement method.

[Guyoncourt, 2001] also reports experimental work via development of an instrumented die for obtaining triaxial stress and frictional data. Experiments were completed with three different industrial presses using ferrous, ceramic and tungsten carbide powders. Friction data were found to agree well with measurement made with direct friction measurement equipment. The issue of sensing radial stress was again highlighted and it was concluded that improvement is desirable.

The indirect measurement methods from these studies approximated the actual compaction process closely. However, it is difficult to investigate

understanding of the results observed and the friction mechanisms present. This includes determination of radial stress variation and it is relatively inflexible to allow exploration of all process variables.

2.2.2 Direct Friction Measurement

Direct friction measurement involves measuring the shear force required to slide a target surface against the compact while the normal force is applied and held constant throughout the process. The coefficient of friction between powder and the target surface can be deduced from the ratio between normal force and measured shear force.

A study described in [Strijbos, 1976] reports experiments by a direct friction measurement method in the form of a calliper shear apparatus shown in Figure 2.1.

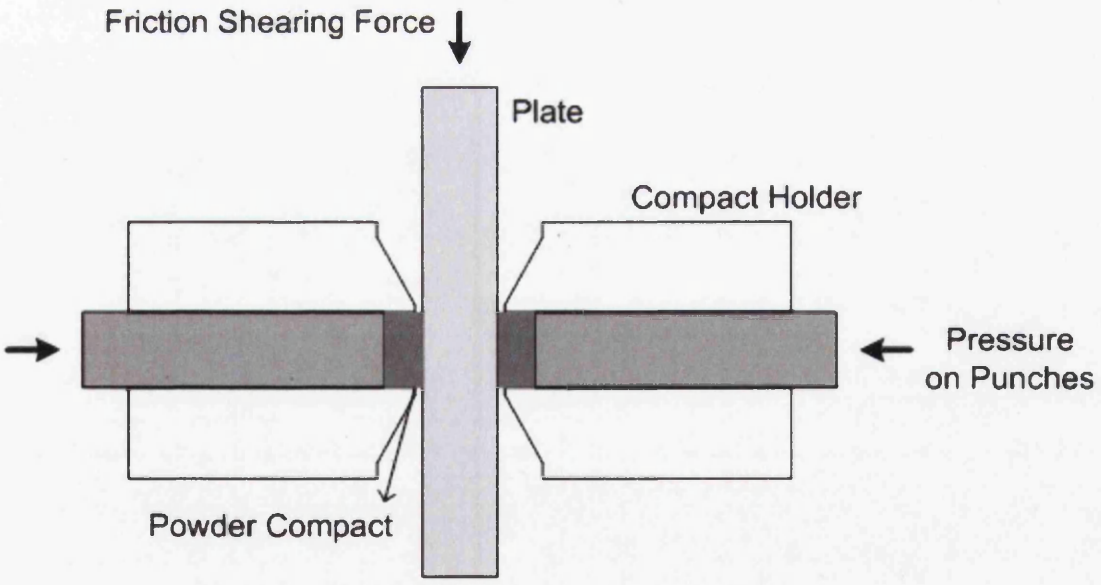

Figure 2. 1 Schematic Diagram of Calliper Shear Apparatus [Strijbos, 1976]

Ceramic powders were chosen for the material and the investigation included consideration of wall surface topology, particle size and hardness of surface and particle. The study showed that particle and surface topology had a significant effect on friction and ratio of particle size to die surface topography was important for softer particles. It was suggested that in order to reduce particle to surface friction, powders must be less hard than the wall and the average particle size must be much larger than the wall roughness. In the cases where the ratio of average particle size to surface roughness was less than or greater than one, the experimental results were found to be discontinuous. An explanation was proposed by describing the different possible mechanisms that could be present, where particles are either locking into grooves or riding over them. It was also suggested that with fine particles, a 'sticking' layer of the powder formed at the wall, which meant that the compact was not directly in contact with the wall but with a thin layer of its own particles. Therefore, it was proposed that die wall roughness and hardness had no influence on the dynamic coefficient of friction.

[Doremus, 2001] reported experiments to investigate friction using a shear plate technique with different process parameters, such as density, normal stress, sliding velocity, temperature and displacement. For the materials, iron powder and a tungsten carbide target surface were chosen. The importance on amplitude of displacement was considered, of which the displacement of the sample was large (around 80mm). The apparatus had maximum sliding velocity of 100 mm/s and was capable of applying a normal stress up to 800MPa. It was found out that normal stress as well as density has a positive influence on the coefficient of friction, whereas sliding velocity, temperature and displacement had only a small effect. For a given normal direction force, the coefficient of friction decreased initially followed by an increase to a constant value. This behaviour was explained as extrusion of lubricants from the compact.

[Cameron, 2002] also reported friction measurement using a shear plate technique. Surface roughness and hardness were explored for iron and alumina

powders, where a number of different target surfaces were used. The experiment involved short sliding distance (5 mm) at low sliding velocity. It was suggested that static and dynamic friction identified were dependent on surface roughness, direction and hardness. In the case of soft surfaces, evidence of particle ploughing was reported and this had a significant effect on the static friction levels. Additionally, friction mechanisms proposed by [Strijbos, 1976] were shown. For the rough surface with the surface finish transverse to the sliding direction, the particles were locked in the grooves then sheared, where for the smoother surface the particles were sliding over it.

As mentioned previously, [PM Modnet, 2002] reported the comparison work between indirect and direct friction measurement method, i.e. friction measurement via instrumented die and shear plate, from different centres. The results from the shear plate test showed closer agreement, in comparison with the instrumented die. For coefficient of friction against normal load, consistent results were reported for the shear plate tests and larger spread between the centres for the instrumented die tests. From both tests, reduction in friction coefficient was observed as the stress level was increased.

[Solimanjad, 2003] introduced a novel friction measurement method to investigate friction behaviour of powder during compaction. The friction was measured between the upper punch and the top of the ring shaped powder compact, which started to rotate with the die at a constant sliding speed once the punch had reached its desired position in the normal direction. Friction mechanisms were explored with consideration of the roughness of the compact surfaces for a range of densities. The relationship between coefficient of friction and density, and surface roughness and coefficient of friction (as a function of normal pressure) were also explored. The friction coefficient decreased in the case of higher densities and normal stress, where it was found out that the friction coefficient is highly dependent on the powder rearrangement at lower densities.

2.3 COMPACTION / FRICTION MODELLING

Over the years, the numerical simulation of material forming processes has been developed to a certain extent and the number of works devoted to it is rising. There are many tools developed for numerical simulation at the present time.

There are two main methods of modelling the powder compaction process as follows:

- Macro-Mechanical Modelling
- Micro-Mechanical Modelling

2.3.1 Macro-Mechanical Modelling

The macro-mechanical model considers powder particles as a continuum and usually adopts the finite element method as the analysis tool. The bulk behaviour of the powder is modelled and such behaviour is captured by a material model embodied into the simulation. Outputs of this model include displacement of powders and tool, stress (force), shape of the compact and density distribution. Accurate input parameters are required such as geometry of tool and powders, material properties, and assigning the kinematics that are to be applied.

This section will review the developments of finite element (FE) modelling work reported in the literature regarding the powder compaction process. The overview of applications using FE modelling will be reviewed, but the details of the numerical aspects of the scheme will not be considered.

[Riedel, 1992] described a feasibility study to model both die pressing and sintering processes using the FE program ADINA. The shape distortions were predicted using the FE method based on an implicit formulation. It was concluded that although the die pressing and sintering processes were modelled, the constitutive models and the numerical algorithms could be improved.

[Haggblad, 1994] performed a numerical simulation of pressing hard metal components. In order to take the non-linearity of the powder into account, explicit integration of the equations of motion for small time steps was used instead of implicit methods. The material model used was based on DiMaggio-Sandler cap model. The study suggested the requirement for the simulation as, a constitutive model, definition of a contact model and requirement of efficient scheme for the solution of the FE model. Although the analytical results were in agreement with measured density distribution, some deviations were found. These were explained by the shortcomings of the material model covering the compaction process from loose powder to the density value of the green part and the use of a Coulomb friction model, where the effects of displacement, relative velocity and the material state of the powder at the contact were excluded.

[Gethin, 1994] reported a FE based approach with a large displacement combined with experimental investigation using iron powder. Material properties from the experiment and geometries of a generic bush part and a rotational flanged component were utilised. Accurate agreement on density fields was reported for both case studies, where for multilevel parts displacement histories was found to have a significant effect on the final part density.

[Redanz, 1998] introduced a FE program for the analysis of porosity and stress distributions in a powder compact. The effects of friction, compaction method and material properties were investigated in this study. For the material model, a combination of Gurson and FKM models, developed by Fleck, Kuhn and

McMeeking, was used to account for low and high porosity respectively. For the friction between the powder and die wall, a Coulomb friction model was used with a constant friction shear stress for unrealistic Coulomb friction at high normal pressures. It was found out that the geometry of the compact, the amount of friction and the pressing method had significant effect on the porosity and strain fields of the compact. For a simple geometry such as a straight cylinder, the porosity was constant throughout if no friction was defined between the powder and die wall. However, non-homogeneous porosity distributions occurred for a more complex geometry. It was also stated that better results were obtained at lower load application. The study showed reasonable results can be achieved for a simple geometry, but further work is necessary for a more complex geometry.

[Wikman, 2000] reported estimation of wall friction coefficient through FE analysis and analytical model (by calculation) for single action cold pressing of a cylinder shaped component. It was stated that the coupling between the material model and the friction model was important. From the results, the behaviour of friction coefficient had a high level at the start of compaction and then reduced gradually. This was explained by the interaction between the deformation of individual particles and the powder mass. It was proposed that at the earlier part of the compaction stage, the contact pressures on each particle in contact and local stress were both high and this resulted in higher die wall friction. The gradual reduction in friction as the compaction proceeds was explained by growing contact area on the individual particles, hardening of the material and movement of lubricants to the die wall.

A benchmark comparison of between FE methods was presented in [PM Modnet, 2002], where simulations of compression stage of the forming process by four separate FE codes are reported. The FE codes were using either Cam-Clay or Drucker-Parger cap model or both. The impact of non-uniform filling density and the effect of fixed and varying die wall friction data were tested. Remeshing to ensure the mesh quality during the simulation was also tested and gave identical

results, which meant it was not required for the kinematic prescription that was used in the simulation. The simulations were found to be consistent in their prediction of density over the compact radius and punch force levels but not in compact height. The consistency in punch force levels led to an agreement within 30 percent of data measured from experimental pressing processes and the overall density was predicted within $0.5gcm^{-3}$ compared to the experimental results.

[Khoei, 2002] introduced an inelastic FE analysis for the powder compaction process by using material properties derived from experimental data. Material parameters such as cohesion, internal friction angle and Young's modulus of powder were established as functions of relative density. A three-dimensional bush component was modelled for the simulation and its powder behaviour during compaction was investigated.

[Sinka, 2003] reported numerical analysis for the die compaction of pharmaceutical powder (microcrystalline cellulose), with significantly lower initial relative density than other powder materials using a Drucker-Prager cap type model. It was concluded that the model could also incorporate low initial density materials subjected to high triaxiality stress conditions. It was suggested that the generalisation of density distribution was not possible because of the variation in contributing factors such as constitutive response, friction, geometry, loading schedule and initial conditions.

[Cante, 2005] proposed a numerical model of the powder transfer stage in the powder compaction process. Very low density powders were taken into account to enable the numerical simulations to deal with compaction processes involving relevant powder transfer stages. It was concluded that although direct measurements of mechanical properties and densification for low density materials were a difficult task, appropriate material characterisation was required for the numerical modelling to produce satisfying results.

[Wu, 2005] investigated the mechanical behaviour of pharmaceutical powder (lactose) by FE analysis using a Drucker-Prager cap model. For the experimental data, an instrumented die was used for uniaxial compaction experiments. Similar to most powder compaction modelling processes, the material characterisation and die wall friction were determined from the experiment and were used as input for FE analysis. It was reported that FE analysis was able to reproduce the dependence of relative density on the compaction pressure of powder beds measured from experiments.

To conclude this section on macro-mechanical modelling, it can be seen that models concerning powder compaction are available to a certain extent. However, modelling multi parts with complex geometries, which will require many different compaction levels are still available for investigation. Additionally, the importance of an accurate input data such as material characterisation was highlighted for all the FE based analyses.

2.3.2 Micro-Mechanical Modelling

In micro-mechanical modelling, powder particles are treated individually and are modelled using discrete simulation techniques. It involves interaction between particles and is designed to handle the contact situation for a large number of irregular particles, where contact definition is not necessary. It admits the microstructure of engineering materials is discontinuous.

Initial models considered the particle to be rigid and only the interactions between particles were modelled. This was represented by rigid particles connected by spring and dashpot seen in Figure 2.2.

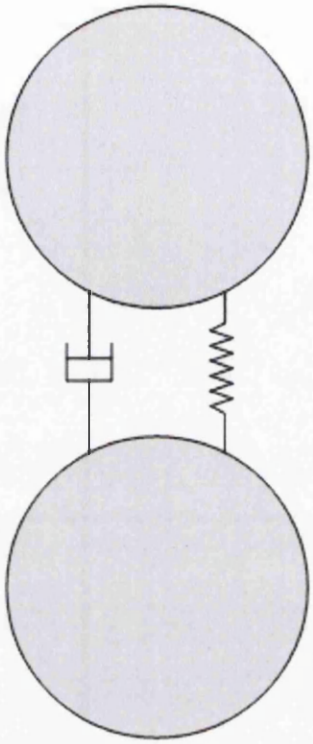

Figure 2. 2 Schematic Diagram of a Discrete Element Model of Two Rigid Particles

[Cundall and Strack, 1979] proposed a method based on the use of an explicit numerical scheme in which the interaction of the particles is monitored contact by contact and the motion of the particles modelled particle by particle. It was stated that the deformations of the individual particles are negligible compared to the deformation of overall particle assembly, which was due to movements of rigid particles. An alternative modelling method was proposed because of the difficulty in determining constitutive material relationships for continuum models. Although later work proved the deformations of individual particles is not negligible, this study introduced a new approach to modelling.

Later work included analysis of particle deformation while normal and tangential springs and dashpots are used at each contact to represent compliance and energy absorption to account for kinematic behaviour [Fleck, 1992]. This study developed a macroscopic yield surface for a random aggregate of perfectly

plastic spherical metal particles. The configuration of this model was treated as isotropic and homogeneous for particle properties and this was used to define the constitutive relationship for a macro-mechanical model. This simplified the issue of micro-mechanical modelling of the whole compaction process with a large number of particles, which is computationally expensive.

[Ransing, 2000] presented modelling of powder compaction process in both finite and discrete element method. The micro-mechanical modelling shown in this study was not assuming the particles to be rigid as it did for the earlier models, but the deformations of particles was also taken into account. The model was two-dimensional with the system representing an assembly of rods. The results of simulation were compared with the compression of a ductile porous material as defined by a Gurson model and agreement was shown. It was highlighted that due to computational demand, modelling the compression of a large assembly was not practical at that time.

[Gethin, 2003] reported a similar discrete deformable element modelling work but for simulation of the compaction involving mixture of ductile and brittle powders to explore its suitability and establish the yield characteristics. The compaction of brittle particles displayed fragmentation, which were closely similar to failures observed in experiments of compression. In the case of mixed particles of ductile and brittle systems, it was reported that ductile particles extruded to surround the brittle particles, which prevented the brittle failure mechanism.

[Skrinjar, 2004] developed a numerical model based on a discrete element method for analysing compaction process of spherical powders. Up to 10000 particles were simulated with perfect plastic material behaviour. The study showed the discrete element method combined with explicit time stepping was effective and accurate for analysing the compaction process. For an isostatic powder compaction process with the same material properties for all particles, the effect of

size variation only had an impact when the number of small particles in the powder was high.

Although some studies reported simulations involving large number of particles [Skrinjar, 2004] [Procopio, 2005], it is still computationally very demanding. Therefore, micro-mechanical models are generally used for localised behaviour of compaction process at present.

In contrast to the hypothetical continuum model, the mathematical formulation of discontinuous problems involves the interaction law between particles and balance principles. The discrete element method (DEM) is one of the most advanced and the most often used approximate numerical method to solve these problems.

In order to account for deformation, fracture and merging of the particles, Combined Finite-Discrete Element Method was introduced. In the Combined Finite-Discrete Element Method, individual particles are represented by individual discrete elements, which allow interaction between particles without the need to define a contact law. Contact laws, such as Hertz contact, cohesion, adhesion and friction can be represented by the use of spring and dashpot type laws. Additionally, each discrete element is divided into finite elements (each discrete element has its own finite element mesh). Investigation of these factors can be performed by using tools and techniques of the finite element method together with the discrete element method to capture gross displacement of the particle.

2.4 MICRO SCALE FRICTION MEASUREMENT USING AFM

Atomic force microscopy (AFM) is a powerful and versatile tool for investigating surfaces and surface material development including local mechanical properties, friction and adhesion at the particle scale. AFM can function as an imaging device as well as a force sensor in both normal and lateral directions. This section will focus on the application of AFM in terms of friction measurement, also known as lateral force microscopy (LFM) or friction force microscopy (FFM).

Finite element simulation is useful in the calibration of the stiffness of the cantilever and is critical for a better understanding of the probe response. Response calibration involves cantilever stiffness calibration as well as detector calibration. Although procedures for normal force calibration are becoming more established, further exploration and verification is required [Clifford, 2005]. For lateral force calibration, further difficulties are encountered with no acknowledged method of calibration to obtain a quantitative measure of friction.

[Liu, 1994] performed LFM experiment with a simple rectangular cantilever and established a calibration using simple beam bending theory. For normal force, a correlation between the bending of the cantilever and the signal of the detector was established. It is also reported that for lateral force calibration, the bending of the cantilever was minimal compared to its twist and thus it was neglected.

[Neumeister, 1994] considered calibration of stiffness for a V-shaped cantilever using mathematical modelling. Equations were derived to represent stiffness and they were compared with a FE analysis resulting in good agreement.

[Noy, 1995] reported experimental results regarding CFM (chemical force microscopy), AFM with modification of coating on the probe tip. The calibration of the lateral stiffness was approximated by an equation expressed in terms of normal stiffness.

[Ogletree, 1996] introduced another method of lateral stiffness calibration. It involved measuring the response of lateral force experimentally on well-defined slopes. Lateral signals for back and forth scans were made for these slopes. The importance of the experimental calibration required for each cantilever was highlighted. The factors were identified to be cantilever properties, tip variation, and alignment of the deflection sensor.

The issue of cantilever properties identified above was reinforced by [Khan, 2004], where Young's modulus of cantilever material (silicon nitride) was investigated further. It was reported that the value found (280-290 GPa) was significantly higher than previously reported (146 GPa).

Apart from the calibration issue, the main factors for friction measurement using AFM were identified from experimental findings.

[Aime, 1995] reported an experiment with a tip scanning a curved surface and derived a general expression for contact mode in AFM. It was stated that the effect of adhesion and the magnitude of friction coefficient could be explored by observing the shift of the maximum height as a function of the direction of the scan and the change of the object shape.

[Gibson, 1997] identified the main parameters of a LFM system and discussed methods of determining them. The parameters were tip shape, detector

sensitivity, normal and lateral spring constants, effective normal and lateral forces and influence of topography.

[Bhushan, 1998] reported experiments to explore the friction and wear mechanism by using a colloid probe instead of a sharp tip at the end of the V-shaped cantilever. For the colloid probe, different values of tip radius were used to investigate the effect on friction, which were $0.05\mu m$, $3.8\mu m$ and $14.5\mu m$ for Si_3N_4 and SiO_2. The coefficient of friction was found to increase with the tip radius and was negligible up to a certain load, where it increased rapidly above this load.

The study of AFM involving colloid probe scanning over four different surface finishes of stainless steel (304) was proposed in [Bowen et al, 2001]. Colloid particle adhesion was measured and it was shown that for the plate used for equipment manufacture, adhesion was less at rougher surfaces, whereas for plates having an aesthetic finish, adhesion was very comparable even though the surface roughness varied.

[Meine, 2002] investigated the correlation between surface roughness and friction for a colloid probe model. A change of friction was observed when the probe was scanning over a step type surface and depending on the direction of travel, the friction increased or decreased. Change in deformed sample volume was proposed for the cause of change in friction.

Numerical modelling of AFM is a relatively novel area of research, especially in three-dimensional geometry.

[Song, 2006] designed a three-dimensional beam cantilever model with pyramid shaped tip for the FE simulations of different modes that exist in AFM, i.e.

tapping mode, torsional resonance mode, and lateral excitation mode. The issues of bending and twisting of the cantilever in the lateral direction was discussed and stated that lateral bending can only be neglected only if the lateral interaction is relatively small compared to the lateral stiffness (bending) of the cantilever. Additionally, it was reported that tip properties strongly affects amplitude and phase of the cantilever responses. Tip properties include its geometry, material, and adhesive for the case of a colloid probe model.

2.5 CLOSURE

From the key process parameters of powder compaction, friction was found to have a significant impact on compact quality consistently. Although the area concerning the effect of friction in powder compaction is well documented, further understanding of friction mechanisms could be explored regarding effects of surfaces and loading conditions. For this purpose, experimental work using an extended sliding plate apparatus for low loads on different surfaces will be shown in Chapter 3.

The friction measurement method at the micro scale was reviewed in connection with the AFM. Although some works have been reported on calibration of the cantilever, no constitutive method was developed at present, especially for calibration of the lateral stiffness. Additionally, it was shown that the area of numerical modelling for AFM indicates that a great amount of research needs to be done. These issues will be explored by designing a numerical model and this is addressed in Chapter 4.

The review of modelling showed that some works have been reported in micro-mechanical modelling of powder compaction process for the investigation of

friction. However, limited work has been reported on a more detailed exploration with investigating the effects of various issues identified from experimental work. This will be attempted in Chapter 5 and 6 through various micro-mechanical models exploring compaction and shear stages respectively.

3

MACRO SCALE FRICTION MEASUREMENT METHOD

3.1 INTRODUCTION

Previous studies show that there are two main methods of measuring friction in powder compaction at the macro scale. The first is an indirect friction measurement, which involves a compaction process. The second is a direct friction measurement, where a target surface is run under the powder compact.

Indirect friction measurement involves the use of instrumented die apparatus [Gethin, 1994]. In this experiment, axial stresses at the top and bottom faces of the compact are measured together with radial stress variation over its height. The relationship between shear and radial stress at the die surface are analysed and the coefficient of friction derived. Disadvantages of the instrumented die method include determination of radial stress variation and it is relatively inflexible to allow exploration of process variables. The advantage is that it approximates the actual compaction process closely.

In the direct friction measurement approach the experiment utilises a sliding plate [Doremus and Pavier, 1998]. The normal force can be set and the shear force required to slide a target surface against the compact measured. The friction coefficient is deduced from the ratio between these two forces. Another direct friction measurement methods include pin on disc method [Fuentes, 2003], and equipment based on a calliper design [Strijbos, 1976]. However, for investigating low compaction forces (i.e. low density compacts), both of these methods are not suitable since the compact needs to be self-supporting. Therefore, heat treatment of compact is usually involved. The pin on disc machine is associated principally with wear studies. For powder compaction, again the samples need to be self supporting, it differs from other methods since there is no restriction on sliding distance.

The sliding plate equipment described in [Cameron, 2002] uses a short sliding distances and moves at low speeds. The ratio between sliding distance and punch diameter was 0.25 (5mm/20mm). It is possible that other frictional response will be exhibited when sliding occurs over a longer distance. An equipment that

incorporates this capability is described in [Doremus, 2001]. The ratio from this experiment was 5 (80mm/16mm). Data presented by the authors show valuable information including the behaviour of friction coefficient with the extrusion of lubricant and further understanding of static and dynamic friction. The experiments were conducted for both ductile (Iron) and agglomerated powders (Ceramic, Tungsten) at high contact stresses. The current project is concerned with other powder types and is also concerned with lower contact pressures.

To investigate the behaviour of friction coefficient for low normal direction loads over long sliding distances, an extended sliding plate apparatus was designed and utilised in this project with the ratio between sliding distance and die diameter of 3.3 (50mm/15mm).

In this chapter, work using the extended sliding plate apparatus for measuring friction between powders and target surfaces will be presented.

3.2 EXPERIMENT

As mentioned previously, the sliding plate method is preferred in this experiment because:

- it allows variation of die material parameters or surface modification
- it allows measurements on low density compacts

3.2.1 Sliding Plate Technique

The sliding plate that was used previously in experimentation is described in [Cameron, 2002]. It consists of two main parts. The top part comprises a fixed "bridge" that provides guidance for the punch and a bottom block that supports the target surface. Needle roller bearings are fitted beneath the bottom block to support

it and to reduce friction to a negligible level (friction coefficient about 0.002). The bottom block is driven by a servo mechanical system, which pushes the bottom block horizontally. The target surface is set to be 50 mm in diameter. A load cell is placed between the bottom block and lateral drive, which means the bottom block and the load cell, are both pushed horizontally by the drive system.

In operation, powder is loaded inside the die and the punch compresses this up to a specified normal force, which is maintained. Then the target surface is pushed laterally under the compact and the friction force recorded via the load cell.

In this experiment, there were limitations in load level of normal force, sliding distance and sliding speed (i.e load level of 100kN, displacement of 8mm, and speed of around 0.07mm/s). Surface roughness (Ra) of 0.02, 0.1, 0.5 and 1.0 μm were also explored.

3.2.2 Extended Sliding Plate

The extended sliding plate was designed to observe friction with variation of parameters that includes load, speed, sliding distance, and surface finish. The new equipment design is shown in Figure 3.1.

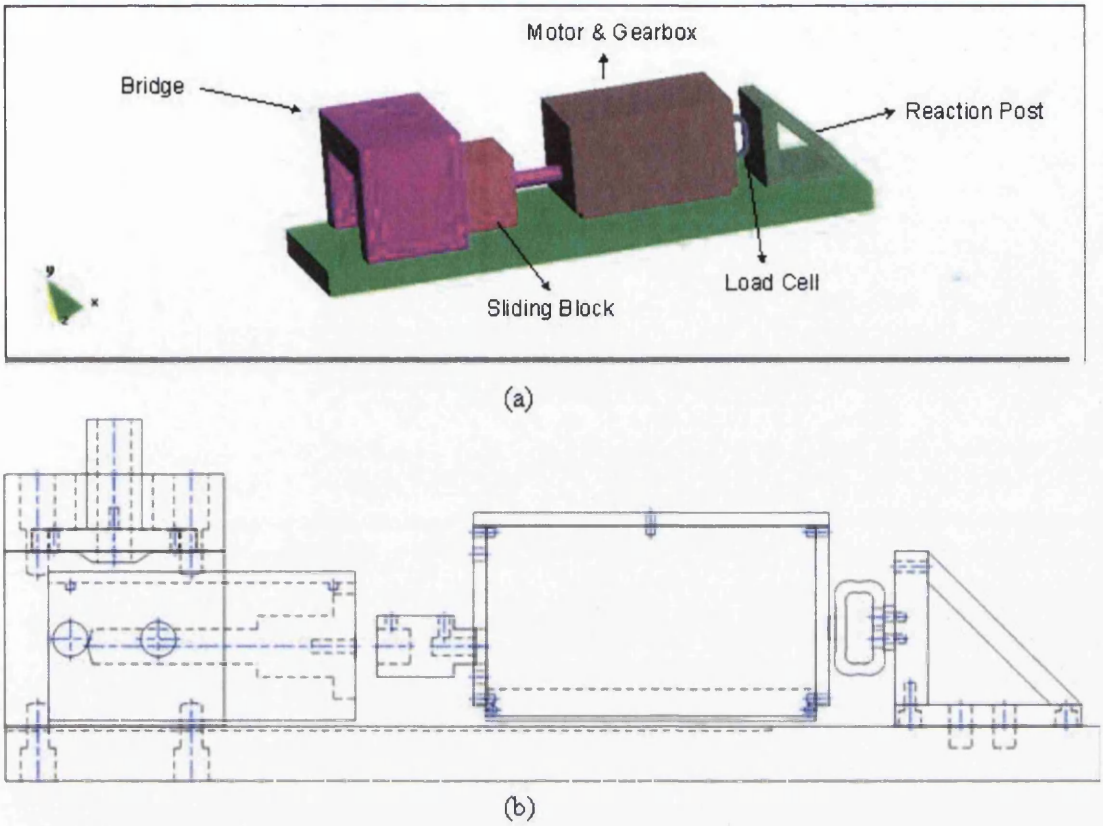

Figure 3. 1 (a) Schematic of the Extended Sliding Plate Apparatus
(b) Design of the Extended Sliding Plate

Similar to the original sliding plate apparatus, it includes the bridge block to hold the punch and the moving block with the target surface installed. In this design, only the bridge block and the triangular block at the end were fixed to the base block. Instead of using a hydraulic motor, an electric motor fixed to a screw was introduced since only low normal force will be explored in this experiment. The moving block was supported by rollers. This design was also applied to the motor block. The reaction force was measured by the load cell fixed to the base. Miniature guides were also installed on both sides of the bridge to secure the linear movement of the block. The guides used a simple ball bearing design and were very lightly loaded to virtually eliminate any friction effects.

The motor and gearbox has two gear stages with rated torque of 800 mNm at 240 rpm. By driving through a ball leadscrew of 4mm pitch, this enables the variation of the linear speed up to 2.2mm/s.

The moving block is 140 mm long and carries the target surface block of 100 mm. This was designed to observe friction over an extended sliding distance.

The target surface blocks were rectangular shape. They were hardened to 60HRC and machined to give surface finishes (Ra) of 0.1-1.0 μm aligned and transverse to the sliding direction.

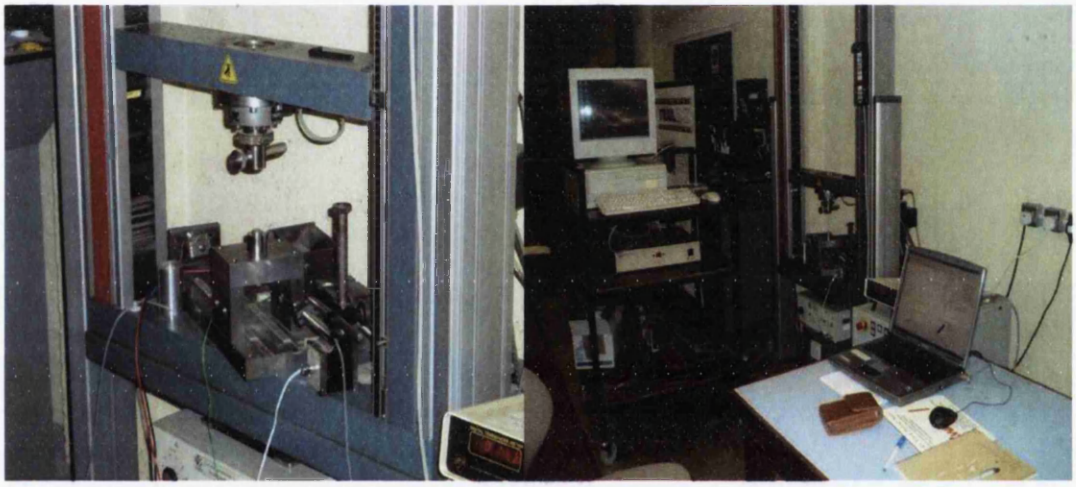

Figure 3.2 Actual Apparatus of Extended Sliding Plate

The overall system is shown in Figure 3.2. The press and the extended sliding plate are shown on the left and the whole apparatus shown on the right. In this case, the press is a static mechanical tester, driven by motorised screws and controlled through PC based software that facilitates programming of different schedules.

3.2.3 Press

A Zwick Z020 materials testing machine was used in this experiment. It has a capacity up to 20 kN. Low loads were used in this experiment ranging from 250N to 1kN, corresponding to pressures from 1.4MPa to 5.7MPa.

The control software used was testXpert 8.1 [Zwick Website, 2006]. As well as closing the control loop, this provides the opportunity to apply a range of loading cycles. The software also includes stiffness and damping control parameters that need to be set to enable smooth operation of the machine and this is influenced by the operation mode (load or displacement control) and the mechanical properties of the test sample (powder compact). Therefore, they were tuned for each sample material. In these tests, the machine was set to compress with a speed in the range 250 to 750 N/s until it reached the desired value of force and this was then held for one minute. The sliding stage of the test was completed during this minute interval.

3.2.4 Load Cell

The load cell for measuring sliding force was calibrated before any experiments took place. Figure 3.3 shows the calibration characteristics for which, the equation is:

$$Shear\ Force = 0.7257 \times Strain + 1.3795$$

The characteristic was found to be repeatable and stable. The sensitivity was established as 1.27mV per Newton.

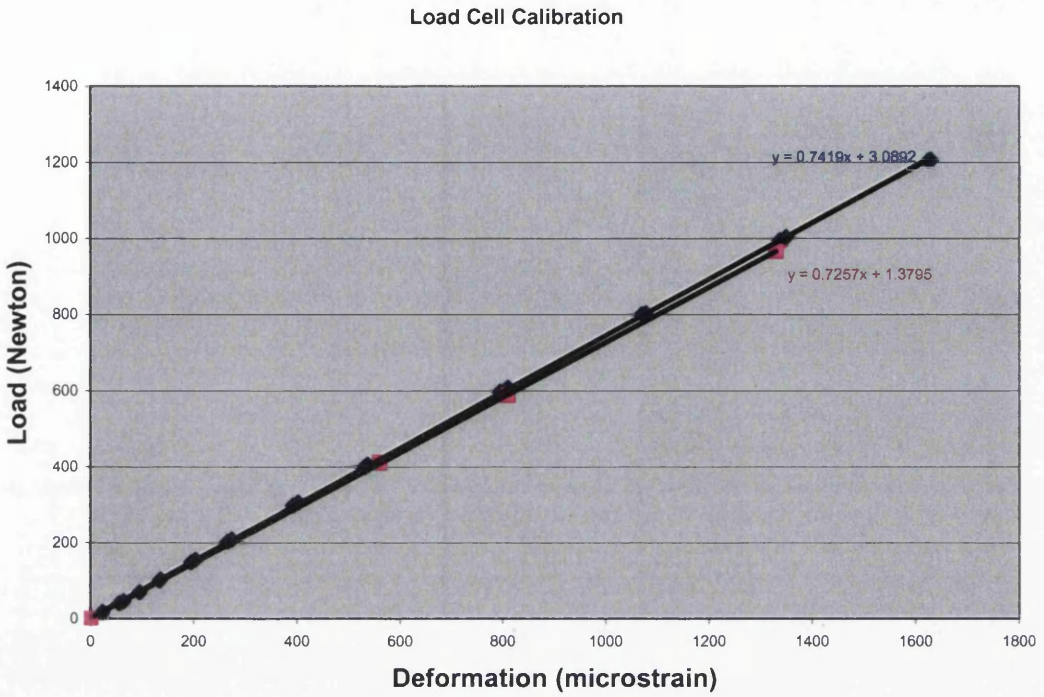

Figure 3. 3 Load Cell Calibration

3.2.5 Displacement Transducers

A linear variable differential transformer (LVDT) was installed to measure the distance the moving block travelled. This was also calibrated prior to the experiment. It was found to be linear, having a sensitivity of 3.58mV/mm.

3.2.6 Data Acquisition

The compression load and displacement was recorded directly from the Zwick control software. For the shear data, acquisition was achieved using a Vishay System 5000 [Vishay Website, 2006] to record both LVDT and the load cell data. The system was set to record at 10Hz. This was set in order to match maximum distance of 50 mm and maximum data of 1000 points per experiment.

The software for the data acquisition was StrainSmart also from Vishay [Vishay Website, 2006]. Synchronisation of data from both sources was carried out during the data reduction stage of the experiment.

3.2.7 Target Surfaces

Eight target surfaces were made with hardened D2 steel (hardened to 60 HRC). Each block was 100 x 35 x 9 mm in dimension. The blocks had different surface roughness and different surface finish directions. Surfaces with roughness (Ra) 0.1, 0.25, 0.5, 1.0 μm in two directions (aligned and transverse to the direction of the shear) were prepared.

3.2.8 Powders

In this experiment, four powders were investigated. They consist of two metal powders (stainless steel and copper), salt and sugar. The characteristics of the powders are itemised in Table 3.1.

Powder	Type	Supplier	Powder Analysis	Particle Size
OFHC Cu	Alloy	Sandvik Osprey Ltd.	Cu balance O 0.062	20~30μm
316L	Alloy	Sandvik Osprey Ltd.	Cr 16.5 Ni 12.0 Mo 2.3 Mn 1.2 Si 0.34 P 0.027 C 0.019 S 0.009 Fe Balance	45~70μm
Salt	Table salt		Crystalline	200~300μm
Sugar	Granulated sugar		Crystalline	100~200μm

Table 3. 1 Characteristics of the Powders

Powders for the experiments were chosen because of their different characteristics. Principally this includes mechanical properties, such as Young's modulus and yield stress.

Typical mechanical properties of the powders were derived from [ASM Metals Handbook, 1986], [Nickel Institute Website, 2006], [Rowe, 1995], [Baer, 2002] and are itemised in Table 3.2.

Powder	**Young's Modulus (GPa)**	**Yield Strength (MPa)**	**Hardness**	**Poisson's Ratio, ν**
OFHC Cu	115	69	40HRF	0.35
316L	200	170 (Minimum)	96HRB (Maximum)	0.3
Salt (Sodium chloride)	1.9	170		0.252
Sugar (Sucrose)	2.2	89		0.25

Table 3. 2 Typical Mechanical Properties of Powders

The differences in modulus and yield levels for the powders are significant. Granulated sugar and table salt were chosen because of their crystalline particle structures. The powders were different in size and shape as observed in Figure 3.4 and 3.5. The effects of differences in the physical and mechanical properties of powders will be investigated later in this chapter.

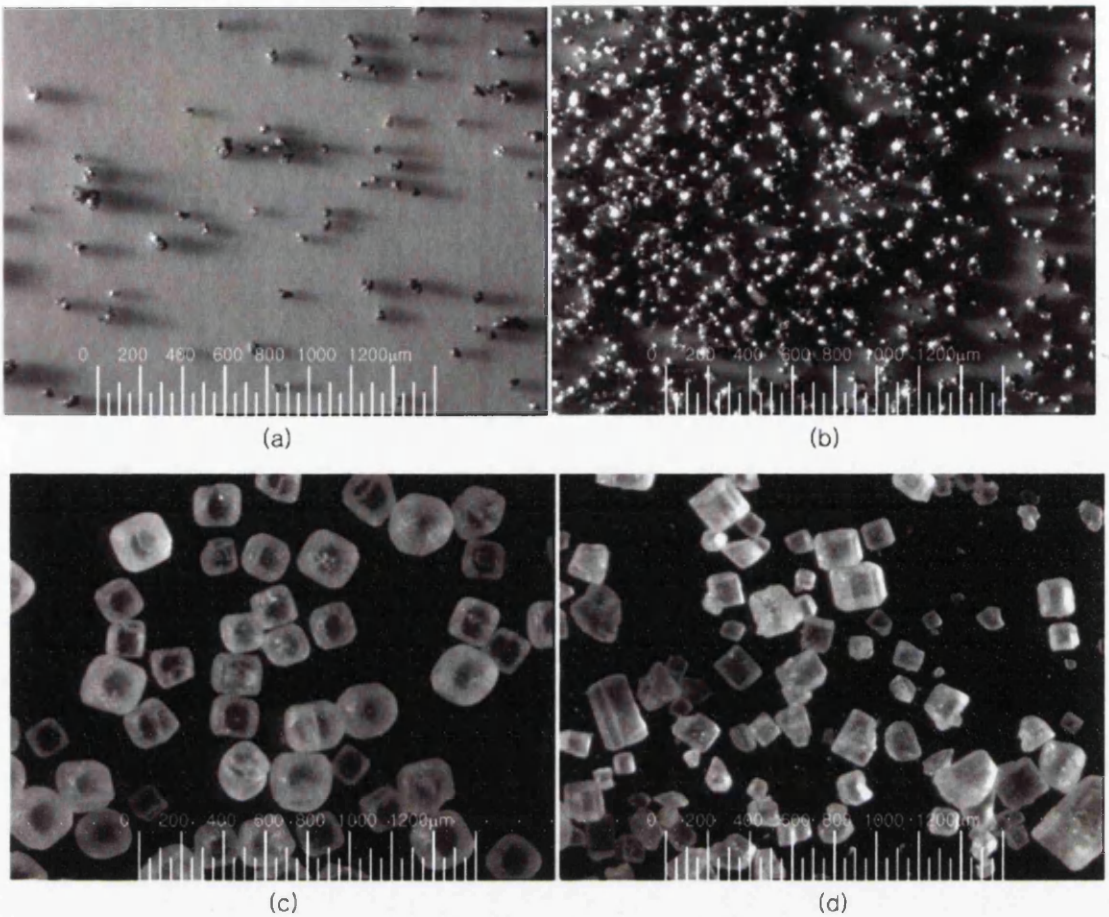

Figure 3. 4 General Microscopic Images of the Powders

(a) OFHC Cu (b) 316L (c) Salt (d) Sugar

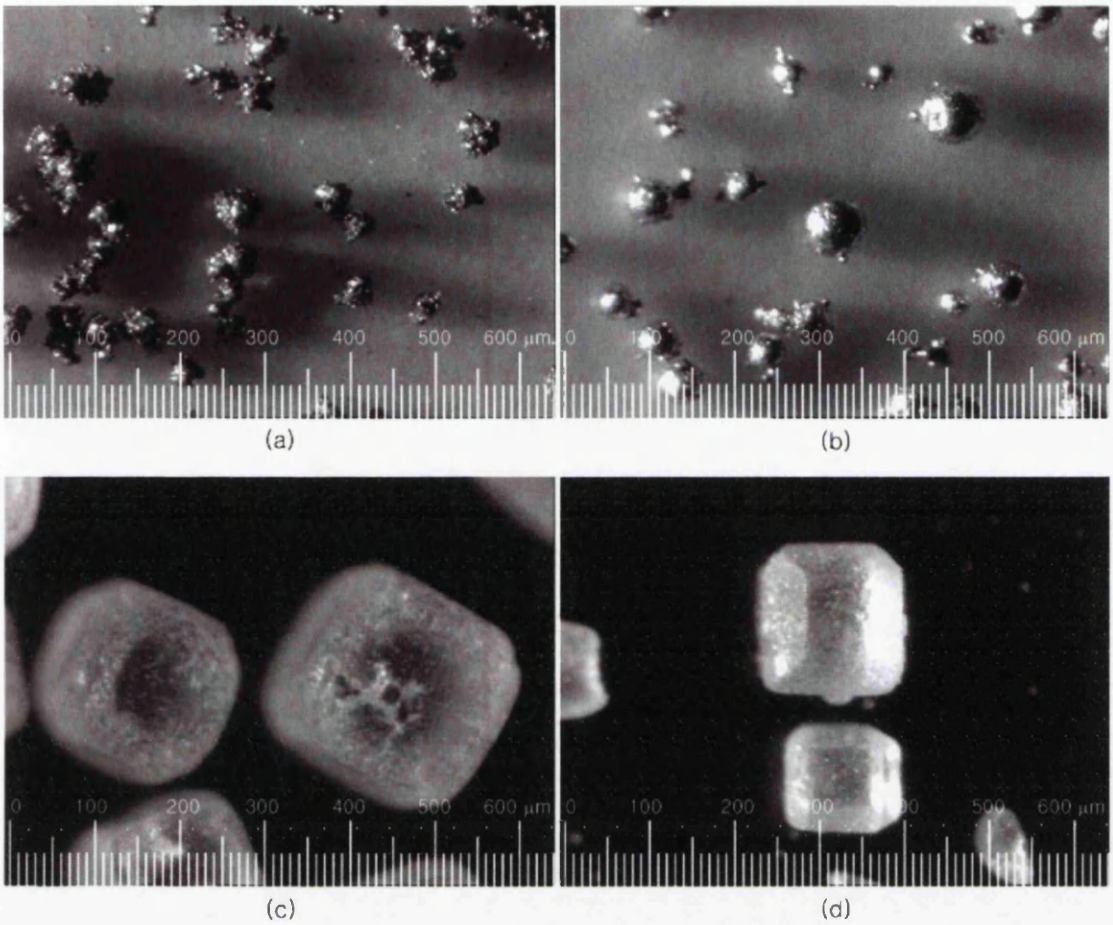

Figure 3. 5 Detailed Microscopic Images of the Powders

(a) OFHC Cu (b)316L (c) Salt (d) Sugar

The images were taken from LEICA MZ 12.5 stereomicroscope with the software EasyGrab [Noldus Website, 2006].

3.3 RESULTS

The results from the powders will be presented in this section. The presentation will be mainly divided into three sections, which are as follows:

- Control Stabilisation Experiments
- Consistency Experiments
- Data Reduction Issues (compression and shear curves)

Before exploring the results, the experimental procedure will be discussed.

3.3.1 Experimental Procedure

1. The target surface block was cleaned before every experiment with isopropyl alcohol solvent then put in the moving block, in order to make sure there were no embedded powders on the target surface.
2. 10g (5g for granulated sugar) of powder was measured and loaded into the die.
3. The press programme was started, compacting the powder that was then sustained until it reached the target load.
4. The positions of displacement transducers were checked and the data acquisition process was started (recording data from LVDT and load cell).
5. The motor to drive the target surface in the lateral direction was turned on with a set speed giving the shear force.
6. The procedures above were repeated at least three times per experiment with the variations of powders, surface finishes, directions, and speed as summarised in Table 3.3.

Powders	**Surfaces Tested (Material / Surface Finish(Ra))**	**Normal Forces (N)**	**Speed of Sliding Plate (mm/s)**
OFHC Cu	Hardened D2 steel /0.1, 0.25, 0.5, 1.0 parallel and perpendicular	250, 500, 750, 1000	0.7 1.3 2.2
316L	Hardened D2 steel /0.1, 0.25, 0.5, 1.0 parallel and perpendicular	250, 500, 750, 1000	0.7 1.3 2.2
Salt	Hardened D2 steel /0.1, 0.25, 0.5, 1.0 parallel and perpendicular	250, 500, 750, 1000	0.7 1.3 2.2
Sugar	Hardened D2 steel /0.1, 0.25, 0.5, 1.0 parallel and perpendicular	250, 500, 750, 1000	0.7 1.3 2.2

Table 3. 3 Summary of Experiments Completed

The target block of surface finish (Ra) 1.0 μm parallel with speed setting of 1.3 mm/s was assigned as the reference. This was chosen because surface finish (Ra) of 1.0 μm is likely to lead to a significant friction coefficient and the speed of 1.3 mm/s was selected because it represents an average value. For different surface finishes, directions, and speeds, the normal load of 1kN was set to be the reference.

Then for each powder, a load range from 250 to 1kN was applied at the punch. For each powder, surface finish (Ra) from 0.1 to 1.0 μm (both aligned and transverse to the direction of movement) was explored. In addition, experiments with speed from 0.7 to 2.2 mm/s were carried out.

For all powders, every experiment was repeated at least three times for consistency evaluation and to assure statistical confidence.

Although this may not reflect industrial practice, cleaning between tests ensures a consistent surface since any debris or contamination from a previous test that will affect the sliding force levels was removed.

3.3.2 Control Stabilisation Experiments

In setting up the press and running the software TestXpert 8.1, there is a need to stabilise press control. This assures the smooth compression at the set loading rate. The stiffness and damping parameter choice depends on the mechanical properties of the powder compact and this is dependant on the powder being tested. The control parameters are itemised in Appendix A.1.

The press was held for 60 seconds once it has reached the target normal force for all powders.

The process was loading rate controlled and in range of 250 to 750 N/s. Effects of different loading rates were explored and found out that the higher it is the sharper the load increase until it reaches the target load. In consideration of the time taken to reach its target value, faster speed was set for higher loads.

3.3.3 Consistency Experiments

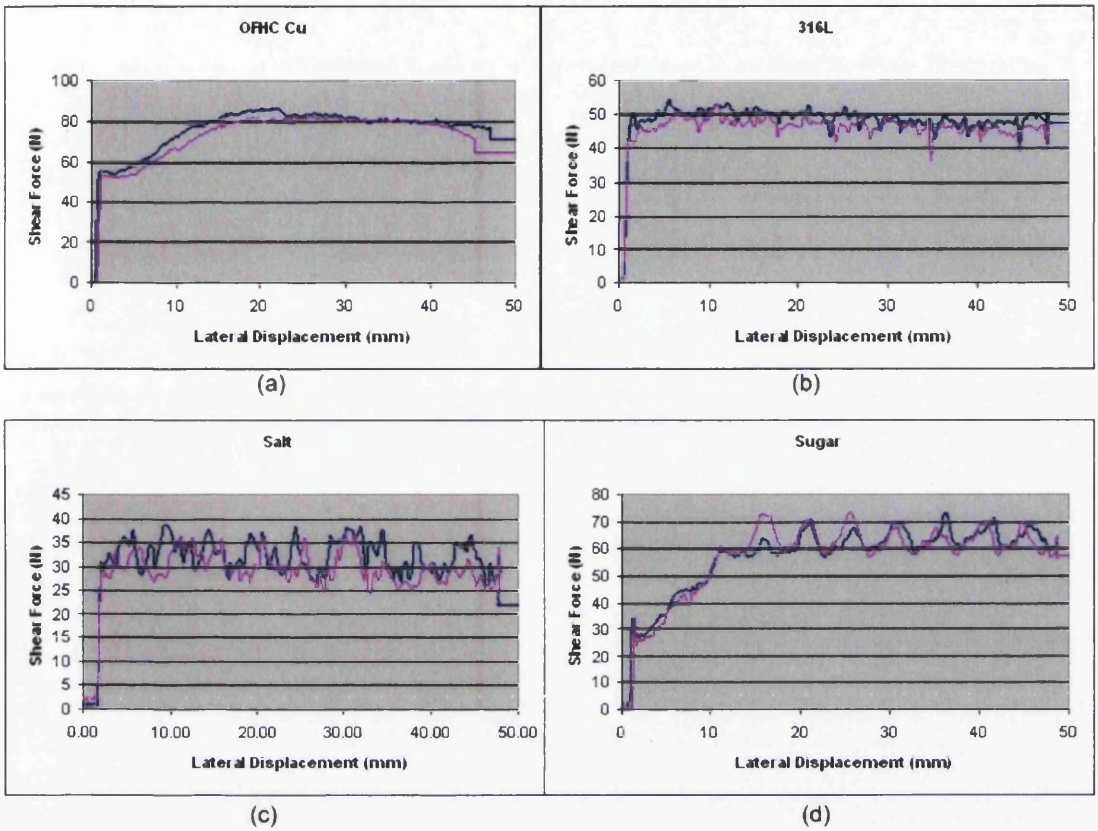

Figure 3. 6 Shear Force against Horizontal Displacement for Validation of Consistency (a) OFHC Cu (b) 316L (c) Salt (d) Sugar

For each powder, the same experiments were carried out numerous times to see if the results were consistent. As shown in Figure 3.6, for all powders, the results were consistent in both form and level throughout the processes. Some curves display a small and random fluctuation. This may be a reflection of a slip-stick response or a consequence of fluctuation in applied load as a consequence of limitations in the closed loop control. Salt and Sugar display a more regular fluctuation and this can be assigned directly to a slip-stick response in sliding.

Behaviour of Coefficient of Friction

Before exploring the behaviour of the friction coefficient, the issue of force transmission losses in the die was considered. An equation used for calculating the coefficient of friction indirectly from a long cylinder compaction experiment with the assumption of an elastic behaviour of the compact is used to handle the force transmission losses simply. The relevant equation was derived and shown to be reasonable from [Cameron, 2000].

$$F_b = F_t e^{\frac{-4\mu\nu L}{D(1-\nu)}} \tag{3.1}$$

where F_b is the axial force on the bottom of the compact

F_t is the axial force on the top

D is the diameter of the powder compact

L is length of the compact

ν is the Poisson's ratio

And the coefficient of friction is defined by the following ratio.

$$\mu = \frac{F_l}{F_n} \tag{3.2}$$

where F_l is the force in lateral direction

F_n is the force in normal direction ($=F_b$)

Taking the equation into account, the coefficient of friction for both ductile and brittle materials with axial force on the top of the compact are acquired from the shear and compression curve data from the data reduction section (3.3.4). By using the equation (3.1), with the appropriate material properties for each powder enables an estimate of force levels at the bottom of the compact. However, the equation required specification of a friction coefficient (μ). This was derived from force data in compression curves (Figure 3.8) and shear curves (Figure 3.11) as shown in equation (3.2). The transmission coefficients ($e^{\frac{-4\mu\nu L}{D(1-\nu)}}$) were determined as in range of 0.61~0.99, 0.71~0.99, 0.83~0.99 and 0.79~0.99 for Cu, 316L, Salt and Sugar respectively.

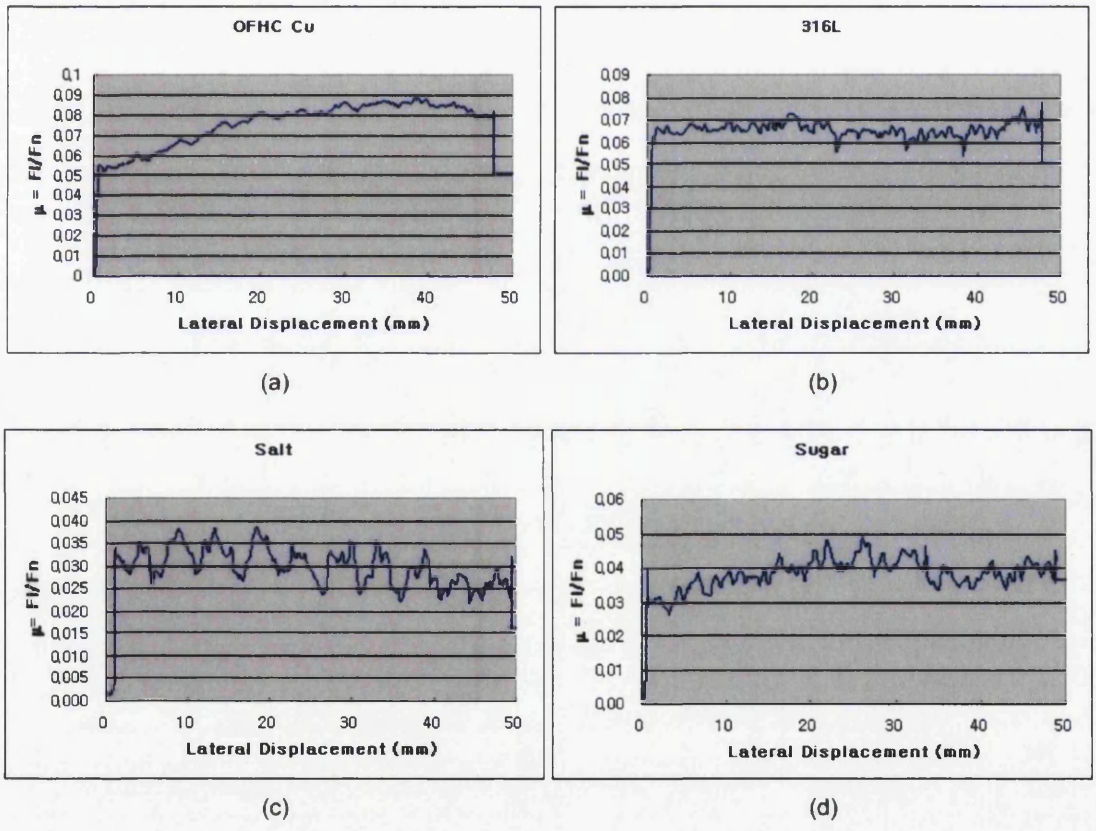

Figure 3. 7 The Behaviour of Coefficient of Friction for Powders with 1kN Normal Load and Ra of 0.25 μm

(a) OFHC Cu (b) 316L (c) Salt (d) Sugar

By looking at the coefficient of friction graphs, it can be observed that the coefficient of friction reaches a maximum value quite rapidly corresponding to the static value. Under dynamic (sliding) conditions, it then reduces gradually, especially in the cases of 316L and Salt. For OFHC Cu and Sugar the coefficient of friction tend to increase achieving a stable value towards the end of the stroke.

The values of coefficient of friction in Figure 3.6 seem much lower than the results that were reported in [Doremus, 2001], but the results were under a very low normal force of 1kN whereas the previous work was up to 800MPa with 16mm diameter die which comes to around 161 kN. Additionally, the result from this work will be high at low density, because of equipment resolution. Recent evidence shows that friction is also low at low pressure, provided that instant sensitivity is achieved. However, the general shape of the friction coefficient graph seems similar. The decrease of friction coefficient after the initial rise was also seen here, especially in cases of OFHC Cu and sugar.

Further investigation will be performed in terms of shear force in the next section.

3.3.4 Compression Curves

It is also appropriate to consider the compression characteristics of the different powders as a means of contrasting their behaviour. Figure 3.8 and 3.9 shows their compression behaviour.

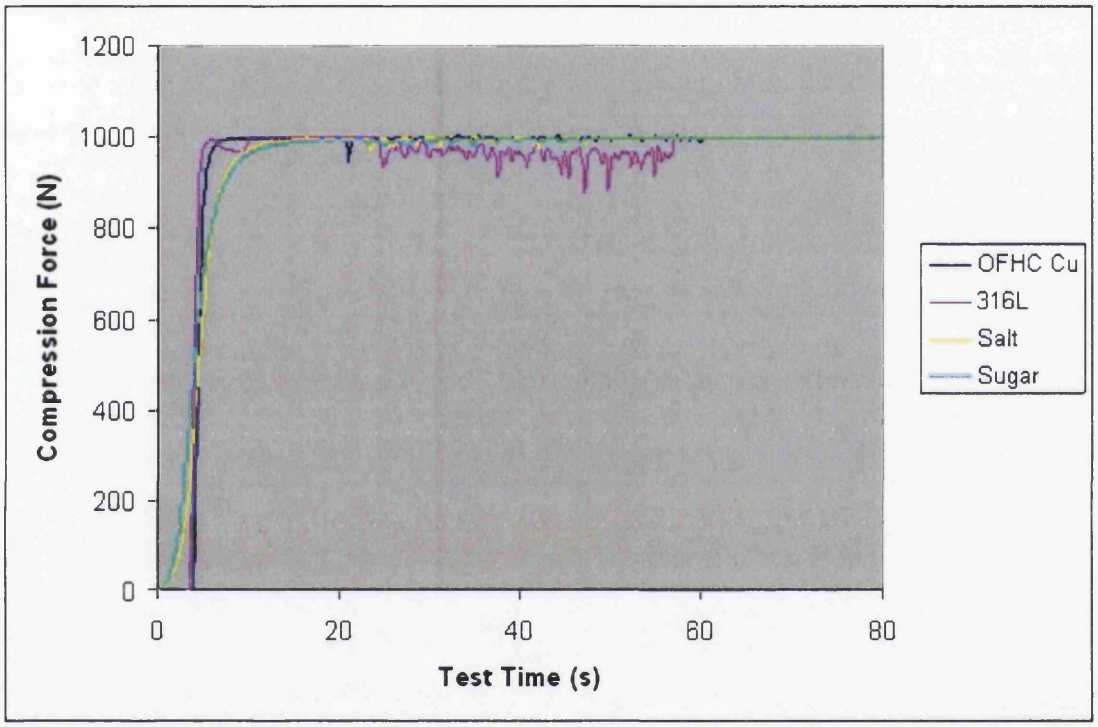

Figure 3. 8 Compression Curves of Normal Force against Test Time

Figure 3.8 illustrates the force build up and confirms it achieves a stable level of 1kN for the duration of the shear stage of the experiment. However, the different powders exhibit different force evolution patterns. The ductile powders exhibit a very sharp build up whereas the salt and sugar exhibit a more progressive action. This is most likely to be attributable to particle shape (Figure 3.5). The OFHC Cu and 316L are spherical, and hence close packed whereas the salt and sugar are

cubic and therefore exhibit a rearrangement phase during which the force build up is more gradual.

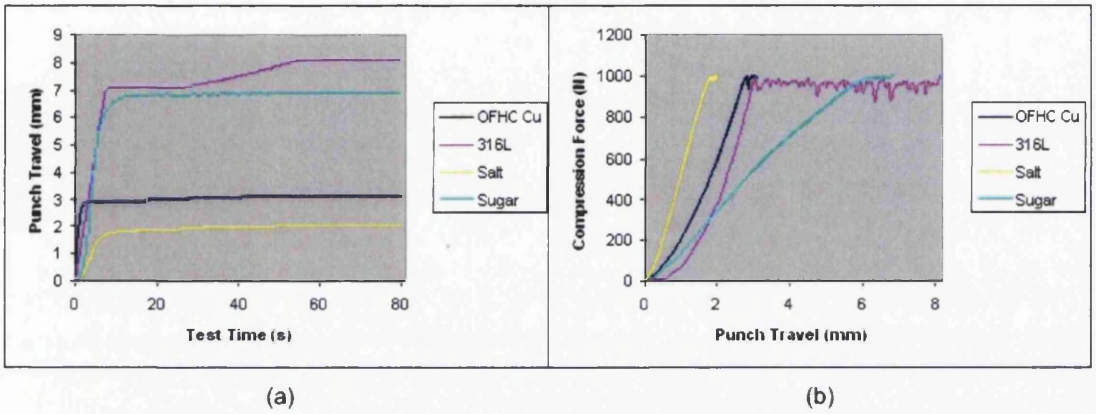

(a) (b)

Figure 3. 9 Compression Curves of (a) Punch Displacement against Time (b) Compression Force against Punch Displacement

Figure 3.9(a) depicts the punch displacement curves that achieve typically a 1kN/s loading rate. Sugar and 316L share a similar punch velocity whereas copper compacts very quickly due to its low modulus and salt exhibits a low compaction speed with only little displacement. All powders exhibit some further punch displacement particularly for the 316L powder. The Figure 3.9(b) shows the characteristic force against displacement data. This confirms the response similarity for the metal powders, the stiff response of salt, and the more linear elastic behaviour of sugar.

3.3.5 Shear Curves

Shear curves allow a direct comparison of process effects without the need for data reduction, provided that compacts are identical in size between tests, which is implied by a consistent test powder load. Therefore, this section will focus on comparative type studies.

3.3.5.1 Different Loads

For every powder, with same surface finish target blocks, four different normal loads were applied (250N, 500N, 750N, 1kN). The target surface of 1.0 Ra aligned parallel to the direction of movement was set as the reference.

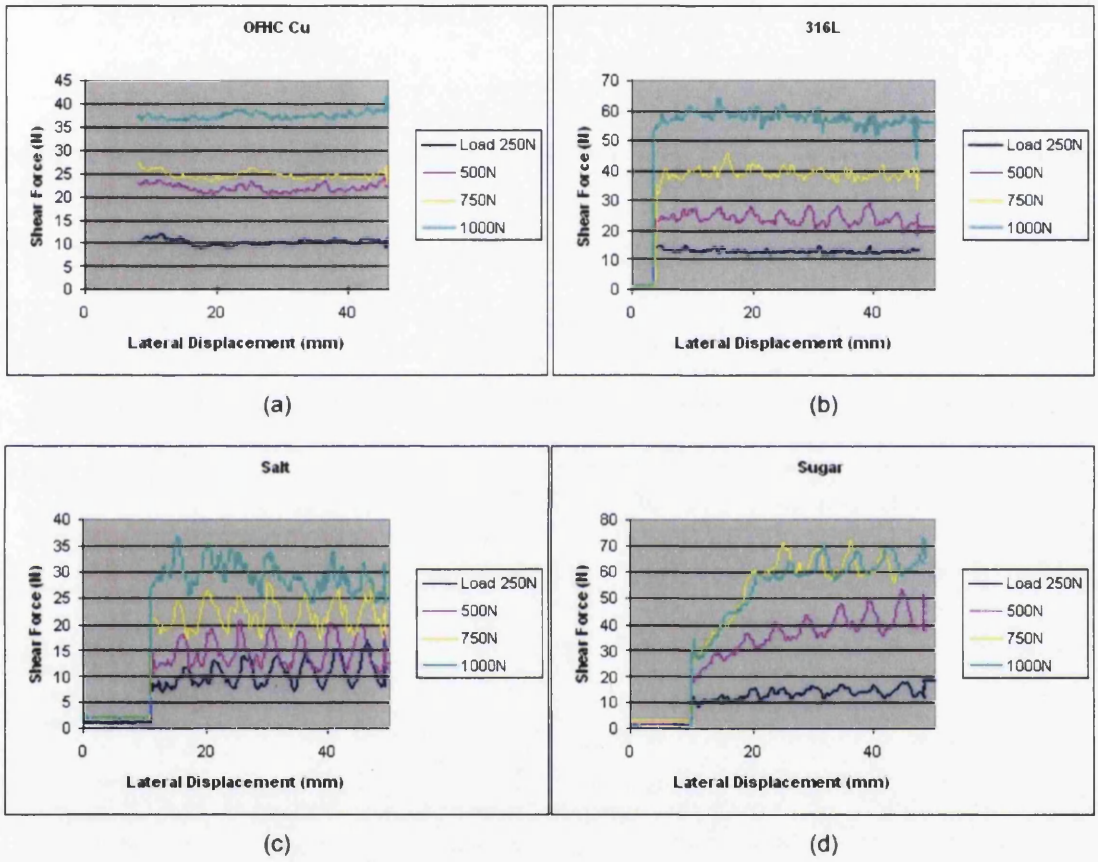

Figure 3. 10 Shear Force against Displacement at Different Loads (a) OFHC Cu (b) 316L (c) Salt (d) Sugar with Ra = 1.0 μm

Examining the graphs in Figure 3.10, OFHC Cu produced the most regular result with the least fluctuation. 316L also showed consistent results. However, in cases of Salt and Sugar, which are brittle materials, the results exhibit fluctuation and each material had a distinct characteristic.

First, in case of copper, the shear force increased rapidly and reached the maximum static friction. Then it had a further gradual increase in dynamic friction (around 70N from Figure 3.11(a), Ra = 1.0 μm Aligned to the target surface) and it eventually settled. The graph in Figure 3.10(a) was from a first batch of copper powder and low shear force levels can be observed comparing to other experiments with a fresh copper powder. This is illustrated to a high level of oxidisation on this powder sample.

For 316L powder, maximum static friction was reached with a very sharp increase, which was followed by a slight decrease in dynamic friction. Same build up in shear force fluctuation can be observed around the displacement of 15mm, which may be due to the powder encountering a clean target surface.

For the two brittle materials, a smoother increase in static friction was first observed. By closely examining Figure 3.10(c), no static friction was present for salt, where the process moved directly to dynamic friction. Then the stick and slip behaviour was exhibited. This can be observed from the process where the initial increase in shear force was followed by a slight decrease in which fresh surface seems to appear (around 11 mm of displacement). Graphs of sugar showed a similar behaviour to salt with a more gradual increase in shear force after fresh surface was introduced. Both brittle powders produced larger fluctuations than ductile materials at the settling phase, which was because of the stick and slip response.

As expected, a higher normal load, led to a higher shear force and all graphs show approximately equispaced shear force increase with load variation which means the coefficient of friction was a constant value in all cases.

3.3.5.2 Surface Finish

Surface finish effects were investigated in this chapter. D2 tool steel blocks with Ra of 1.0, 0.5, 0.25, and 0.1 μm were used as the target surface. The normal force was set to be 1kN.

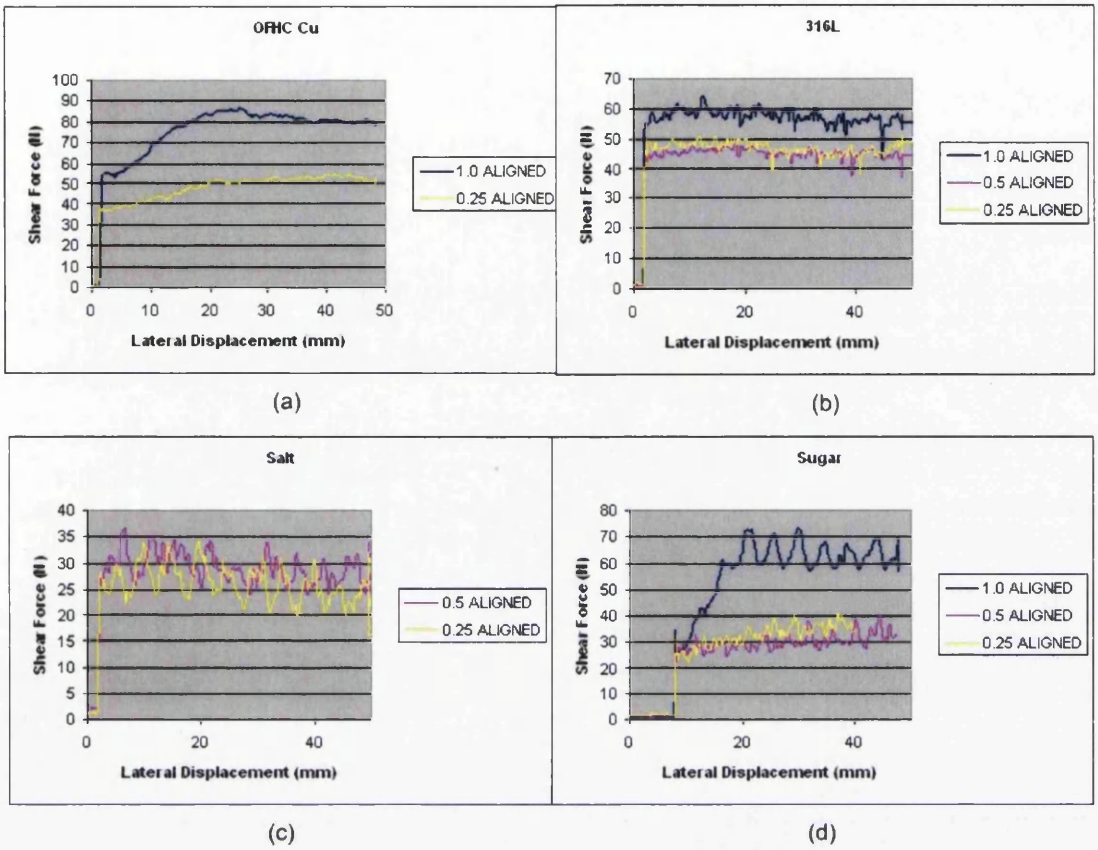

Figure 3.11 Shear Force against Displacement for Different Surface Finishes

(a) OFHC Cu (b) 316L (c) Salt (d) Sugar

Figure 3.11 shows four graphs of shear force against lateral displacement for different surface finishes. It can be seen, in general, that the roughest surface produced the highest shear force for all powders.

3.3.5.3 Surface Finish Direction

Experiments were also carried out with different direction of surface finish target blocks. There are two directions; one is parallel (aligned) to the movement of the moving block and the other, perpendicular (transverse). Again, the normal force was set to be 1kN for all experiments.

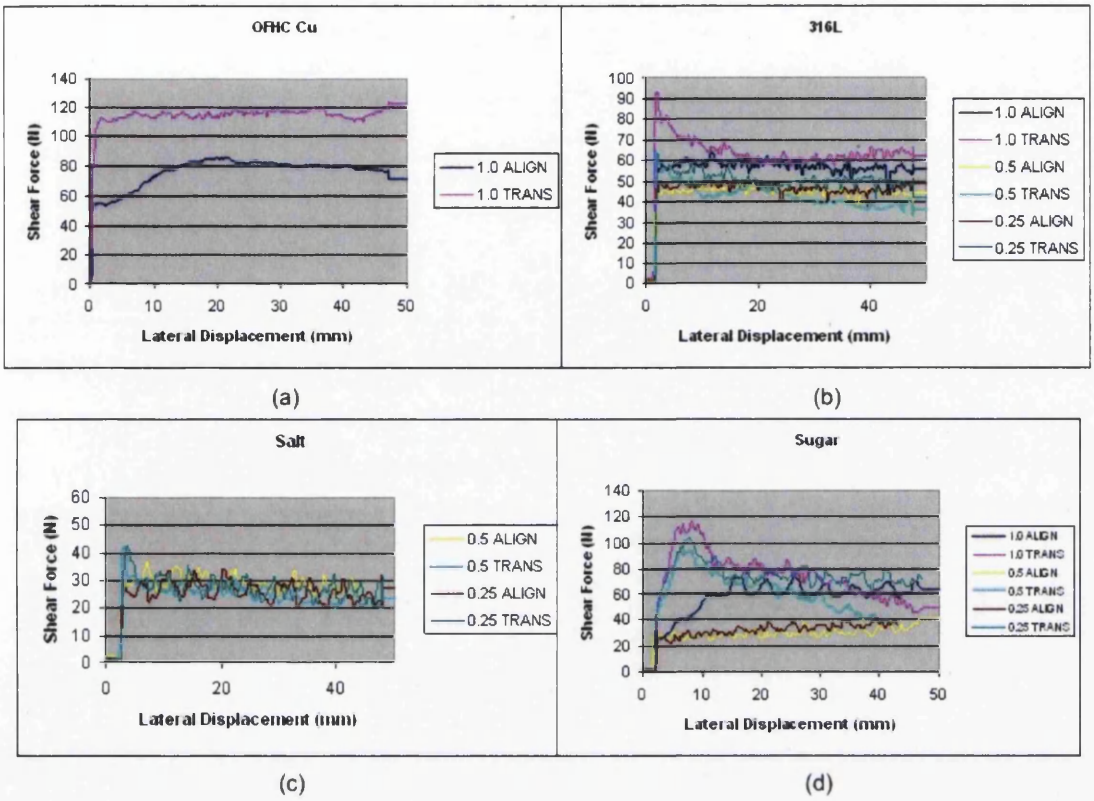

Figure 3. 12 Shear Force against Displacement for Different Directions of Surface Finish (a) OFHC Cu (b) 316L (c) Salt (d) Sugar

Figure 3.12 shows experiments with target surface transverse to the direction of the slide produced generally higher shear force, clearly shown in graph (a). Static shear forces in transverse directions were clearly higher than in aligned directions in all the powders. For most of the powders except OFHC Cu, dynamic shear forces in transverse directions were lower than in aligned directions. This is obvious since for target surface transverse to the direction of shear, powder particles are locked into surface grooves, where, for aligned target surfaces, particles just slide along the surface.

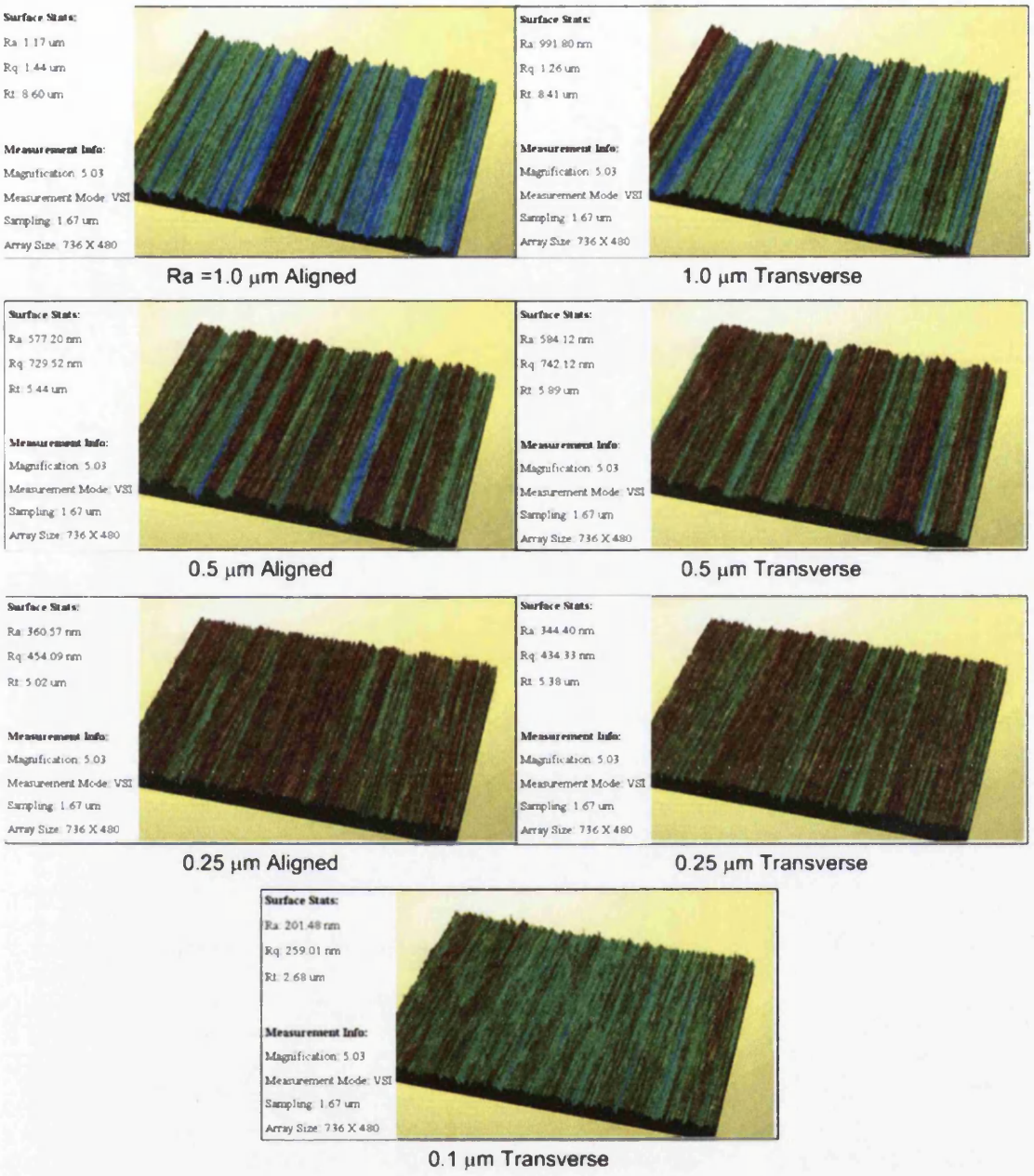

Figure 3. 13 White Light Images of Target Surfaces

Figure 3.13 shows the surface roughness images of different target surfaces used in the experiments. These images were taken by WYKO vision 32 from VEECO [Veeco Website, 2006]. Because they were prepared on opposite sides of the target surface, images designated as aligned and transverse are included.

3.3.5.4 Different Speed (Sliding Speed)

The default speed of the motor was set to be speed unit 8. In this chapter, each powder was experimented with same target surface but three different speeds, which are speed unit 6 (slowest), 8, and 10 (which were 0.7, 1.3, 2.2 mm/s accordingly). These speeds were calculated from overall distance travelled over the test time and therefore represent nominal values. Again, the normal load was set to be 1kN for all experiments.

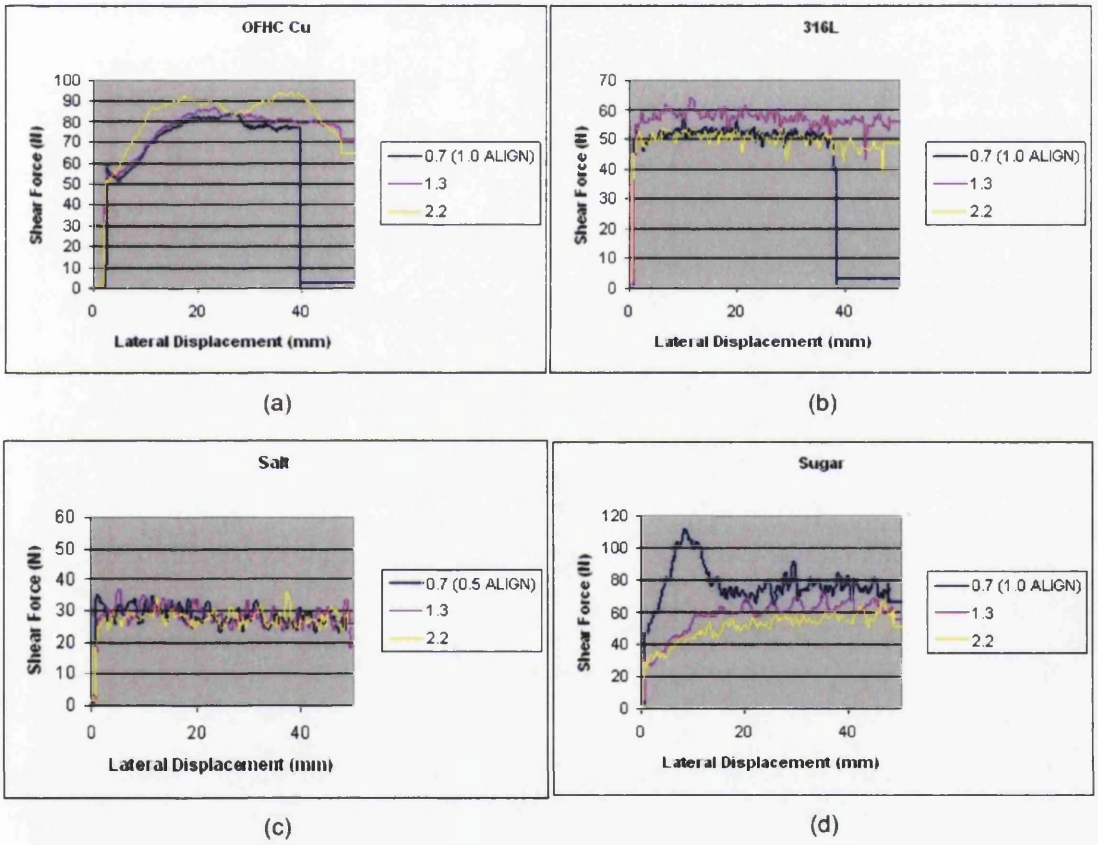

Figure 3. 14 Shear Force against Time for Different Linear Movement Speeds

(a) OFHC Cu (b) 316L (c) Salt (d) Sugar

Figure 3.14 shows shear forces against displacement for different sliding speeds. Obviously, as the speed of process increased the test time decreased. On the other hand, the shear behaviour exhibited a rate dependence. Observing (a) OFHC Cu, the shear force increased slightly as the linear speed increased. However, in (b) 316L and (c) Salt, there were only small differences. The case of (d) Sugar, it shows the opposite results from that of (a) OFHC Cu, decreasing shear force as the speed increased.

Examining the results reported in this chapter, mainly two friction mechanisms seem to be present even with low loads applied: particles sliding over the top of the groove of target surface and particles locked in the grooves. These mechanisms were identified in experimental work of [Strijbos, 1976]. It was reported that if the diameter of the particle is greater than surface roughness, the former mechanism takes place. This was observed frequently, where small difference between static and dynamic friction was shown (e.g. Figure 3.11). However, even though the ratio between them was significantly greater than 1 (at least 20 times greater for the smallest average size of particle on roughest surface), the latter mechanism seem to exist for transverse direction of target surface from the sharp decrease in dynamic friction (Figure 3.12(b)).

3.4 CLOSURE

The experimental procedure and work using extended sliding plate have been demonstrated in this chapter.

Experiments regarding control stabilisation, consistency, and data reduction have been reported. The results from these experiments were examined to

characterise friction between powders and target surfaces with the variation of different powders, loads, surface finishes, and speed.

Issues of importance in friction mechanism seem to be particle size, particle shape, material response (ductile or brittle), and surface topography (surface roughness). These issues will be further explored in numerical modelling chapters (4, 5, and 6) for ductile materials since they exhibited clearer friction mechanisms.

4

ATOMIC FORCE MICROSCOPY MODELLING

4.1 INTRODUCTION

The experimental work on a macro scale friction measurement was reported in Chapter 3. To investigate friction mechanisms from the experiments further, friction modelling work was carried out.

As reported in Chapter 2, there were two main methods of modelling the powder compaction process, macro-mechanical and micro-mechanical. The macro-mechanical model considers powder particles as a continuum and usually adopts the finite element method as the analysis tool [Riedel, 1992] and therefore models bulk behaviour of the powder. Such bulk behaviour is captured by a material model embodied into the simulation. In micro-mechanical modelling, powder particles are treated individually and are modelled using discrete simulation techniques [Gethin, 2003]. In this case, material properties are those of the powder component.

Although the microstructure of engineering materials is discontinuous, for many engineering problems they can be described as continuous (macro-mechanical models) since large enough quantities of materials are considered. However, a more detailed understanding of macro-scale behaviour may be derived through application of micro-mechanical analysis principles.

The current chapter focuses on modelling at the particle scale with emphasis on Atomic Force Microscopy (AFM) as a means of characterising particle properties. AFM provides a measurement technique to explore interaction at the particle scale when the usual silicon tip is replaced with a particle – referred to as a colloid probe [Bowen et al, 2001]. Factors that affect probe response are not fully understood and simplifying assumptions are often made. The calibration of an AFM involves stiffness calibration as well as detector calibration, where the latter focuses on the optical path [Beaulieu, 2007]. At present, many of the AFM experiments are performed with a set stiffness value provided by the manufacturer of the cantilever and sensitivity of the detector. The latter is required for converting

voltage output into deflection and given deflection and cantilever stiffness, this can be used to estimate force.

Although procedures for normal force calibration are becoming more established, considerable discrepancies still exist [Clifford, 2005]. In the case of Lateral Force Microscopy (LFM), further difficulties are encountered and there are no acknowledged and widely accepted methods of calibrating the probe in this mode.

Modelling the probe response forms a potential solution to this issue and this will be investigated in this chapter.

The key focus of this chapter is to build a model to simulate operations of the AFM incorporating the colloid probe system to explore parameters that affect it and investigate how it may influence measurements and outcome. Although the chapter is not intended to serve as a study of the finite element method, the use of finite element simulations will obtain an understanding of AFM response. This will aim to establish a tool and quantify parameter influences that are currently understood in a qualitative manner. The software used for the simulation was a finite and discrete element package ELFEN v3.0.4 from Rockfield Software [ELFEN, 2001]. Models for general compaction and friction simulation based on discrete element simulations will be presented in Chapter 5 and 6.

In order to calibrate stiffness, definitions of normal and lateral stiffness are required. For normal stiffness, it is straight forward as stiffness is just the ratio of force to deflection in the normal direction. There are a number of ways of determining this [Clifford, 2005] and this has now led to standard procedures that depend to some extent on the final application. However, in the case of lateral stiffness, it may be defined in a number of ways. This includes definitions based on a plain lateral movement, torsion or more realistically a combination of deflection in the lateral direction and slope due to torsion. Lateral deflection will influence the optical path for the detector, but this is likely to be secondary in comparison with torsion. However, since results accuracy in the normal mode may be improved through refinement of the optical analysis [Beaulieu, 2007] and so it is anticipated

that detail understanding of AFM response to lateral load will lead to improved resolution and ultimately standard calibration procedures coupled with the ability to account for surface topography in analysing experimental data. To date, the lateral mode has received less attention and so the purpose of this chapter is to explore the lateral mode response for simple beam and V-shaped cantilever designs to quantify the influence of parameters on probe response. This will be achieved through application of finite element modelling [ELFEN, 2001].

The following sections summarise how models may be built using this system. The steps are generic and may be summarised as:

1. Define Geometry
2. Define Loading
3. Define Constraints
4. Select Material Properties
5. Generate Mesh
6. Define Contact Model

These will be described further below.

4.2 MODEL CHARACTERISTICS

The AFM is a unique instrument that functions both as a topographical imaging device and a force sensor with nano-scale resolution. The AFM may be operated in a number of modes, contact, non-contact and tapping, each of which is aimed at specific applications [Veeco website, 2006]. The tip at the end of a

microscope cantilever is systematically scanned across a surface to generate a topographical image. When operating in contact mode, as the tip travels along the surface, the forces between the tip and the surface cause the cantilever to twist or/and bend dependent on scanning direction. A laser beam is reflected from the gold-coated back of the cantilever onto a position sensitive photodiode [Bowen, 2001]. Further details of AFM measurement principles are presented in Appendix A.2.

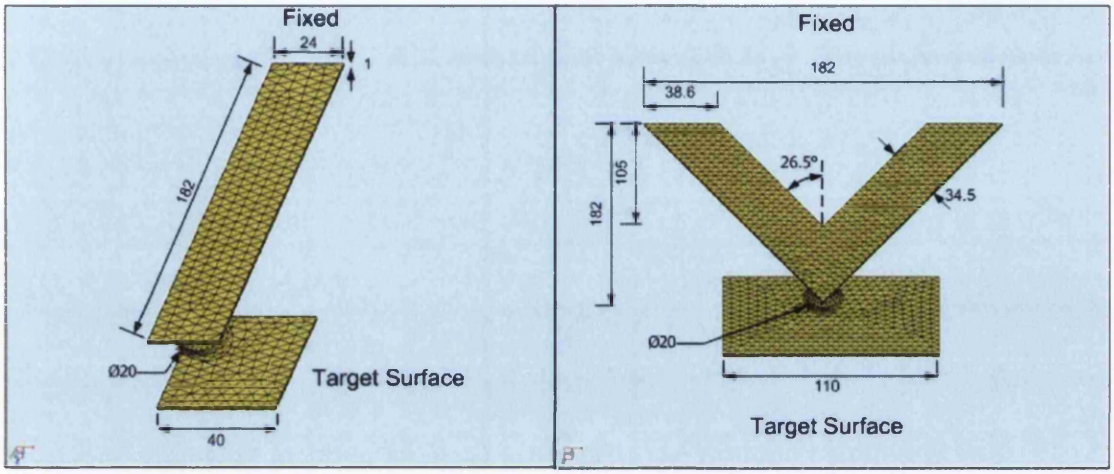

Figure 4. 1 Geometries of (a) *Rectangular Beam (b) V-Shaped Cantilever (dimensions in μm)*

Cantilevers are components that operate within an elastic regime, having a range of designs such as simple beams and V-shapes. The aim is to capture their geometry and compute deflections and to explore response in normal and lateral mode, the latter to estimate friction. The dimensions for the colloid probe models in section 4.3.3 therefore were from the actual cantilever used in the Veeco Model Dimension 3100 AFM [Veeco website, 2006].

Simulation needs to reflect the operation of the AFM. In this instance, the AFM is operated in contact mode and hence the target surface is brought into contact with the probe tip, displacing it. Reflecting this, loading was in the form of applied displacement of the target surface.

For boundary conditions, the mounting ends of the cantilevers are fixed in displacement in all directions and the contact model between the colloid probe and target surface was defined separately.

For colloid probe operation, generally, material properties corresponding to the powders used in the experiments described in Chapter 3 was selected for the particle, and the cantilever was made from silicon nitride. In this case, the influence of the gold reflecting layer on the back of the cantilever was excluded from the analysis, however the cantilever can be modelled as a bimetallic strip if this is required. The AFM tip is measured in terms of micrometers as shown schematically in Figure 4.1. The geometry was constructed in terms of micrometers and material units defined appropriately. This avoids the problem associated with meshing very small geometries in which solution accuracy will be affected by the computing resolution as a consequence of very small element dimensions.

The force against displacement and force against slope data are the key results for calibration. For normal mode, force against displacement data gives the stiffness parameter, which is critical for calibration of AFM response. A similar analysis may be carried out for the lateral mode, but a variety of lateral stiffness definitions is reported in the literature [Neumeister, 1994]. Force against slope at the cantilever tip is important for both modes since the AFM obtains the deflection of the cantilever by reflecting a laser beam off the back surface and the slope is the principal factor in determining the beam path. This is especially the case for the lateral mode where a number of studies [Green, 2004] highlight this as the method of estimating the mechanical component for calibration.

4.3 AFM RESPONSE

Within the software adopted for this work [ELFEN, 2001], there are two modes in which finite element simulations may be used to undertake modelling of

the cantilever: implicit and explicit. The implicit mode was selected because exploring the calibration of the probe response is the key objective and its formulation leads to a direct analysis of cantilever deflection. The implicit formulation within ELFEN also has the capability to simulate simple contact phenomena. Additionally, a three-dimensional model is preferred for better understanding. Explicit mode is a physically appropriate option that may be used to capture more complex contact phenomena in which significant deformations take place, but it requires very small time steps to maintain computational stability.

The following sections will explore the response of the AFM for a range of operating scenarios that will include design, colloid tip material properties, and operation under normal and lateral contact mode.

The materials properties used in this simulation are itemised in Table 4.1 below [Ultra Hard Materials, 2006] [Khan, 2004] [ASM Metals Handbook, 1986].

Part	**Material**	**Young's Modulus** $(N\mu m^{-2})$	**Poisson's Ratio**
Cantilever	Silicon nitride	0.28	0.2
Tip (Colloid probe)	316L	0.2	0.3
	OFHC Cu	0.115	0.35
Target surface	Steel	0.2	0.3

Table 4. 1 Material Properties of Parts in Friction Modelling

4.3.1 Cantilever Beam Model Calibration

As explained in section 4.2, the model output can be expressed in terms of stiffness and force-slope relationships. The simple cantilever design allows an analytical solution based on simple bending and torsion models for both parameters in both normal and lateral mode. This solution is subject to the assumptions embodied into the simple bending and torsion models and so may be considered as 'first order'. There is increasing evidence that for improved accuracy in normal mode operation, more complex models of optical sensitivity are required [Beaulieu, 2007] and this will need to be augmented by better models for normal stiffness. This is likely to be even more important in lateral measurement operation. However, such first order models provide a datum and allow comparison with a finite element model as a means of initial comparison for calibration.

As a vehicle for exploring the models, a simple rectangular beam is considered having a sharp tip. Experimental data from [Liu, 1994] is chosen for this purpose and therefore the three-dimensional beam is designed with the geometry summarised in Figure 4.2 below.

For small deflection of the rectangular beam cantilever, the normal and lateral stiffness can be calculated using the equations:

$$k_n = \frac{3EI}{L^3} \tag{4.1}$$

$$k_l = \frac{GK}{t^2 L} \tag{4.2}$$

where k_n and k_l are the spring constant in the normal and lateral direction

E is the Young's modulus

I and K are the second moment of area of the cross section

$$(K \approx \frac{wh^3}{16}\left(\frac{16}{3} - 3.36\frac{h}{w}\right), \text{ for } h \ll w)$$

L is the beam length

w is the beam width

h is the beam thickness

G is the Shear Modulus $\left(\frac{E}{2(1+\nu)}\right)$

t is the height if the tip

Equation 4.1 is based on a simple deflection model and 4.2 on a torsion type equation that excludes any lateral deflection effects.

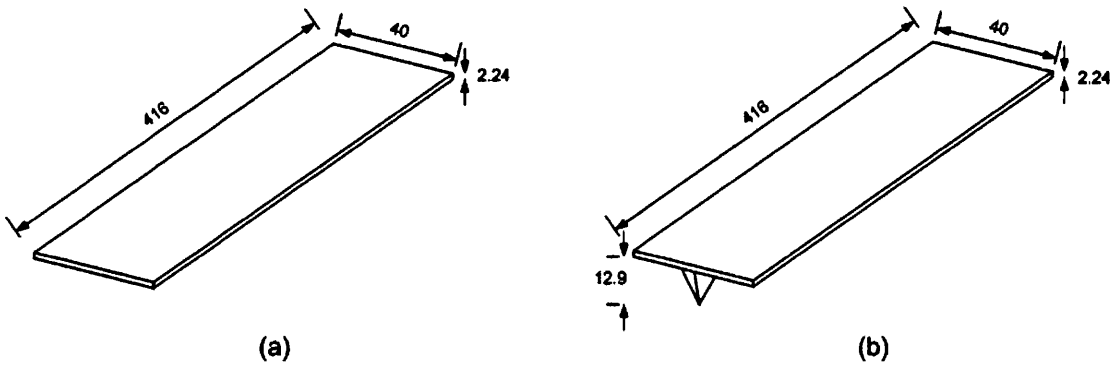

Figure 4. 2 Geometries of Cantilever Beam Model Calibration (a) Normal (b) Lateral Mode (μm)

In this calculation and for the purpose of comparison rather than establishing the characteristics of the AFM probe, a Young's modulus of $E = 0.2N/\mu m^2$ and Poisson's ratio of 0.3 (typical of steel) were used in the model.

The main difficulty that arises in obtaining stiffness data from the FE analysis is the issue of lateral stiffness. For normal stiffness, only bending of the cantilever is considered but in the case of lateral, it is complicated since it can be a combination of lateral movement as well as twisting and there is a difficulty in separating these.

In order to incorporate both bending and twisting of the cantilever, load was in the form of applied displacement at the end of the tip. Lateral stiffness was obtained by the distance the tip end travelled and the reaction force in the lateral direction at the other end of the cantilever, which is fixed. Although twisting is reported to be the main factor, lateral bending of the cantilever is included by the use of this method.

From calculation in which a small displacement of 10 μm was applied, the normal stiffness was found using equation 4.1 to be $k_n = 0.312\times10^{-6}N/\mu m$, and $k_n = 0.353\times10^{-6}N/\mu m$ from the simulation (Figure 4.2(a)). In addition, the lateral stiffness, based on twisting, was $k_l = 0.161\times10^{-3}N/\mu m$ from the equation 4.2 and $k_l = 0.106\times10^{-3}N/\mu m$ from the simulation with geometry shown in Figure 4.2(b), where the displacement was applied at the end of the tip. The differences between them are 12, 35 percent respectively. The greater difference in lateral stiffness is due to neglecting lateral deflection from the equation 4.2, but for cantilever beam model it is argued that lateral deflection (bending) cannot be ignored. This will be explored further in the section for shear interaction with a colloid probe model (Figure 4.18).

There are a number of potential reasons for the discrepancy that include model discretisation and the representation of the physics of the process. To explore the differences that may arise from discretisation, simulation for the simple beam with geometry shown in Figure 4.2(a) was undertaken and the results from this are itemised in Table 4.2.

Mesh Generation Method	**Division Dimension (μm) (Width/Length/Thickness)**	**Output (Normal Stiffness (N/μm))**
Structured	2 : 2 : 2.2	0.466×10^{-6}
	1 : 2 : 2.2	0.457×10^{-6}
	2 : 2 : 0.7	0.430×10^{-6}
	1.3 : 2 : 0.7	0.427×10^{-6}
	1 : 1.1 : 1.1	0.353×10^{-6}
Unstructured		0.512×10^{-6}

Table 4. 2 Investigation of Division Dimension ratio in Structured and Unstructured Mesh for the Simple Beam Tipless Cantilever

The finer meshes tend towards a stiffness of $0.353\times10^{-6} N/\mu m$ and a structured mesh comprising near cubic elements yields the best result. The unstructured mesh produced a slightly higher stiffness value compared with that of the structured counterpart. This is mainly due to the number of elements through the thickness of the beam and ideally, at least two should be used. For the unstructured mesh model having two layers through the thickness was computationally prohibitive and led to simulation failure due to the discretisation and a high element count. However, while noting this difference, the unstructured mesh system will be used later since it allows discretisation of a colloid probe,

including the particle attached to the tip. The remaining discrepancy between the simulation and stiffness based on a simple beam bending model may be attributed to a more accurate representation of the physics. This is a point made in [Clifford, 2005] for analysis of normal stiffness calibration, in that the FE model does not embody the assumptions that are required for the simple bending model, thus it may be described as 'ab initio', and the most accurate.

The slope of the deflection was also derived at the end of the cantilever and for a plain beam cantilever, an approximate value may be derived from simple bending theory. Because of the uncertainty of the location of the laser reflection point [Beaulieu, 2007], in the numerical simulation, sections are investigated through nodal interrogation. Exploration of slope calculations will be discussed further in connection with the model for V-shaped cantilevers since it is more aligned with the AFM experiments undertaken within this work.

It is interesting to note that the AFM beam cantilever is significantly more sensitive in the normal mode (about 300 times for the case study set out above) confirming its ability to resolve normal forces more accurately, but at the same time limiting its ability to apply load when it is used in for example an indentation experiment. Lateral sensitivity could be enhanced by effectively turning the cantilever and optical sensor arrangement through 90°.

4.3.2 Cantilever V-Shaped Model Calibration

Calibration for the V-shaped cantilever may be obtained from equations by [Neumeister, 1994] and [Noy, 1995].

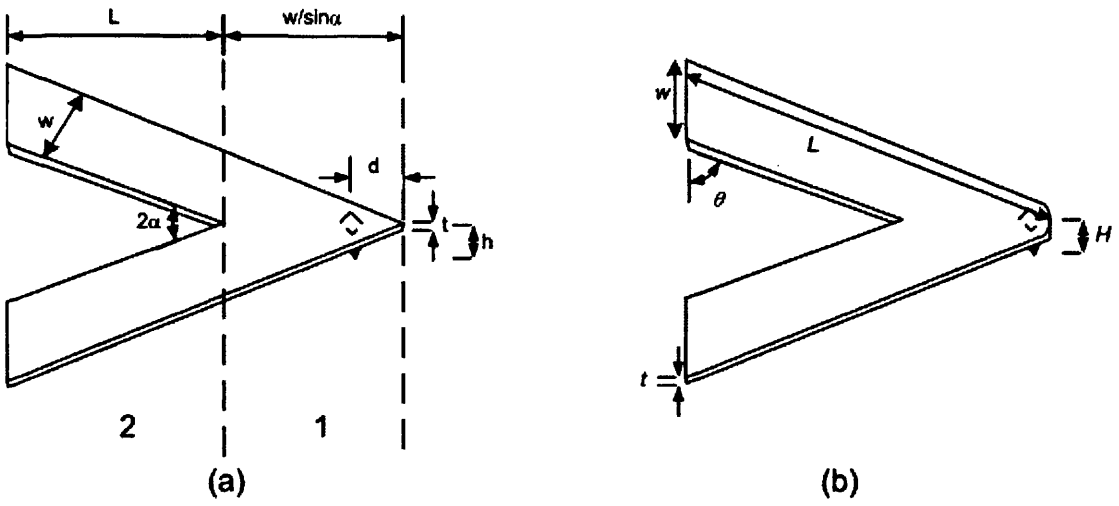

Figure 4. 3 Geometries of (a) [Neumeister, 1994] (b) [Noy, 1995] Model

The normal stiffness constant was derived by [Neumeister, 1994] for a 'V' configuration as the sum of three parts, the deflection of a clamped triangular plate (Δ_1), the end deflection of the two beams (Δ_2), and rotation (θ_2, i.e. deflection angle in normal direction), shown in Figure 4.3(a). This has led to the equation:

$$\Delta_N = \Delta_1 + \Delta_2 + \theta_2 \times \left(\frac{w}{\sin\alpha} - d \right) = N \frac{1}{k_n} \tag{4.3}$$

where

$$\Delta_1 = \frac{3N}{Et^3 \tan\alpha} \left[\left(\frac{w}{\sin\alpha} - 2d \right)^2 - d^2 \left(2\log \frac{w}{d \sin\alpha} + 1 \right) \right] \tag{4.4}$$

$$\Delta_2 = \frac{NL^2}{Ewt^3 \cos^2\alpha} \left(\frac{2L}{\cos\alpha} + 3\left(w\cot\alpha - d\cos\alpha - r\sin\alpha \right) \right) \tag{4.5}$$

$$\text{with } r = \frac{L\tan\alpha + (w - d\sin\alpha)(1-\nu)\cos\alpha}{2 - (1-\nu)\cos^2\alpha}$$

$$\theta_2 = \frac{3NL(1+\nu)}{Ewt^3 \cos\alpha} \left(\frac{w}{\sin\alpha} - d + r\cot\alpha \right) \tag{4.6}$$

where, N is the force applied at the end of the cantilever to induce normal deflection of the device.

E is the Young's modulus

ν is the Poisson's ratio

Using his equations resulted in the normal stiffness constant $k_n = 1.453\times10^{-6} N/\mu m$ for the cantilever dimensions shown in Figure 4.4(a) below ($N = 0.0126\times10^{-3} N, E = 0.2N/\mu m^{-2}, \nu = 0.3$).

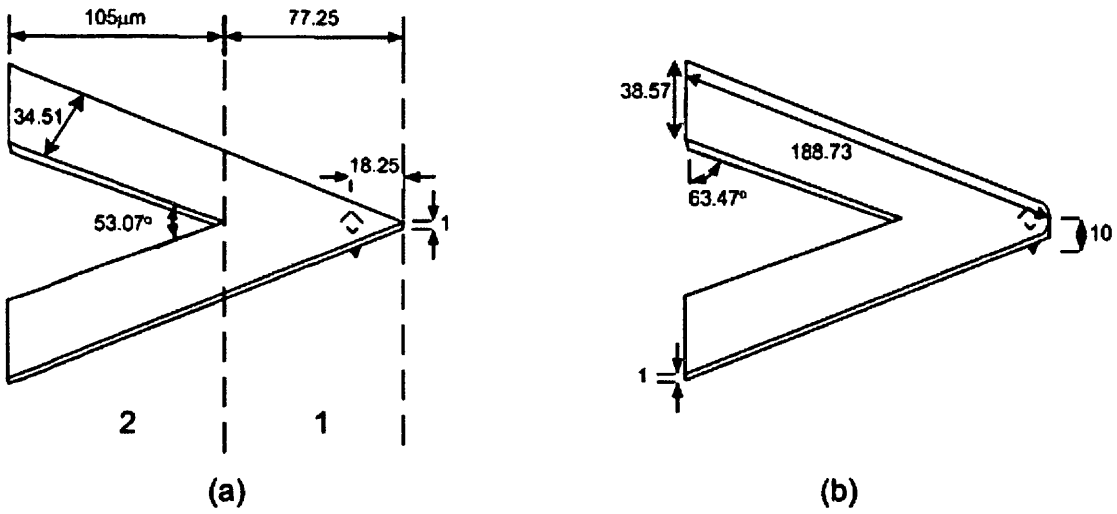

Figure 4. 4 Dimensions of Calibration using (a) [Neumeister, 1994] (b) [Noy, 1995] Model

[Noy, 1995] also reported an approximation of k_n as a sum of the normal stiffness constants for two rectangular beams, equation 4.7. From the dimensions in Figure 4.4(b), the normal stiffness constant is found to be $k_n = 0.574\times10^{-6} N/\mu m$ ($E = 0.2N/\mu m^{-2}, \nu = 0.3$).

$$k_n = \frac{Ewt^3}{2L^3} \tag{4.7}$$

The normal stiffness values from the two methods differ significantly which shows the discrepancy and hence difficulty in determining even these stiffness coefficients.

For comparison, an elastic model of the V-shaped cantilever was built with the dimensions shown in Figure 4.4 (also identical to the geometry shown in Figure 4.1(b) but with a cube shaped tip). To obtain best results, a very fine and structured mesh was used and the result is presented below in Figure 4.5, shown as a deflected cantilever.

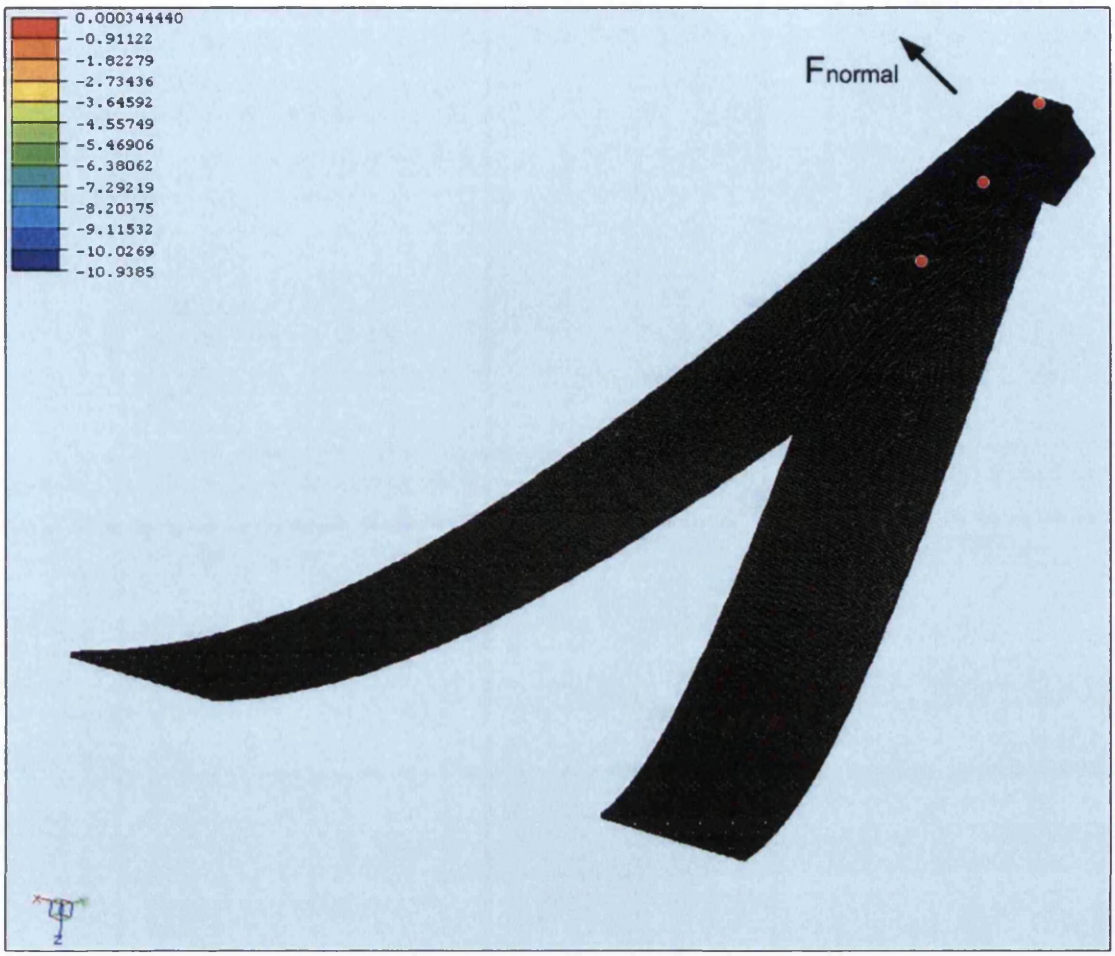

Figure 4. 5 Schematic Diagram of Applied Displacement for a V-Shaped Cantilever with Forces Applied in Normal Direction

From this model, the normal stiffness constant was found to be $k_n = 1.031 \times 10^{-6} N/\mu m$. This value lies between the results from previous methods and closer to the value from [Neumeister, 1994].

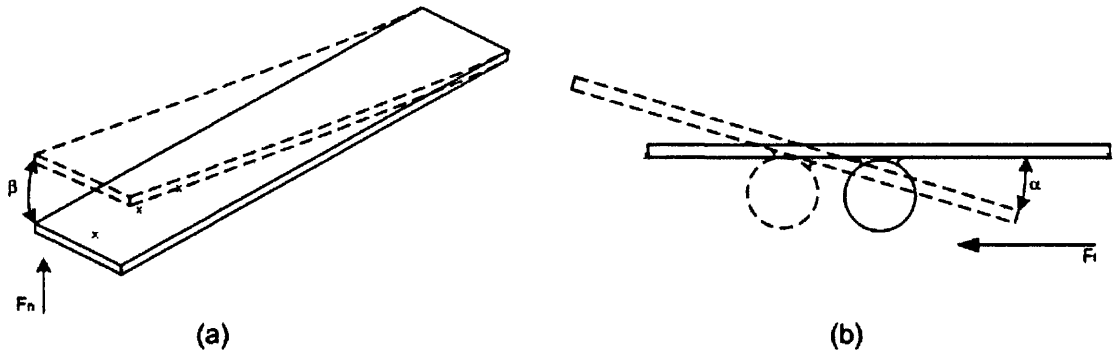

Figure 4. 6 Deflection Angles in (a) Normal (b) Lateral Direction

The force slope relationship was also investigated for both the beam and V-shaped models. Because of the uncertainty of point of reflection of the laser light off the back of the cantilever (or the need to account for it in the case of advanced optical models [Beaulieu, 2007]), a number of nodes were selected to calculate the slope. The resulting slope angle in the normal direction had similar results at the points shown in red in Figure 4.5, i.e. $\beta_1 = 5.48^\circ$, $\beta_2 = 5.43^\circ$ and $\beta_3 = 5.46^\circ$ for an applied displacement of $0.01\mu m$. The same procedure was repeated for the beam model in Figure 4.2, by selecting three nodes, red crosses, on top of the cantilever (Figure 4.6(a)). The angles were found to be $\beta_1, \beta_2, \beta_3 = 2.06^\circ$. Although difference between these angles may increase as the applied force increases, the difference is minimal and therefore two nodes that provide information to compute β_2 were selected to represent the point at which the laser beam is reflected.

For the lateral stiffness constant, [Neumeister, 1994] reported an equation based on the representation shown in Figure 4.3(a). The slope analysis was divided into two, the twist of the triangular plate and that of the beams. From the total rotation of these two parts, a torsional stiffness constant was calculated following which, the lateral stiffness constant was derived.

$$k_l = \frac{Et^3}{3(1+\nu)h^2}\left(\frac{1}{\tan\alpha}\log\frac{w}{d\sin\alpha}+\frac{L\cos\alpha}{w}-\frac{3\sin 2\alpha}{8}\right)^{-1} \tag{4.8}$$

From this equation, the lateral stiffness constant was found to be $k_l = 0.143\times10^{-3} N/\mu m$. It is shown to be dependent on the cantilever design, but is particularly sensitive to the height of the tip (h).

Instead of a direct derivation of lateral stiffness constant, an equation relating both normal and lateral stiffness constants are reported in [Noy,1995]. The lateral force constant was expressed in terms of the normal stiffness constant. This was done based on a hypothesis that both forces originate from the breaking of intermolecular interactions, and it could avoid the difficulties in derivation of the lateral stiffness. Thus given the calculated ratio of normal to lateral stiffness and a good calibration of normal stiffness (including the optical path calibration) it was hypothesised that the lateral stiffness could be calculated. Then according to [Noy, 1995]:

$$k_l = \frac{2}{\left[6\cos^2\theta+3(1+\nu)\sin^2\theta\right]}\left(\frac{L}{H}\right)^2 k_n \tag{4.9}$$

By calculation from the geometry in Figure 4.4(b), the lateral stiffness was found to be $k_l = 0.133N/mm$.

Equation 4.9 is in principle similar to the key objective of this chapter. A more accurate representation will be attempted by utilising the finite element model application.

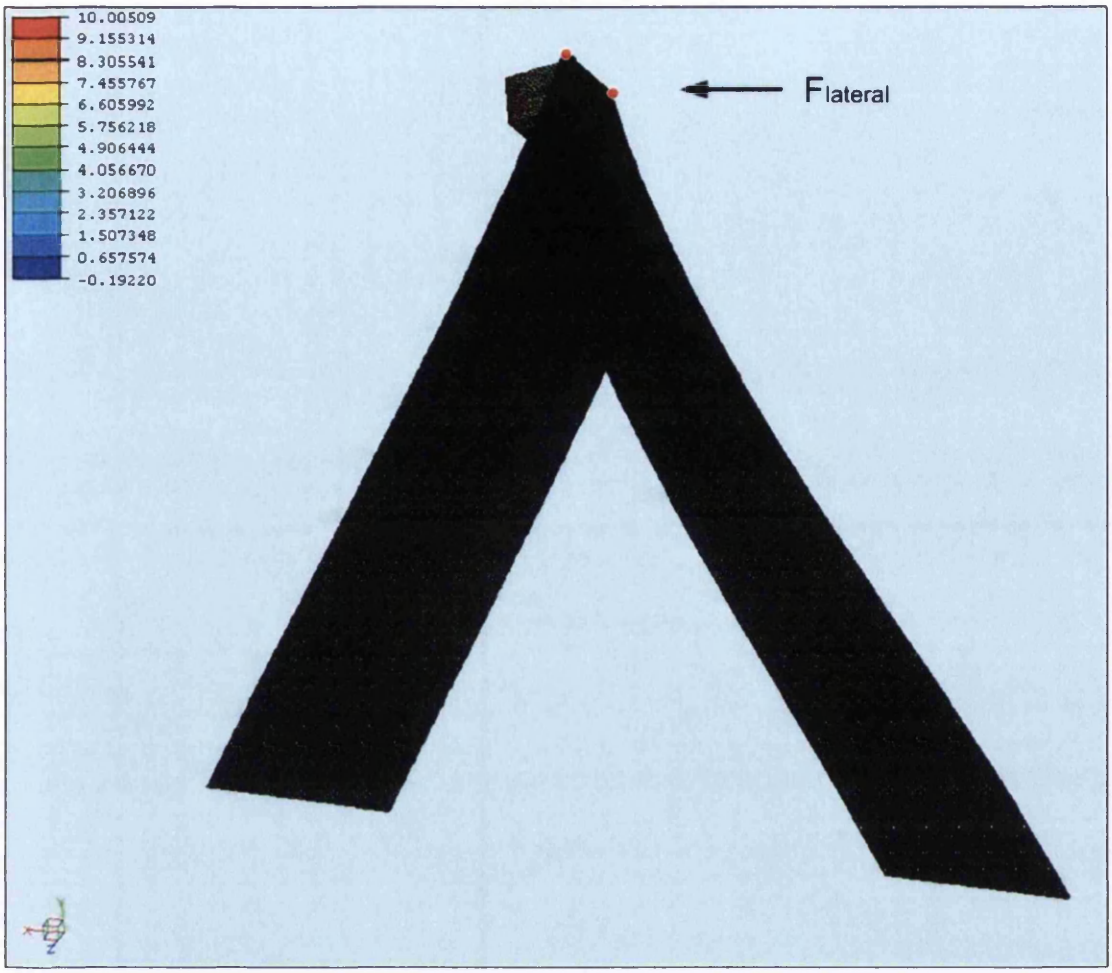

Figure 4. 7 Schematic Diagram of Applied Displacement for a V-Shaped Cantilever with Forces Applied in Lateral Direction

The resulting deformation from the simulation is shown in Figure 4.7 from which the lateral stiffness was found to be $k_l = 0.123N/mm$. This lies between the values derived from application of equations by Noy and Neumeister.

The calibration of the V-shaped cantilever is compared below in Table 4.3.

	[Neumeister, 1994] Method	[Noy,1995] Method	Finite Element Model
Normal Stiffness ($N/\mu m$)	1.453×10^{-6}	0.574×10^{-6}	1.031×10^{-6}
Lateral Stiffness ($N/\mu m$)	0.143×10^{-3}	0.133×10^{-3}	0.123×10^{-3}
Ratio of Lateral / Normal Stiffness ($\frac{k_l}{k_n}$)	98.42	231.71	119.30

Table 4. 3 Summary of Stiffness Calibration for a V-Shaped Cantilever

As it can be observed from Table 4.3, the stiffness derived from the finite element model achieved best agreement with the approximations proposed by Neumeister. Since the FE model is more free from simplification, it can be used to establish the mechanical component of normal and lateral stiffness data for the AFM.

The normal to lateral stiffness ratio ($\frac{k_l}{k_n}$) of the methods were compared and found that the FE model produced results that lie closest to the data by Neumeister.

4.3.3 Colloid Probe Model

A colloid probe model will be constructed to explore overall cantilever response to loading when assuming the geometries shown in Figure 4.1. First, a three-dimensional model of the simple beam with a spherical particle attached to the tip was considered as shown in Figure 4.1(a). The contact model was defined

between the tip and the target surface and the particle attached to the end was assumed to behave elastically. The target surface plate was then subjected to applied displacement in the normal direction. The surfaces at the mounting end of the beam cantilever were fixed at which reaction forces were then captured.

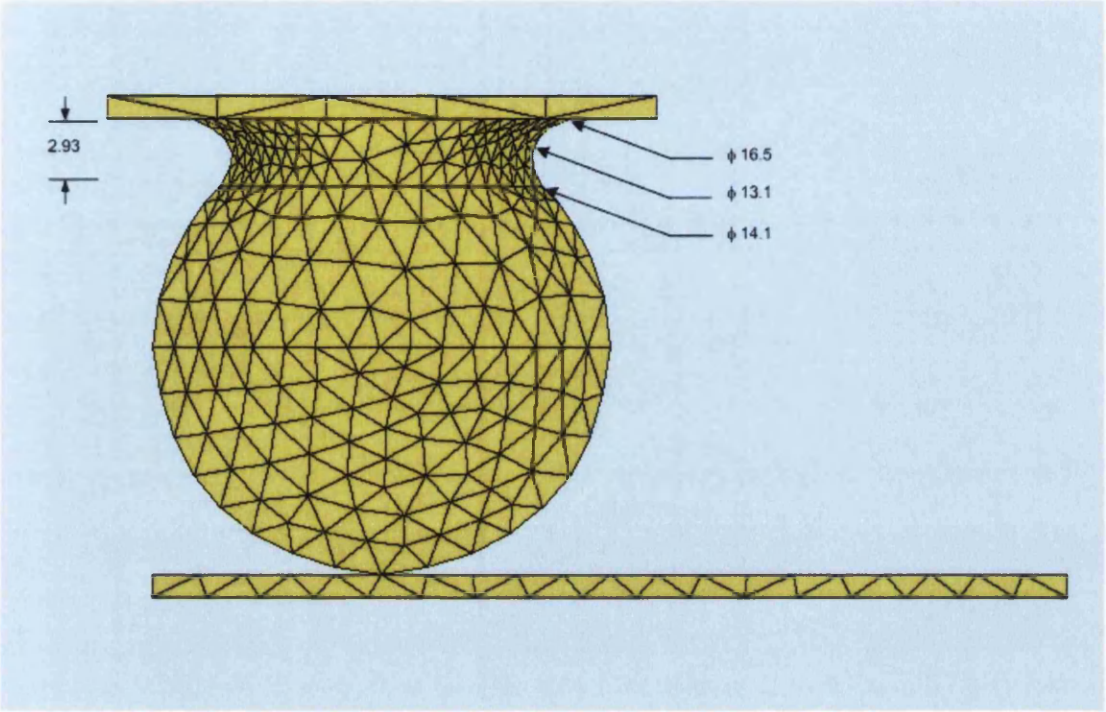

Figure 4. 8 Geometry of the Adhesive

The particle was attached to the end of the cantilever using a glass glue adhesive to form a colloid probe, (see Appendix A.2). The geometric representation is captured in Figure 4.8 that shows the finite element model at the probe tip. This figure also shows a range of neck radii that were investigated within the sensitivity case studies that will be described below. Although material properties of the glue are different, due to difficulties in defining geometry and mesh generation, it was regarded to have the same material properties as the particle included in the tip definition.

The loading for the colloid probe model was applied through the contact model, i.e. the target surface was constrained to move, to come into contact in the normal direction. The interactions in the normal direction are presented below for steel and copper particles fixed at the cantilever tip.

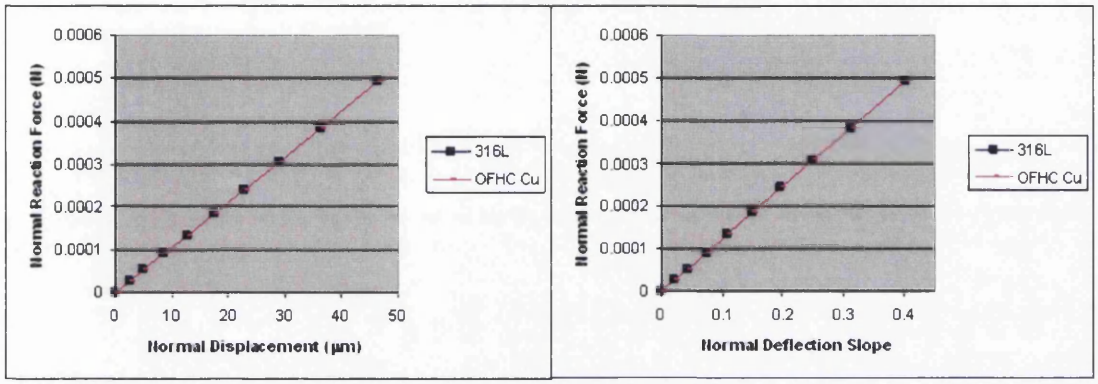

(a) (b)

Figure 4. 9 Graphs of (a) Normal Direction Reaction Force against Displacement (b) Reaction Force against Deflection Slope for both 316L and OFHC Cu Probes with Elastic Material Properties for Beam Model

As seen from Figure 4.9, the force deflection and slope are related linearly, confirming the elastic behaviour of the system. In addition, because the deflection of the cantilever is small, the contact patch does not move sufficiently to affect the normal direction mechanical stiffness of the system. Both graphs show very small differences between the two colloid probes even though the particles that form the probe have a significant difference in elastic modulus. For the particle material properties used, this confirms the dominance of material properties of the cantilever in determining the normal stiffness coefficient and this may be the main reason for choosing silicon nitride as the material for the cantilever for most AFM experiments reported up to date. However, this scenario may change in the event that very soft particles, such as biological materials, are attached to the cantilever.

A similar investigation was performed for the V-shaped cantilever.

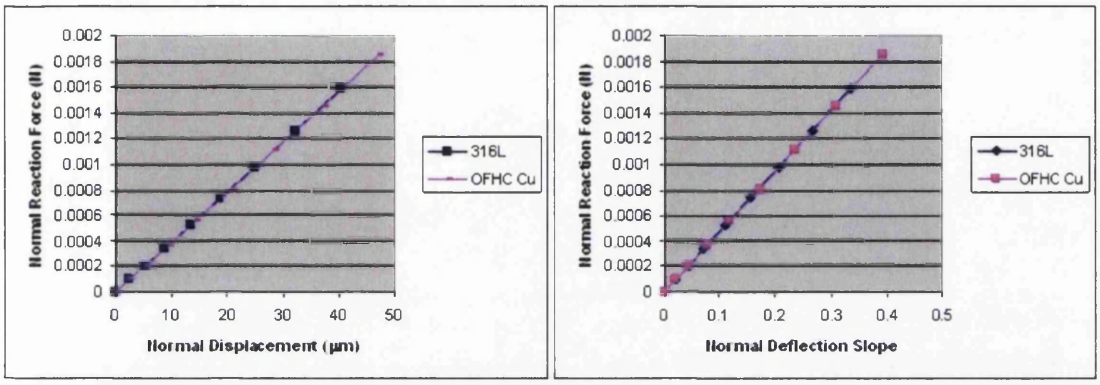

(a) (b)

Figure 4. 10 Graphs of (a) Normal Direction Reaction Force against Displacement (b) Reaction Force against Deflection Slope for both 316L and OFHC Cu Probes with Elastic Material Properties for V-Shaped Model

A similar linear relationship is exhibited, the V shaped cantilever has a high normal stiffness reflecting its more rigid construction.

Further models were developed in which the particle at the probe tip was assumed to deform plastically according to a yield model based on a von Mises criterion in which shear is assumed to be the dominant yielding mode. Although many ductile materials have non-linear hardening characteristics the von Mises model used has a linear approximation. The slope of the hardening curve was defined using the values in Table 4.4.

Material	Yield Stress ($N\mu m^{-2}$)	Hardening Modulus ($N\mu m^{-2}$)
316L	0.24×10^{-3}	0.44×10^{-3}
OFHC Cu	0.05×10^{-3}	0.44×10^{-3}

Table 4.4 Plastic Properties of Ductile Materials

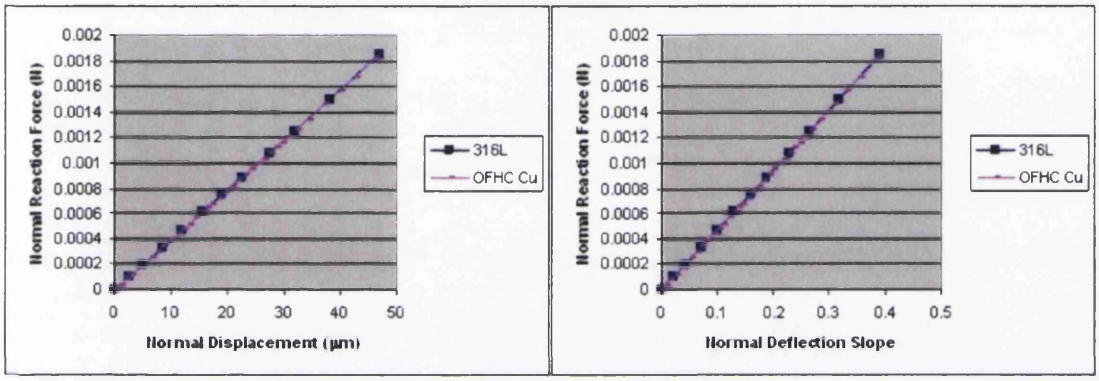

(a) (b)

Figure 4. 11 Graphs of (a) Normal Direction Reaction Force against Displacement (b) Reaction Force against Deflection Slope for both 316L and OFHC Cu Probes with Plastic Material Properties for V-Shaped Model

From Figure 4.11, it can be seen that including plasticity has a very small effect on stiffness. This is an expected result as the loads and deflections remain very small, even though there may be local yielding at the tip point in the contact and some areas of the glued joint as shown in Figure 4.12. The influence of plasticity on stiffness can be observed in Figure 4.13, where a very soft probe was used.

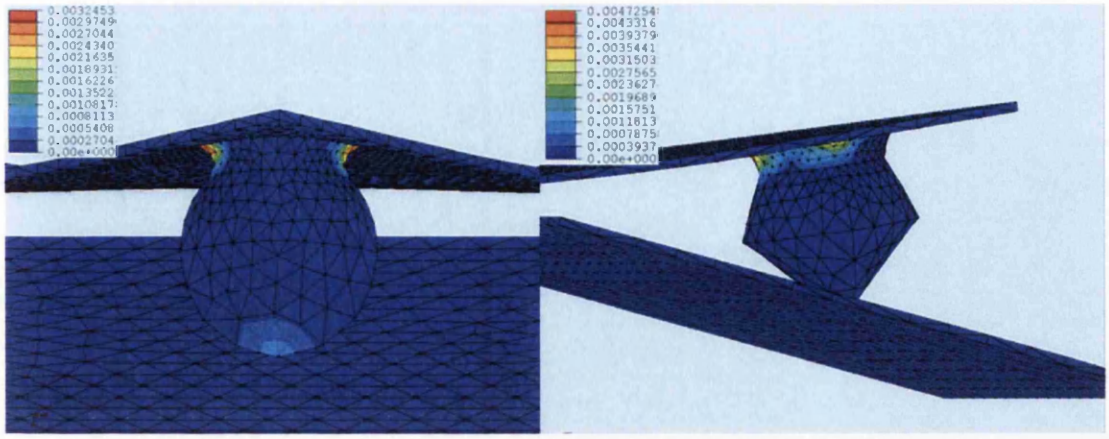

Figure 4. 12 Plastic Strain Zones for OFHC Cu (V-Shaped Model)

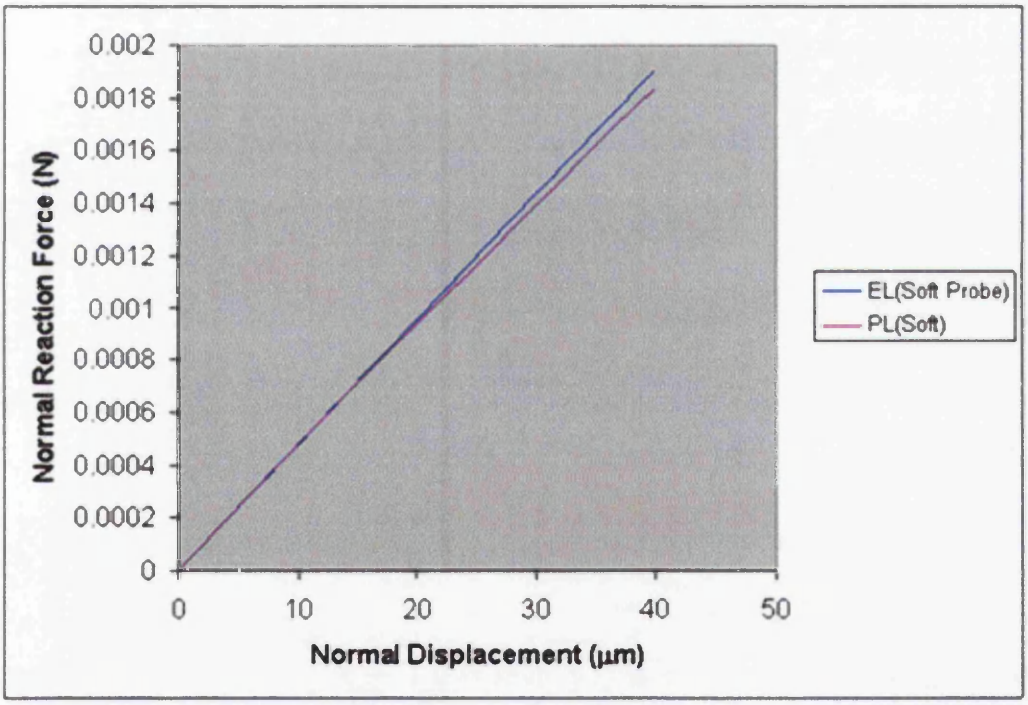

Figure 4. 13 Graph of Normal Direction Reaction Force against Displacement for a Very Soft Probe with Elastic and Plastic Material Properties for the V-Shaped Cantilever Model

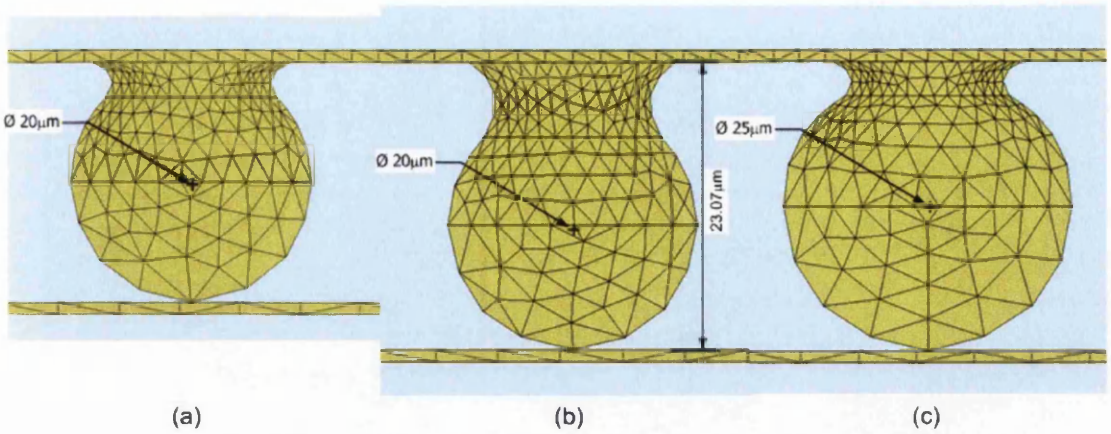

Figure 4. 14 Geometries of (a) Original (b) Larger Colloid Fixity (c) Larger Probe Particle

Factors that may affect normal deflection were also investigated (i.e. fixity geometry and size of colloid probe). However, since the material properties of the adhesive were not reflected in these models, but investigated purely in terms of geometry, exploration of one of the factors (size of colloid fixity) will be sufficient to show the effect of tip height on the deflection in the normal direction. The case study was modelled with elastic material properties since the effect of plasticity was negligible for the material used as reported above.

The model geometry shown in Figure 4.14(b) was chosen for comparing the effect of the tip height.

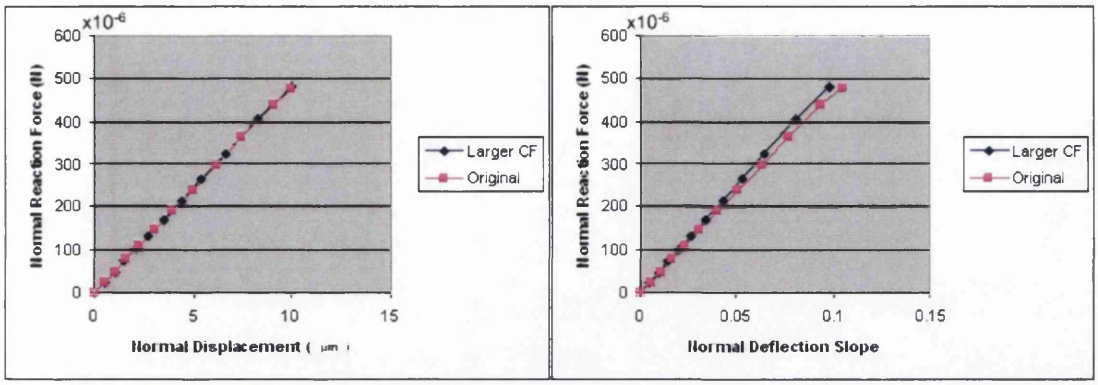

Figure 4. 15 Graphs of (a) Normal Direction Reaction Force against Displacement (b) Reaction Force against Deflection Slope for Original and Larger Colloid Fixities (316L Probe) with Elastic Material Properties for V-Shaped Model

Although only a very small difference was observed for the reaction force in the normal direction, the deflection slope increased in the case of the larger colloid fixity. This is because the larger the tip height, the greater the deflection angle in normal direction with same applied displacement on target surface, especially when the material properties of the cantilever is very influential. This is as expected and demonstrates the additional stiffening effect of the fixed region whereas for the smaller glued region there is more freedom for the cantilever end to deflect.

A case study of a cantilever engaging an inclined surface will give an insight to understanding the issue of linking normal and lateral sensitivity and their undesirable mutual dependence. This will be explored in the following section.

An inclined target surface is introduced to replace the horizontal target plate, see Figure 4.16. By bringing this vertically into contact with the probe, it will induce both normal deflection and lateral torsion. This model can also represent the sloping flank of a rough surface.

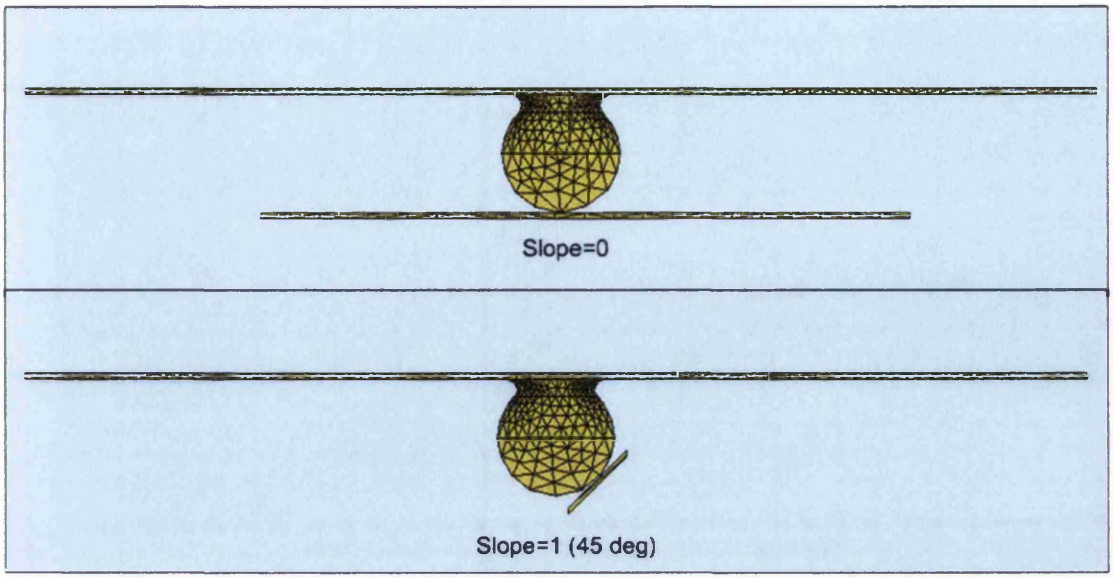

Figure 4. 16 Schematic Diagrams for the Inclined Surface Models

For both models, the contact model was defined separately between the probe and the target surface. The friction coefficient between the probe and the target surface was 0.1.

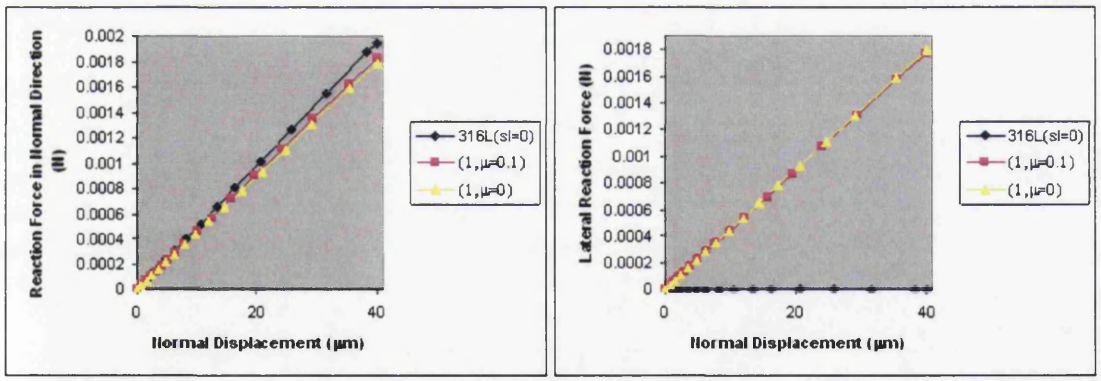

(a) (b)

Figure 4. 17 Graphs of (a) Normal Direction Reaction Force against Displacement (b) Lateral Direction Reaction Force against Test Time for 316L Probe on an Inclined Target Surface with Elastic Material Properties for a V-Shaped Cantilever

By examining Figure 4.17(a), it can be seen that the normal reaction force is nearly independent of the surface inclination. This is due to coefficient of friction of 0.1 being set between the probe and target surface and this constrains it to move through nearly the same distance as when the surface is not inclined. The slight reduction in displacement occurs because the probe now twists slightly and so the normal deflection of the beam is reduced. The inclination leads to significant changes in lateral force development as shown in Figure 4.17(b) due to resolution at the plate contact. As a further check, zero friction was applied at the tip contact and this led to identical normal and lateral load as the engagement proceeded. This is the anticipated result confirming the correctness of the model.

4.3.4 Shear Interactions

For both colloid probe models (i.e. cantilever beam and V-shaped), the shear interaction was explored for the geometries shown in Figure 4.1. Thus the colloid probe models used in the above section were extended to incorporate shear interactions. Models were developed to simulate a complete friction experiment through engagement of the probe, followed by its lateral movement against the target surface. The contact between the probe and the target surface was defined to have a friction coefficient of 0.1 as a datum. Additionally, since the material selection of the tip had only a very small effect on the results, 316L with the elastic material response was chosen.

With the lateral direction motion applied while holding the normal engagement constant, a complex response is observed for the probe. First twisting occurs due to friction between the colloid probe and the target surface that is reflected in a couple type reaction at the probe fixing point. This is followed by bending in the lateral direction that leads to the generation of lateral load and eventually it settles to the slipping stage at which point no further displacement (torsion and bending) occurs. By exploring the relationship between lateral force

against displacement and lateral force against slope, interactions of bending and twisting can be explored.

4.3.4.1 Cantilever Beam Model

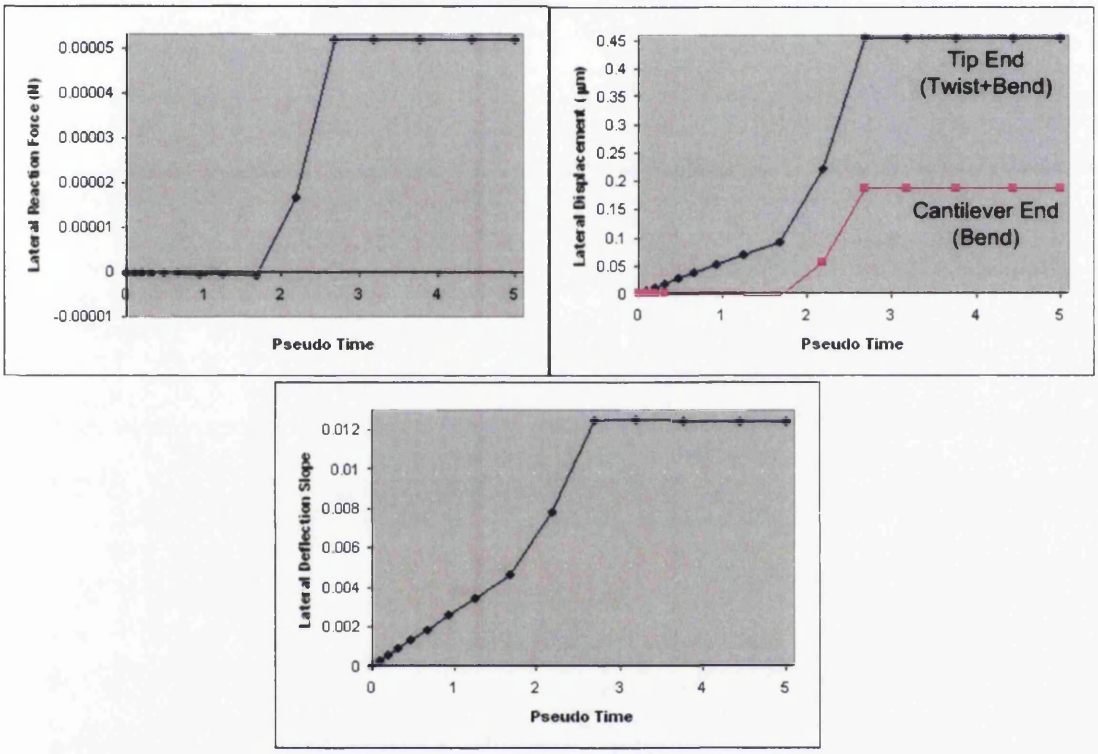

Figure 4. 18 Graphs of Reaction Force in Lateral Direction, Lateral Displacement on the Tip End, and Lateral Deflection Slope against Test Time for Beam Model (Left to Right respectively)

The displacement at the tip contact point was chosen as the main parameter in order to incorporate both twisting and bending of the cantilever. In order to differentiate between twisting and bending, displacement at the tip end and cantilever end at the tip fixing point has been plotted in Figure 4.18. It can be observed that for the beam type cantilever although twisting had a greater influence in shear interaction, bending was also significant accounting for about 45% of the

deflection. Bending will be expected to show much less effect for the V-shaped cantilever model shown in the section below.

4.3.4.2 Cantilever V-Shaped Model

The calculation principles for the beam cantilever model were extended to the V shaped geometry and the results from this series of simulations is presented below.

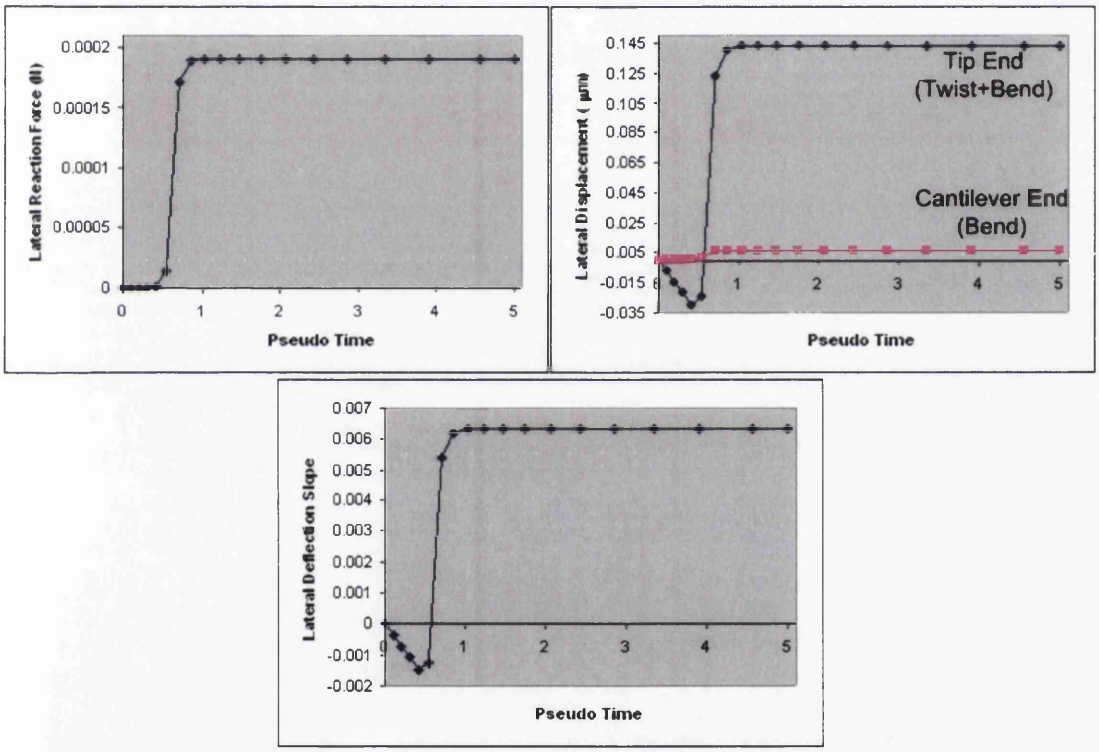

Figure 4. 19 Graphs of Reaction Force in Lateral Direction, Lateral Displacement on the Tip End, and Lateral Deflection Slope against Test Time for V-Shaped Model (Left to Right respectively)

Figure 4.19 shows the lateral response of the V-shaped cantilever. In this instance sliding at the tip starts at 1 time unit and lateral loading starts to be

generated following its application at 0.5 units. This pattern reflects the results for the simple beam arrangement. The displacement of tip end during the normal loading stage is in the opposite direction and this is an unexpected result. This may be attributed to an offset in the tip due to imprecise discretisation of the spherical surface. A contact on the facetted surface that is offset from the probe centreline will induce this type of response. Such a twisting mechanism could also be a problem in an experiment, where the colloid probe is not a perfect spherical geometry.

In addition, it can be seen clearly that the lateral bending has much less effect on the V-shaped cantilever than for the beam model. This shows that twist is the dominant response of this cantilever type, negating the need for compensation that may be needed for the optical path.

One of the main factors identified that affect response is the height of the tip (or the diameter of the sphere). For this purpose, a model with a larger colloid fixity was considered having the geometry shown in Figure 4.14(b) and the results of simulation are shown in Figure 4.20.

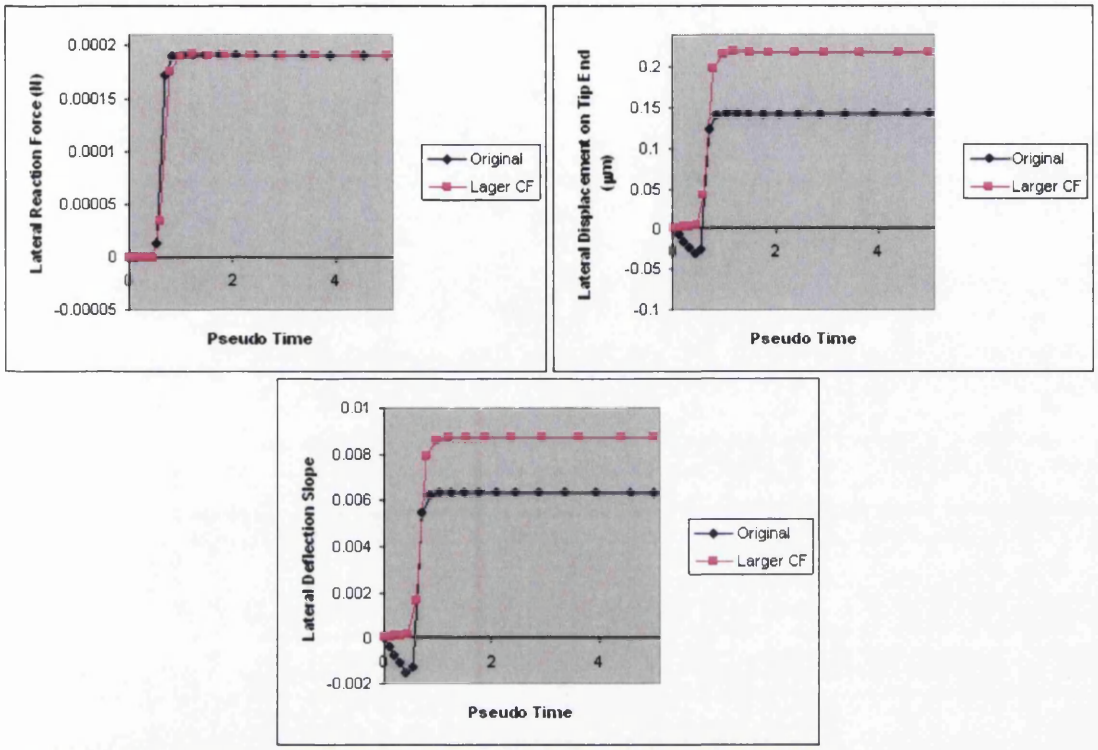

Figure 4. 20 Graphs of Reaction Force in Lateral Direction, Lateral Displacement on the Tip End, and Lateral Deflection Slope against Test Time for Original and Larger Colloid Fixity Model (V-Shaped) (Left to Right respectively)

Observing Figure 4.20, the difference that appears due to the introduction of larger colloid fixity can be seen. The final lateral force level is identical due to the equivalent mechanical engagement and contact friction coefficient choice. Also, the finite element mesh captures the tip geometry more accurately so that the contact between the tip and target surface is on the cantilever centreline and therefore load induced twist does not occur. This highlights the importance of discretisation level and also the importance of correct positioning of the particle at the cantilever tip.

The graphs of lateral displacement of the probe and the slope at the cantilever end show larger values for the greater tip height, even accounting for the offset seen from the model with original tip geometry (Figure 4.14(a)).

4.4 LATERAL SCANNING OVER SLOPING SURFACES

Practical surfaces are not smooth and dependent on the roughness wavelength and particle size there can be strong interaction when experiments are conducted in lateral scanning mode and the tip (or colloid probe) interlocks with the surface topography.

In order to capture rough surface topography, the idea of encountering a slope during shearing was explored by introducing a simple 'bump', see Figure 4.21 to represent the flank of an asperity or a groove in the surface.

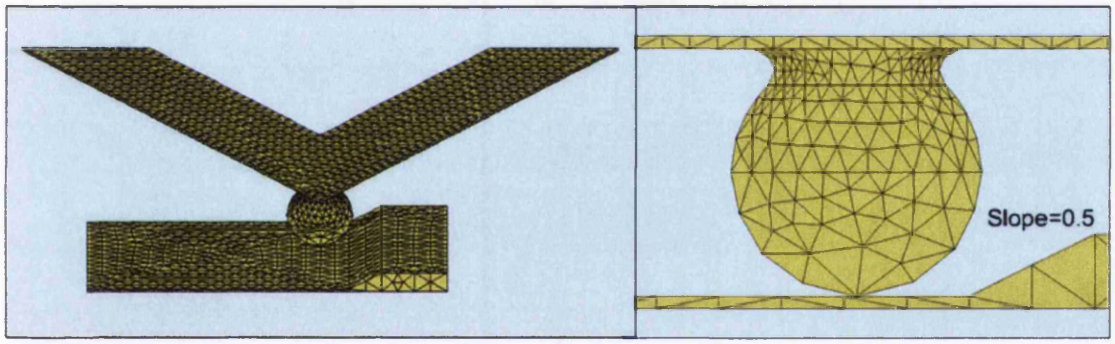

Figure 4. 21 Schematic Diagrams for Bump Model

Figure 4.21 shows the overview of the bump model, where the geometry for the cantilever was the same as for the previous V-shaped cantilever probe. The model was designed to apply a displacement on the target surface so that the probe will encounter the bump with slope of 0.5. The friction coefficient at the surface was again assigned a value of 0.1.

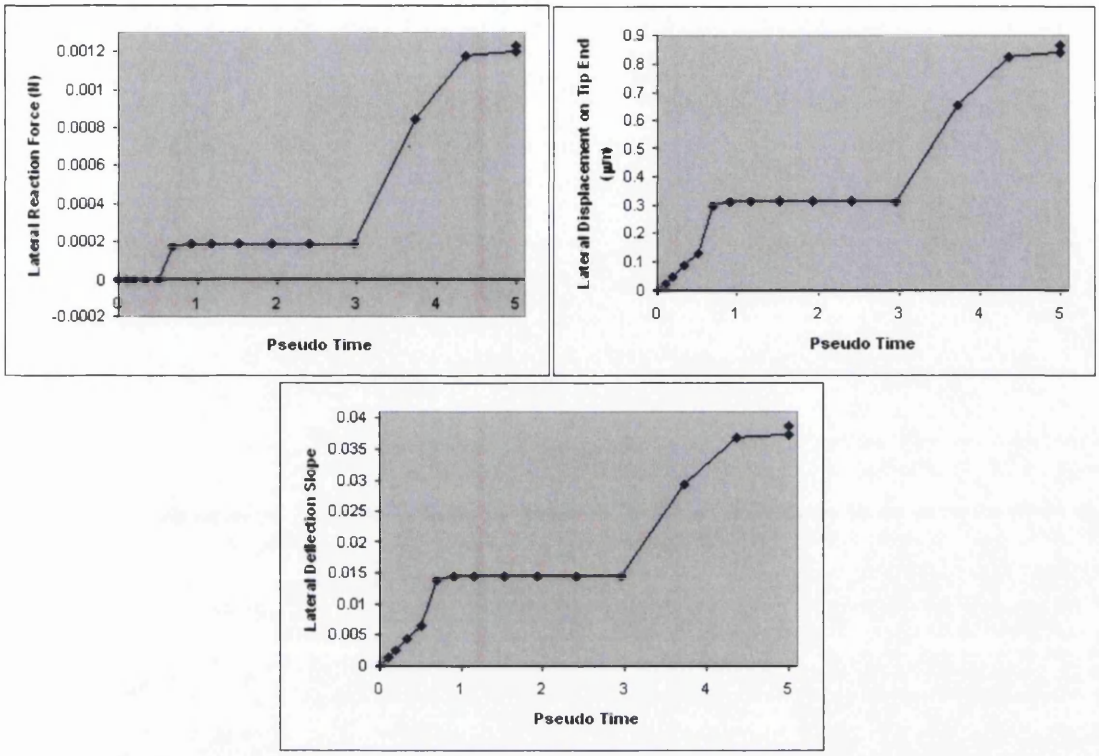

Figure 4. 22 Graphs of Reaction Force in Lateral Direction, Lateral Displacement on the Tip End, and Lateral Deflection Slope against Test Time for V-Shaped Bump Model (Left to Right respectively)

As it can be observed from the graphs in Figure 4.22, an additional step increase in all of the parameters can be seen after around test time unit of 3 as the probe tip encounters the sloped section as it traverse the surface. Even with the slope of 0.5, the increase in lateral force and deflection slope due to further normal deflection was significant. The end process of shearing did not include the probe reaching the top of the bump, however both normal and lateral forces exhibit similar increases during this sliding stage (Figure 4.23).

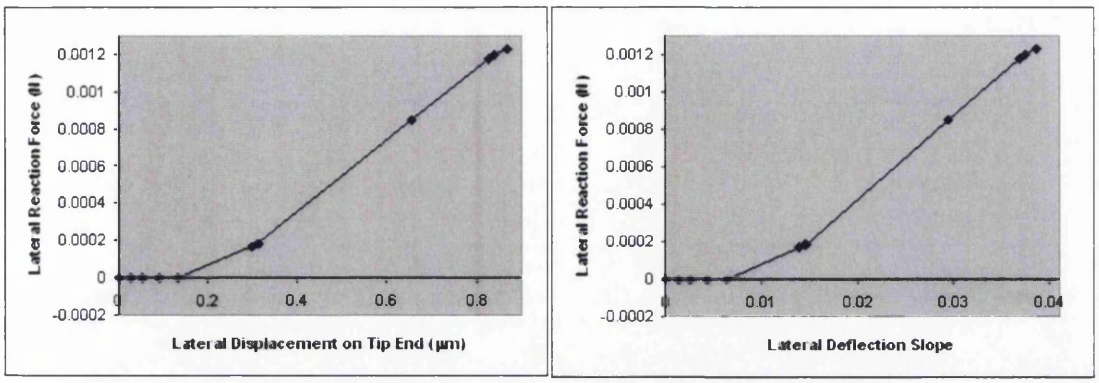

(a) (b)

Figure 4. 23 Graphs of (a) Lateral Direction Reaction Force against Displacement (Tip End) (b) Lateral Reaction Force against Deflection Slope for V-Shaped Bump Model

[Ogletree, 1996] reported experimental data for Lateral Force Microscopy (LFM) on inclined surfaces to produce friction loop as a means of calibrating its response dynamically. The experiment involved a V-shaped cantilever with pyramid shape tip scanning up and down plain inclined surfaces ($SrTiO_3$) having precise geometry achieved by annealing in oxygen leading to facets on 101 and 103 planes having angles at $+14.0^{\circ}$ and -12.5° respectively.

Emulation of this experimental work was performed with the geometries shown in Figure 4.24 below that represents a Veeco TR Series Probe [Veeco Probes Website, 2007].

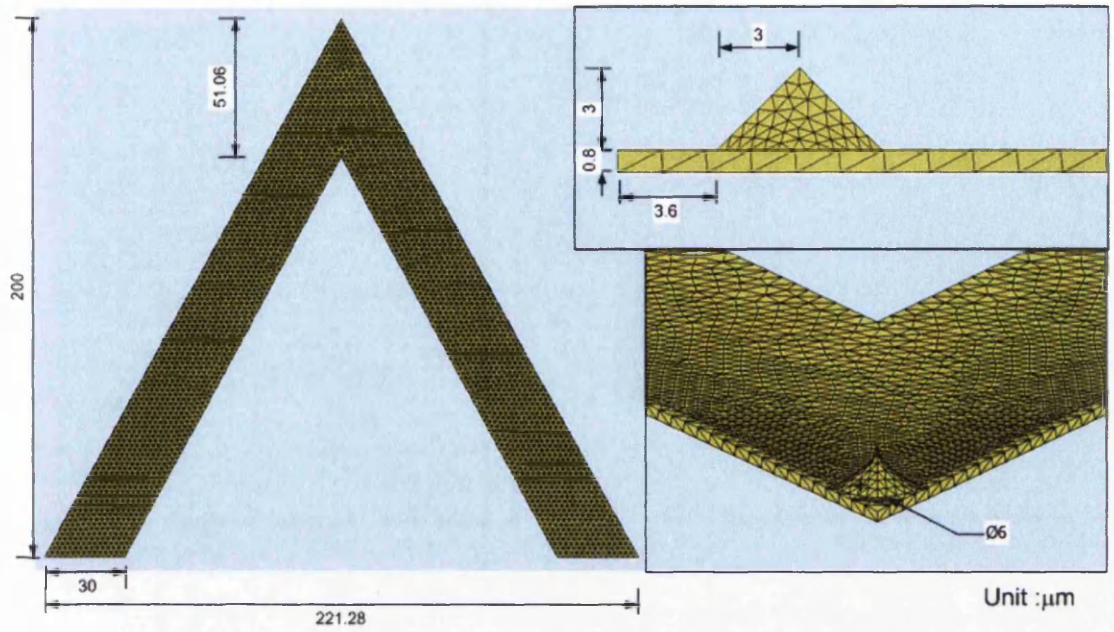

Figure 4. 24 Geometries of V-Shaped Cantilever for Emulation Model for [Ogletree, 1996] with Plastic Material Properties

The cantilever shown in above was built into a model to simulate sliding over the faceted $SrTiO_3$ surface to represent a friction loop.

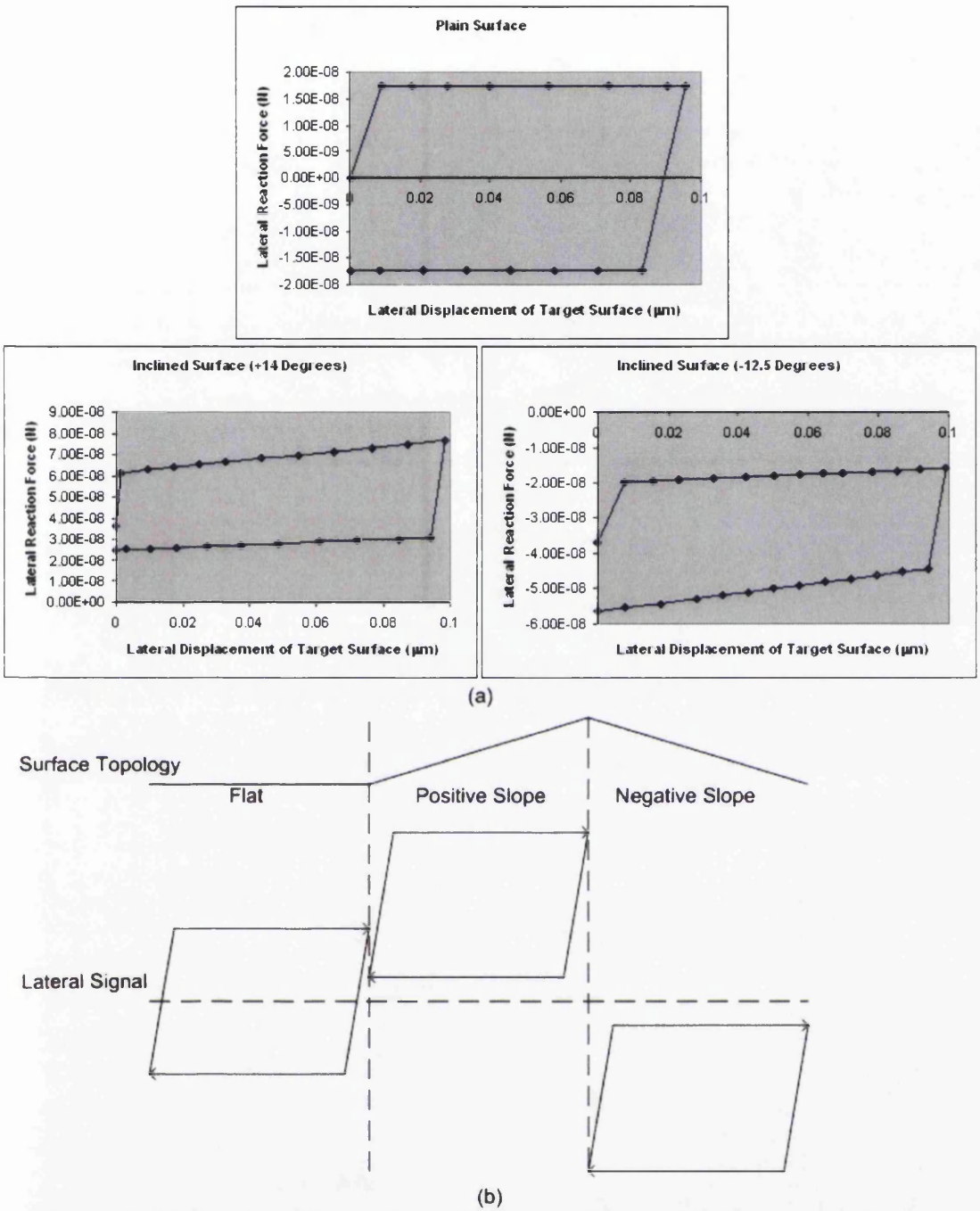

Figure 4. 25 Graphs of Lateral Displacement of Target Surface against Lateral Reaction Force for Plain (Flat), Inclined (+14 Degrees), and Inclined (-12.5 Degrees) respectively for (a) FE Model (b) [Ogletree,1996]

In general, the graphs shown in Figure 4.25 agree with the results reported in [Ogletree, 1996], and thus the friction loop was produced from which dynamic

sensitivity can be deduced. By observing the lateral force evolution for each graph, it is clearly seen that for the positive inclined surface the graph shifted up and for the negative it shifted down as expected from the experimental result. However, when climbing up and down the inclined surface, the results were not symmetrical as for the case of the plain surface, which follows the pattern shown from the experiment. This is mainly due to difference in initial geometry of the cantilever and the displacement direction.

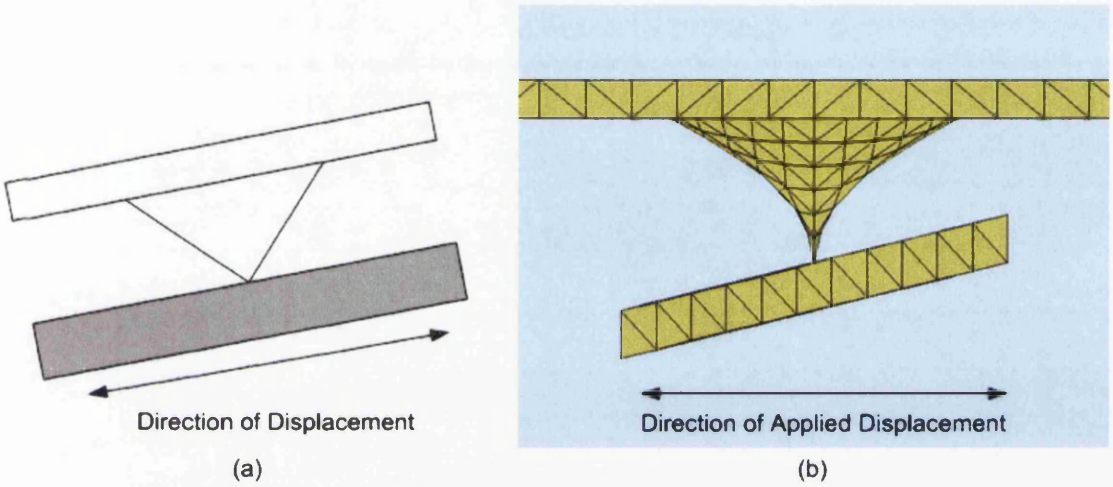

Figure 4. 26 Schematic Diagrams of Initial Geometry of (a) [Ogletree, 1996] (b) FE Model

Figure 4.26 shows the apparent difference between the two. The difference was set to reflect a more realistic environment, where in the LFM experiment, the end of the cantilever is fixed and thus the displacement should be horizontal as well as the initial cantilever geometry. In addition, it resolves the complexity caused by two directional applied displacements in modelling.

Considering the differences, the patterns shown in Figure 4.25 for both inclined surface becomes apparent and confirms the results reported in previous work. For both surfaces, the slope of increase when climbing up is greater than that of climbing down.

4.5 CLOSURE

An exploration of response in both normal and lateral direction has been investigated in this chapter.

Normal response was much more sensitive than that of lateral and hence more accurate results could be obtained. From investigation of a simple beam model, the importance of discretisation for the FE model was shown with the best result yielding in the case of near cubic elements.

The calibration by means of geometric calculation of normal and later stiffness for both simple beam [Liu, 1994] and V-shape model [Neumeister, 1994] [Noy, 1995] was compared with the results from FE model and showed good agreement especially with mathematical modelling of Neumeister (for both normal and lateral response equations).

For the lateral loading characteristics, both beam and V-shaped cantilever were affected by twisting, caused by torsion, and bending in lateral direction. However, the bending had more significant influence for the beam model (around 45 percent of the deflection), where twisting was dominating for the V-shaped model.

FE models with colloid probe tip revealed that although the material properties of the cantilever were significantly influential for both normal and lateral response, local yielding exists at the tip contact and colloid fixity. Tip height, including area of fixity and size of probe tip, was one of the factors that affect the deflection angle of the cantilever. Additionally, the importance of discretisation, probe position and shape were highlighted by twisting of the cantilever that occurs when normal load was applied.

The relationship between normal and lateral sensitivity was explored by introducing an inclined (slope=1) surface for V-shaped model, where division between them was observed and confirmed that the sensitivity in normal direction was higher than the lateral.

The overall process of lateral response for V-shaped model was explored with the inclusion of a bump and each stage was identified (i.e. first twisting, second bending, and finally slipping).

Dynamic sensitivity was also explored by emulating the previously reported experiment and the results showed good agreement in response pattern. Experimental works that have been attempted will be shown in Appendix A.2 for exploring issues of importance.

5

COMPACTION MODELLING

5.1 INTRODUCTION

Micro-mechanical modelling involves simulation at the micro scale. Fundamentally, it admits the microstructure of engineering materials is discontinuous. In the current work it represents the discrete nature of particles and is therefore a 'natural approach' to simulate particle behaviour during compaction. As set out in the review in section 2.3.2 (Figure 2.2), initial models assumed rigid particles connected by spring and dashpots. Later work included analysis of particle contact deformation while general particle deformation in which discrete and finite element schemes are combined is a recent innovation [Munjiza, 2004]. In all of these analysis types, the key requirement is to capture the interaction between particles, specifically to identify the making and breaking of interactions in a totally automated manner.

The combined application of discrete and finite element analysis is a most recent innovation. Initial work to demonstrate the technique is reported in [Ransing, 2000]. It is evident that the scheme is generally complicated and too computationally expensive to model a whole compact that comprises several million particles, typically it is capable of handling about 1,000 particles while retaining practical computing times. A more recent application of a combined discrete and finite element approach to powder compaction (denoted as a 'multi-particle finite element model') is set out in [Procopio, 2005]. In this work, the authors compare this simulation approach with other particle scale simulations of powder compaction. As well as achieving good agreement, the authors illustrate the insight gained and further benefits through application of the technique. Their work focused on round particle geometry and there remains scope for exploring the effect of different particle shapes as well as mixtures. This, including the influence of friction on compaction process will be explored further within this chapter.

5.2 THEORY

A mathematical description of the micro-mechanical modelling approach used in this work that combines discrete and finite element schemes follows. It has to account for the shape, size and mass of individual particles and how they deform in response to loads applied through particle contacts and the confinement offered by the rigid tool surfaces. A set of governing equations for a particle can be deduced from a combination of interaction law and a momentum balance principle for each particle. These equations for different particles are then coupled through inter-particle interaction, giving the global equations, which describes the behaviour of the particulate system as a whole [Munjiza, 2004].

A detailed description of the combined discrete and finite element modelling approach is set out in [Munjiza, 2004], [Mak, 2003]. An overview of the technique is presented below. The interaction between particles determines the kinematic behaviour of the assembly and it consists of normal and tangential contact force as shown below in Figure 5.1.

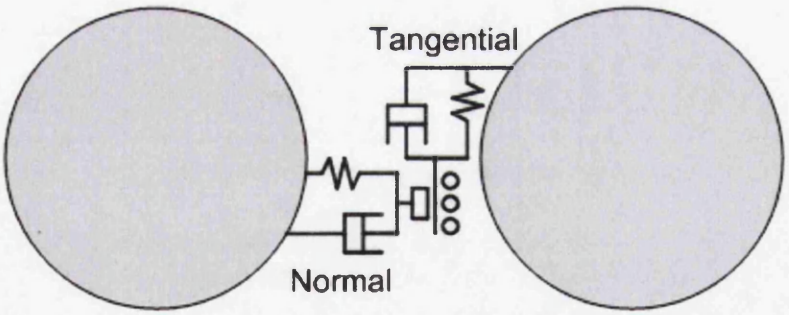

Figure 5. 1 Schematic Representation of the Interaction between Two Particles [Mak, 2003]

The interface is assigned properties to have stiffness, k, and damping, c. For both normal and tangential direction (n and l), these combined with displacement,

x, and impact velocity, v, determine the contact force, F shown in equation 5.1 and 5.2.

$$F_n = k_n x_n + c_n v_n \tag{5.1}$$

$$F_l = k_l x_l + c_l v_l \tag{5.2}$$

The normal contact force is calculated based on the interaction laws while the tangential forces are calculated from relative velocities of the contacting particles using an incremental tangential force-displacement law. The details of derivations of contact forces and contact detection are described in [Mak, 2003].

The normal and tangential forces lead to particle acceleration, such that, for example, for the normal component

$$a_t = -\frac{k_n x_t}{m} \tag{5.3}$$

For the time increments $\Delta t_t = t - t_{last}$ and $\Delta t_{next} = t_{next} - t$ integration gives

$$v_{next} = v_t + 0.5 a_t (\Delta t_t + \Delta t_{next}) \tag{5.4}$$

$$x_{next} = x_t + v_{next} \Delta t_{next} \tag{5.5}$$

where v_{next} and x_{next} are the predicted velocity and displacement at the next time step.

The discrete particle algorithm shown above has been combined with finite element tools and techniques applied at the particle level. A continuum model is applied to the particle. It is quasi static, in that the force balance excludes any effect of acceleration when computing the particle response. Within each particle, this leads to the construction of linearised equations expressed as

$$[K]\{\delta\} = \{F\} \tag{5.5}$$

where $[K]$ is the stiffness coefficient matrix

$\{\delta\}$ is the displacement vector

$\{F\}$ is the external force

The deformation, strain and stresses within each particle are computed from the displacement vector, δ. Through the presence of contact phenomena, the overall force balance on the particle assembly will not be conserved and so there will be iteration within each displacement step. Thus, the analysis continues until it reaches equilibrium within a set tolerance.

Central to the methodology, the contact between particles must be detected automatically as they occur. The detection of making and breaking of contact represents a very significant portion of computing effort within the simulation, over 60% in some cases [Munjiza, 2004].

Material models and contribution from particle interactions defined through contact algorithms are included in the stiffness coefficient matrix, $[K]$. The tools in the compaction process are considered to be rigid and loads are applied by their displacement. The deformation of each particle and the contact force at each point of constraint is then calculated for establishing the state of equilibrium. This

process continues until elastic equilibrium is established within the particle. The calculation procedure then continues depending on the type of models, i.e. elastic, perfectly plastic and plastic with hardening.

The modelling work in this chapter focuses on ductile particles and therefore a von Mises criterion was applied as one of the material properties with the assumption of plastic behaviour of the material. The model requires specification of elastic properties, the yield stress and hardening response of the material, capturing the increased resistance within each particle as deformation proceeds.

The models built in this chapter follow the generic steps of modelling as summarised in Chapter 4. In this instance, they are complicated by the need to define the position and geometry of each particle separately as well as defining the containing punch and die system. An example model build is shown in Figure 5.2. Although a two-dimensional model will not represent the three-dimensional system in full, it can give insight to the mechanisms present and explore the effects of the various factors, whereas the three-dimensional model will be computationally extremely expensive to the point that even simple three dimensional models will require several days of computing time on a high specification PC.

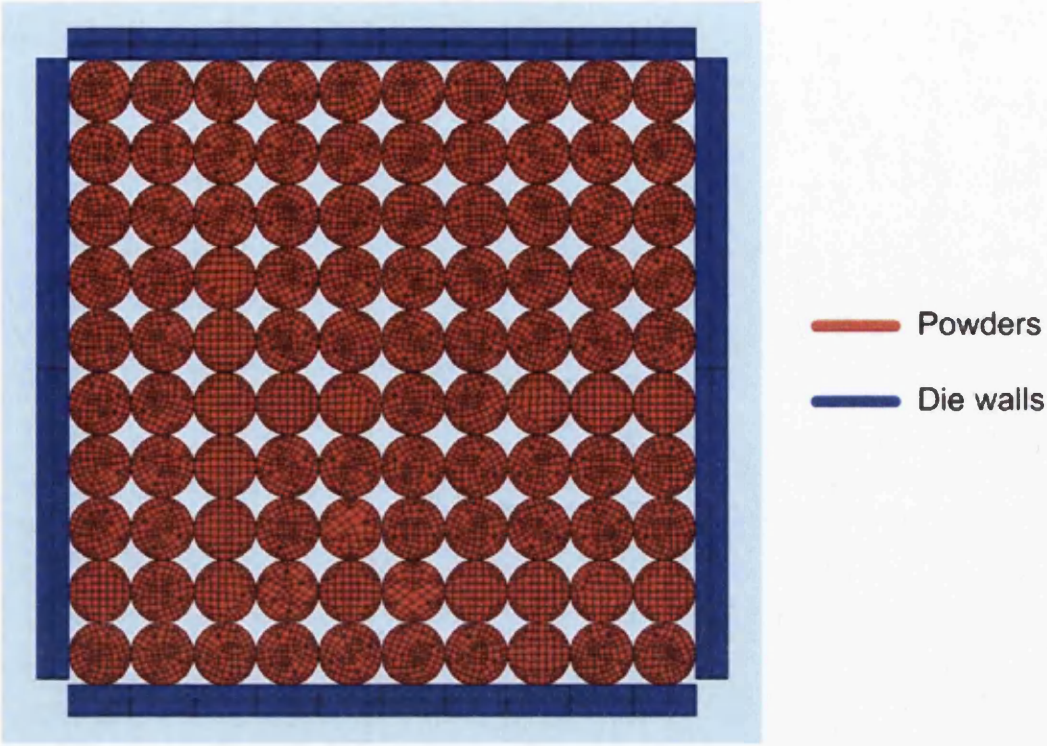

Figure 5. 2 Schematic Diagram of Element Groups in an Example Model

The mathematical description and model build strategy set out above have been embodied into a versatile simulation system ELFEN v3.0.4 from Rockfield Software [ELFEN, 2001].

Definition of initial particle packing is a crucial requirement because it determines the initial density within the compact. For example, in the case of monosized spherical particles on a regular matrix, the initial density is 0.79. A range of possibilities exists, including geometric packing of monosized particles on a regular matrix, application of geometric packing capable of handling a range of particle sizes and shapes [MacroPac, 2001] and full die filling simulations [Wu and Cocks, 2004]. Geometric packing may be based on direct input of particle geometry detail [ELFEN, 2001] or through integration of software routines [MacroPac, 2001].

In the case of complex particle geometries, modelling directly from the software is heavily time consuming. For this purpose, geometric packing based on integration of software routines was adopted. A particle packing software called MacroPac [MacroPac, 2001] was utilised and the resulting geometries were then imported to ELFEN. MacroPac enables random particle packing with various shape and size, most commonly for circular and rectangular shaped particles. For the rectangular particles, sharp corners cause stress singularity and therefore a separate process involving rounding was introduced before the import phase. Rounding was selected such that the radius was 40% of the minimum particle side. Although this will tend to lose the original rectangular particle geometry, it was necessary in order to avoid time consuming computation. The rounded particles will therefore be called 'semi-rectangular'.

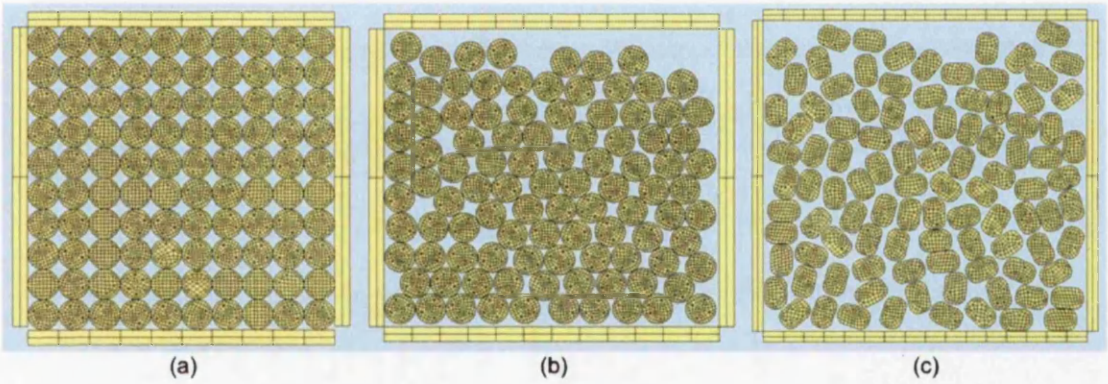

Figure 5. 3 Schematic Diagrams of Initial Packing of Models (a) Monosized Spherical Particles in Regular Matrix (b) Random Geometry Packing (c) Rounded Rectangular Particles with Random Packing

Figure 5.3 shows a compaction model comprising monosized particles with different initial packing geometry. Additional models comprising a mixture of different size and shape particles were also prepared as shown in Figure 5.4. The compact size of the models was not identical for the three cases in Figure 5.3 due to random packing and different shape and size for (c). For (a) and (b) the particles were 10mm in diameter and 1.5:1.0 ratio (15mm/10mm) with rounding (semi-

rectangular) mentioned above for (c). Although these dimensions are large in comparison with the real particles, they were enforced by computational constraints.

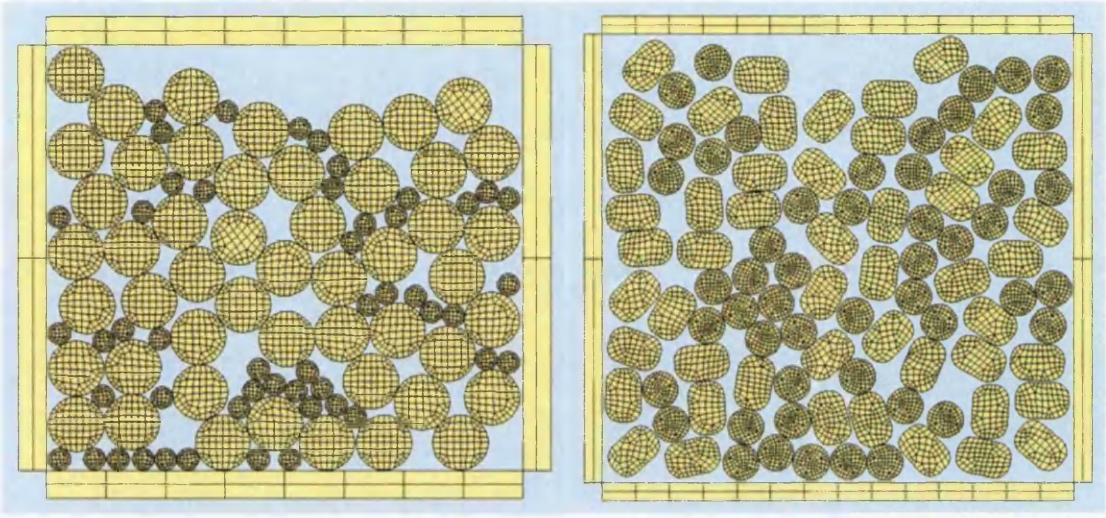

Figure 5. 4 Schematic Diagrams of Initial Packing of Models (a) Random Packing of Spherical Particles with Different Sizes (b) Random Packing of Particles with Different Shape

There are a range of outputs from the simulation that include for example, particle displacement and deformation, stresses, tool forces, etc. For powder processing, compact density is a crucially important output and this is not readily available from the simulation. Where particles use identical material, relative density may be derived directly from geometric data, through the ratio of total particle shape divided by overlaid footprint area. By selecting a footprint of appropriate area and moving this over the compact, it is possible to have a rough estimate of the local density variation throughout the compact. Thus, relative density was acquired by using an image analysis tool. To do so, an image was screen captured from the simulation program at a certain stage and edited manually to remove the unnecessary parts, such as tooling, where this was then processed. In order to determine the accuracy of this method, the total compact area was divided

in to 25 identical sections to derive a relative density contour of the system (Figure 5.5).

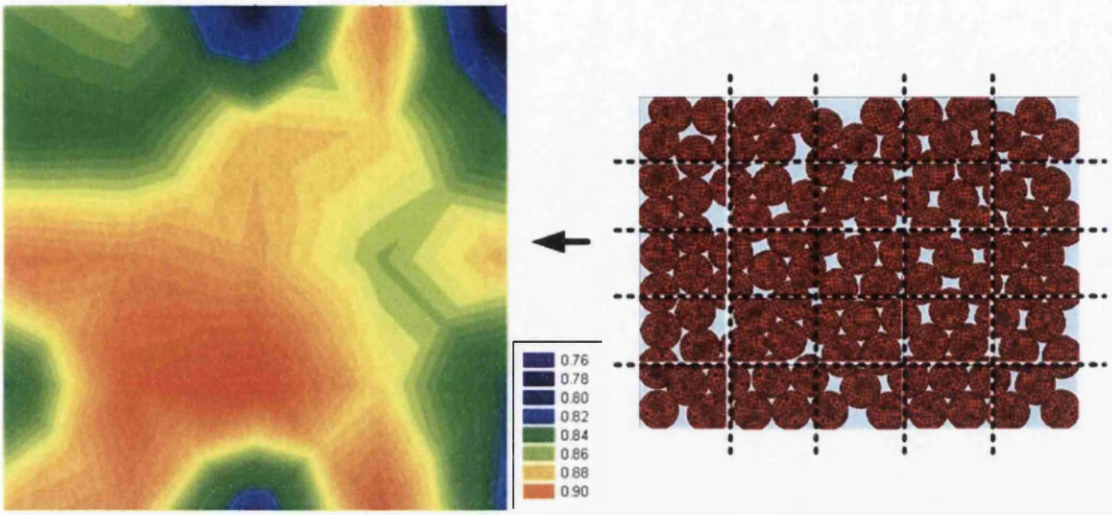

Figure 5. 5 Contour of Relative Density

From Figure 5.5, it can be seen that the estimate of local density variation throughout the compact by this method reflects the geometric packing arrangement.

The modelling approach described above will be used to explore compaction and contact behaviour in the powder compaction process and this work will be described in the following sections.

5.3 COMPACTION MODELS

Particle scale compactions models have been developed to explore the impact of particle topography and friction on compaction response.

For the material properties, the model was divided into tools (punch, die walls, target surface) and particles as itemised in Table 5.1.

Part	Material	Young's Modulus (Nmm^{-2})	Poisson's Ratio	Yield Stress (Nmm^{-2})	Hardening Modulus (Nmm^{-2})
Tools	Steel	(Rigid)	(Rigid)		
Particles	316L	2.0×10^5	0.3	240	440
	OFHC Cu	1.15×10^5	0.35	50	440

Table 5. 1 Material Properties of Parts in Compaction Modelling

The tooling in the model was considered to be rigid and the two types of particle represent soft and hard ductile materials. These particles were also chosen because their material properties are well known and documented [Gethin, 2001] [Ransing, 2004] [ASM Metals Handbook, 1986]. Additionally, since both particles were ductile, same hardening modulus (a linear approximation of the work hardening rate) was used.

A number of case studies were devised for simulation. Some were directed at exploring simulation issues and others were aimed at exploring the effects of process parameters on the compaction process. The case studies undertaken are itemised in Table 5.2 below.

Exploration of simulation issues involves particle count, time step, and particle discretisation effects. It is well known that for increased particle count and mesh refinement, the simulations become computationally more expensive. Typically, the work described in [Procopio, 2005] suggests several days of computation for an assembly comprising about 1600 particles. Exploration of

process parameter effects using computation requiring this duration is not practical and therefore numerical studies were undertaken to explore the use of fewer particles combined with mesh refinement within each particle.

The remaining factors were chosen to explore the effects of process parameters on the compaction process. Principally this includes friction, material yield and particle size/geometry effects.

Friction coefficient parameter study was necessary to investigate the effect of friction coefficient between the tool surfaces and the particles.

Initial packing geometry can also be crucial since it defines the variation of initial density within the compact. Particles with different size and shape were introduced to explore the effects of interactions between particles and variation in relative density of the compact. For all the case studies, plastic material response with hardening, with properties shown in Table 5.1, was used except for the comparison section below (Figure 5.14) where an elastic - perfectly plastic yield model was adopted.

Factor Studied		**Cases Studied**
Simulation Issues	Particle count effects	25, 49, 100 Particles
	Time step effects	Different time increment
	Particle discretisation effects	Particle mesh size (1.25, 1, 0.75)
Process Parameters	Friction coefficient parameter	Friction coefficient between die wall and particles (μ_1), Friction coefficient between particles (μ_2) = 0.001, 0.1, 0.3
		$\mu_1 = 0.1$ $\mu_2 = 0.1, 0.5$
		$\mu_1 = 0.1, 0.5$ $\mu_2 = 0.1$
	Initial packing geometry	Two randomly packed geometries
	Particle size	100 large particles, 100 small particles, 50-50 mixed (spherical)
	Particle shape	100 spherical particles, 100 semi-rectangular particles, 50-50 mixed

Table 5. 2 Case Studies for Compaction Modelling

5.4 SIMULATION FACTORS

5.4.1 Particle Count Effects

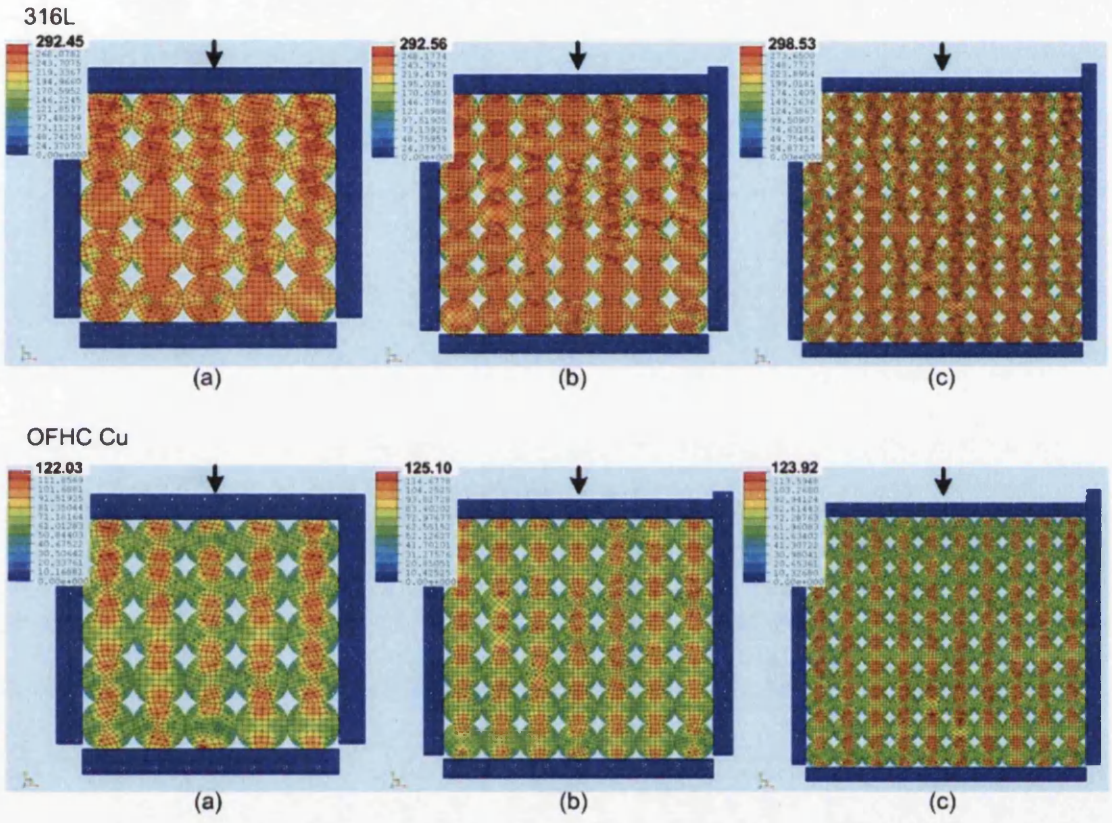

Figure 5. 6 Schematic Diagrams of Effective Stress for (a) 25 (b) 49 (c) 100 Particles (10mm Diameter)

Simulations were undertaken in which compaction was facilitated by downward movement of the top punch. In this part of the work, compaction was achieved by downward motion through a distance of 10% of the die length with the same termination time and the friction between the powder and die was assigned a coefficient value of 0.1. These models consist of monosized spherical particles in a

regular matrix thus assigning an initial density of $\frac{\pi}{4} = 0.79$ as shown in Figure 5.3(a).

Figure 5.6 shows the effective stress contours within each particle at notionally identical top punch displacement. Clearly, the stress values are similar for different number of particles and in comparing hard and soft materials, the difference is apparent. Although the stress levels are similar in three cases, Figure 5.6 only shows the end-result, and therefore further exploration of the process should be investigated by observing force curves in order to study particle count effects.

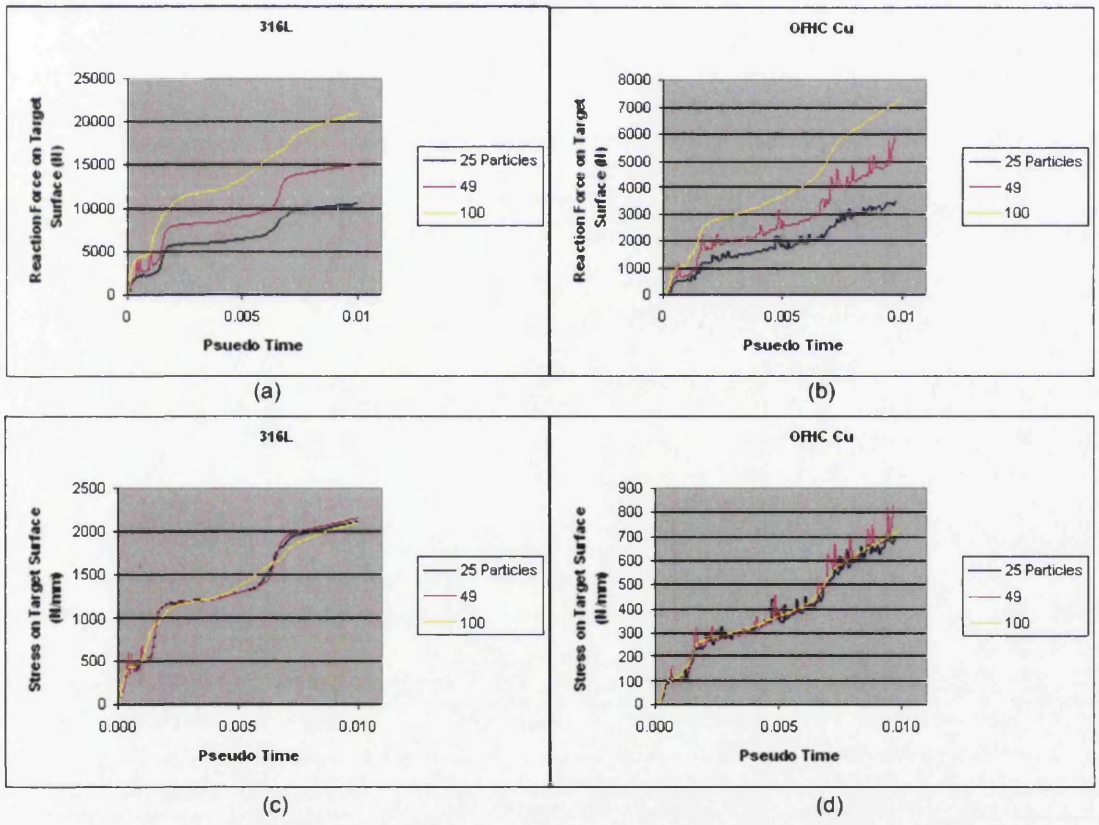

Figure 5. 7 Graphs of Particle Count Effects with Force against Time for (a) 316L (b) OFHC Cu and Stress against Time for (c) 316L (d) OFHC Cu

Figure 5.7 shows the evolution of force on the bottom punch as compaction proceeds. This also includes particle count effects for both hard and soft materials.

The compaction force displays distinct characteristics in that for the hard particles it builds up in an approximately step wise manner. The reason for will be explored below. These results were also expressed as an average load on the bottom punch since the dimension of the die varied for each case (Figure 5.7(c) and (d)). Since the model was two-dimensional, the force was divided by the length of the bottom punch. It can be seen that the general pattern was similar for different particle counts. The results for the softer material display a more noisy response, particularly for the cases comprising 25 and 49 particles.

Overall, it can be seen that a model with higher number of particles produced the smoother increase in force and thus resulting in a clearer representation of the compaction process. This was especially apparent in the case of softer material. From this investigation, models with 100 particles were chosen as a reference.

5.4.2 Time Step Effects

Time step effects were explored by varying time increment (Δt) with set termination time of the simulation process. For identical punch displacement and termination time, the number of divisions is increased. The critical time step value depends on material and discretisation issues. Based on an elastic approximation, the critical time step is given by:

$$\text{Time Step Increment } \Delta t = \frac{l}{c} \text{ and } c \approx \sqrt{\frac{E}{\rho}} \tag{5.6}$$

where l is the edge length

E is Young's modulus

ρ is density

Thus time step is governed by material properties (Young's modulus and density) together with discretisation in terms of the minimum element edge length 'l'. In the context of the current simulation, selection of material and discretisation parameters leads to very small time steps, typically $0.3 \sim 0.4 \times 10^{-7}$ s.

Simulations were undertaken using a model comprising 100 particles with friction between the powder and tool surfaces being captured through a coefficient value of 0.1. The results from the simulations are shown in the form of effective stress contours in Figure 5.8 and little difference between different time increments choice was observed.

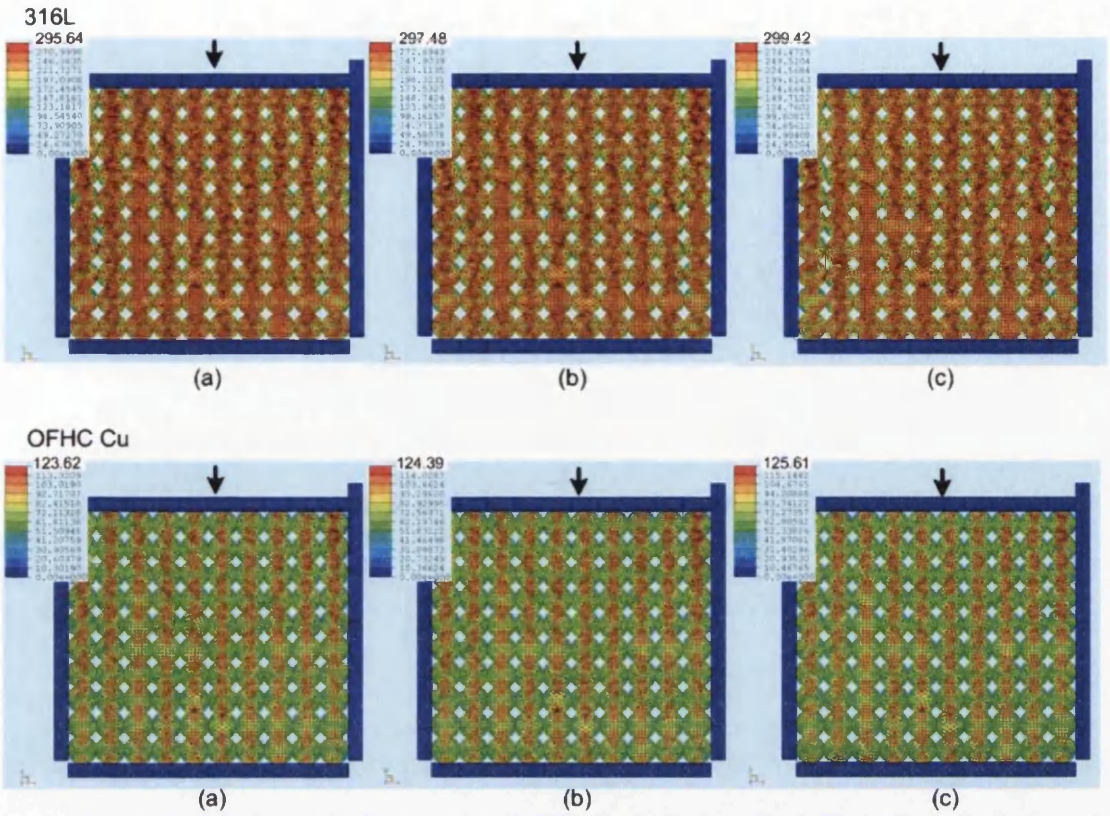

Figure 5. 8 Schematic Diagrams of Effective Stress where Time Increment is

(a) > (b) > (c)

The time increment and critical value range for these different cases are presented in Table 5.3. This confirms that the size of the time step has an impact on the overall calculation duration (i.e. the smaller the time step, the longer the duration).

Cases	Number of Divisions	Δt Range	Critical Value Range	Overall Duration
316L	94000	$0.48 \sim 0.69 \times 10^{-7}$	$0.53 \sim 0.66 \times 10^{-7}$	1 hour
	163000	$0.12 \sim 0.68 \times 10^{-7}$	$0.57 \sim 0.76 \times 10^{-7}$	3~4 hours
	196000	$0.07 \sim 0.68 \times 10^{-7}$	$0.53 \sim 0.76 \times 10^{-7}$	4~5 hours
OFHC Cu	68000	$0.70 \sim 0.83 \times 10^{-7}$	$0.78 \sim 0.92 \times 10^{-7}$	30 mins~1 hour
	106000	$0.27 \sim 0.82 \times 10^{-7}$	$0.80 \sim 0.92 \times 10^{-7}$	2~3 hours
	140000	$0.13 \sim 0.82 \times 10^{-7}$	$0.79 \sim 0.92 \times 10^{-7}$	3~4 hours

Table 5. 3 Cases Studies for Time Step Variation

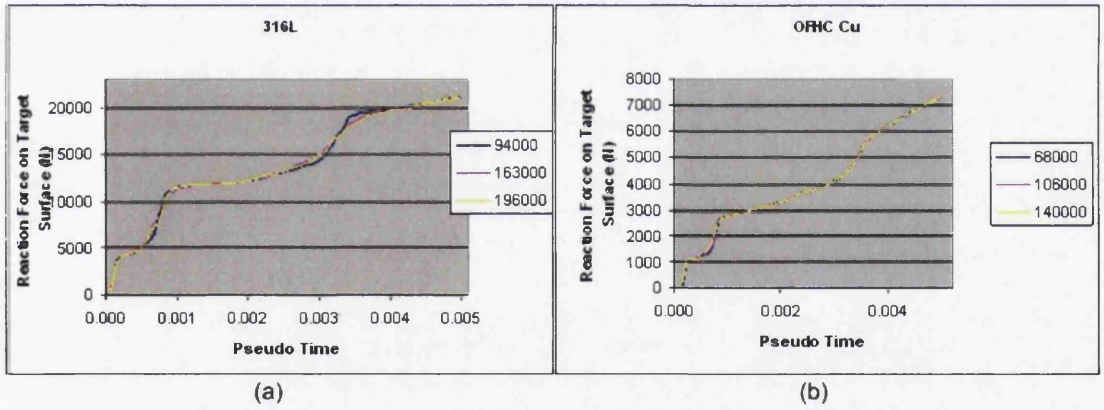

(a) (b)

Figure 5. 9 Graphs of Time Step Effects with (a) 316L (b) OFHC Cu for Different Number of Divisions

Although it can be observed from Figure 5.9 that generally the increase in number of time steps had little influence on the force value, the effect of a larger number of divisions can be seen. For the harder material, a smoother increase in force was observed. The difference in pattern for the softer material was even less.

This has been attributed to the contact and rearrangement process, which is more evident for the harder particles, the softer particles deform plastically.

5.4.3 Particle Discretisation Effects

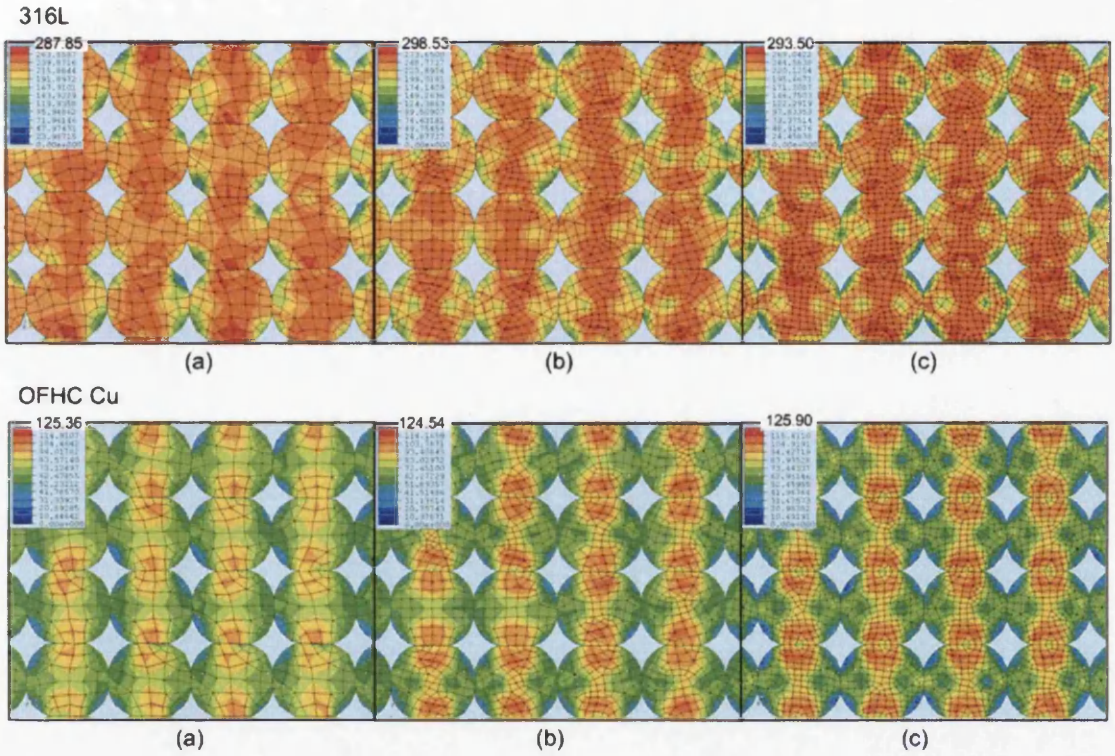

Figure 5. 10 Schematic Diagrams of Effective Stress with Particle Discretisation

(a) Coarse (b) Moderate (c) Fine

From examining Figure 5.10, the stress levels are not significantly different. Differences that do exist may arise from slight discrepancies in time at which the contours have been plotted, a consequence of data output control from the software. Each particle within the assembly was discretised identically.

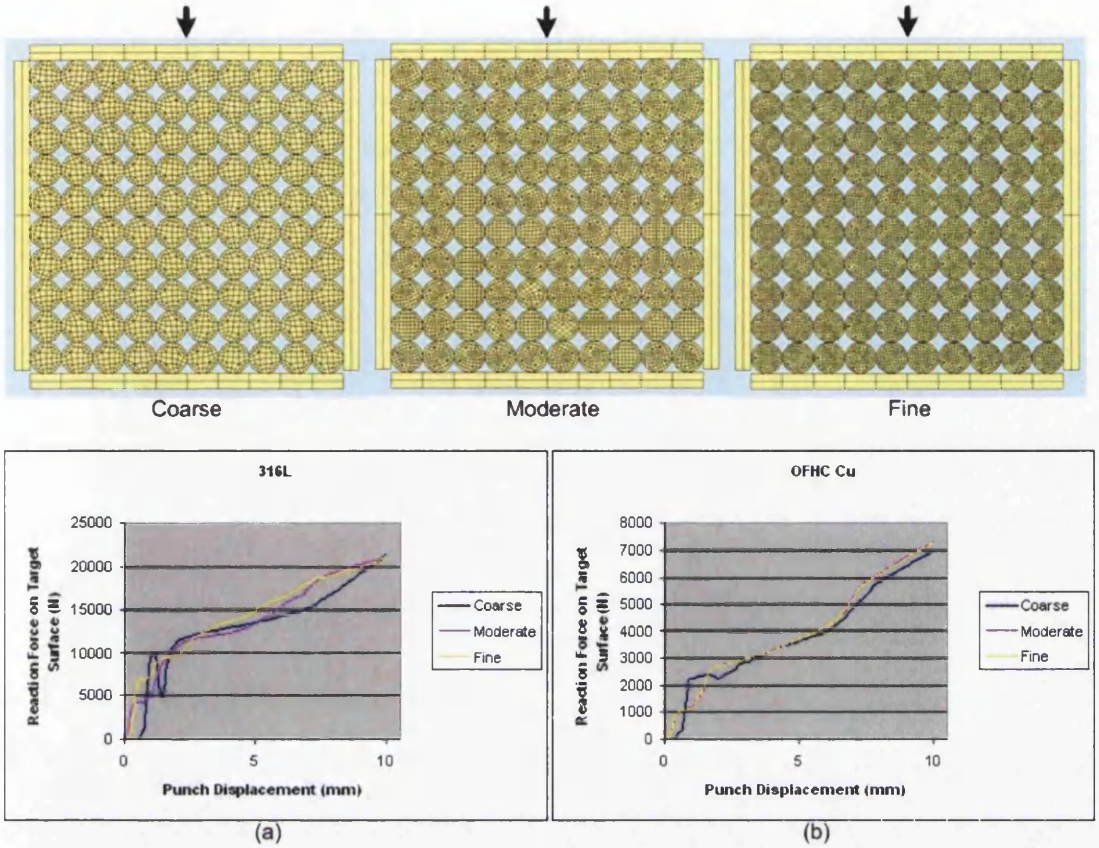

Figure 5. 11 Graphs of Particle Discretisation Effects with (a) 316L (b) OFHC Cu

Figure 5.11 shows the consequent tool force evolution for which notable differences may be observed for the harder material. The force fluctuation observed for these particles diminished as the discretisation became more fine.

From the effects investigated above, it is clearly seen that a model with large number of particles and time steps with fine discretisation produces better results. However, it is more time consuming to compute and so a moderate discretisation setting was chosen.

From the three investigations of simulation issues, the reaction force showed a similar response pattern, increasing as an approximate step function shape. In

comparing with macro scale experiments, this is not an expected result and so in order to explore this response further, a thorough investigation of the mechanism was undertaken (Figure 5.12, 5.13 below).

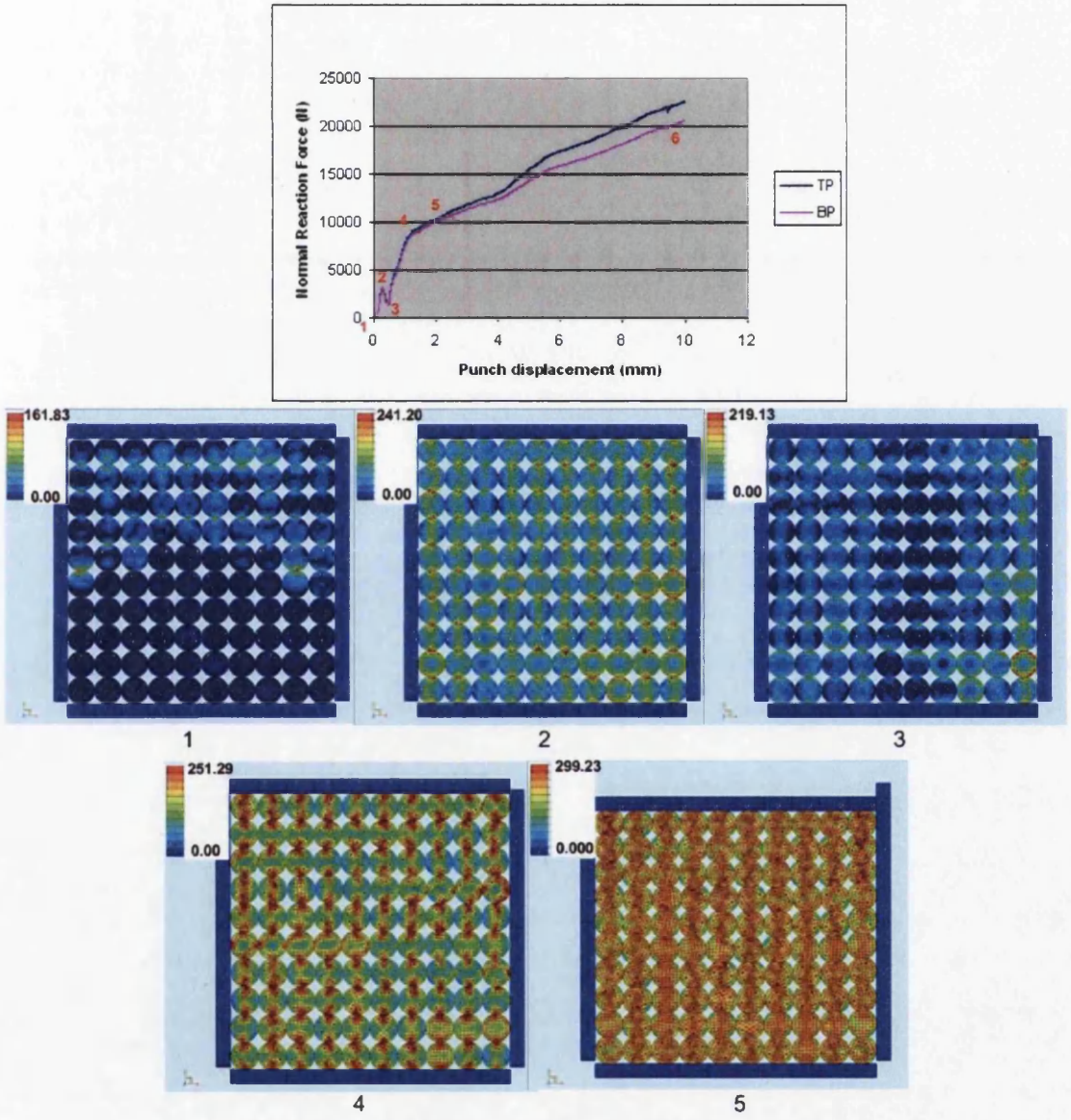

Figure 5. 12 Investigation of Compaction Process by Effective Stress Diagram

Figure 5.12 shows the compaction process for a hard ductile powder in a rigid tool set with a coefficient of friction of 0.1 throughout the system.

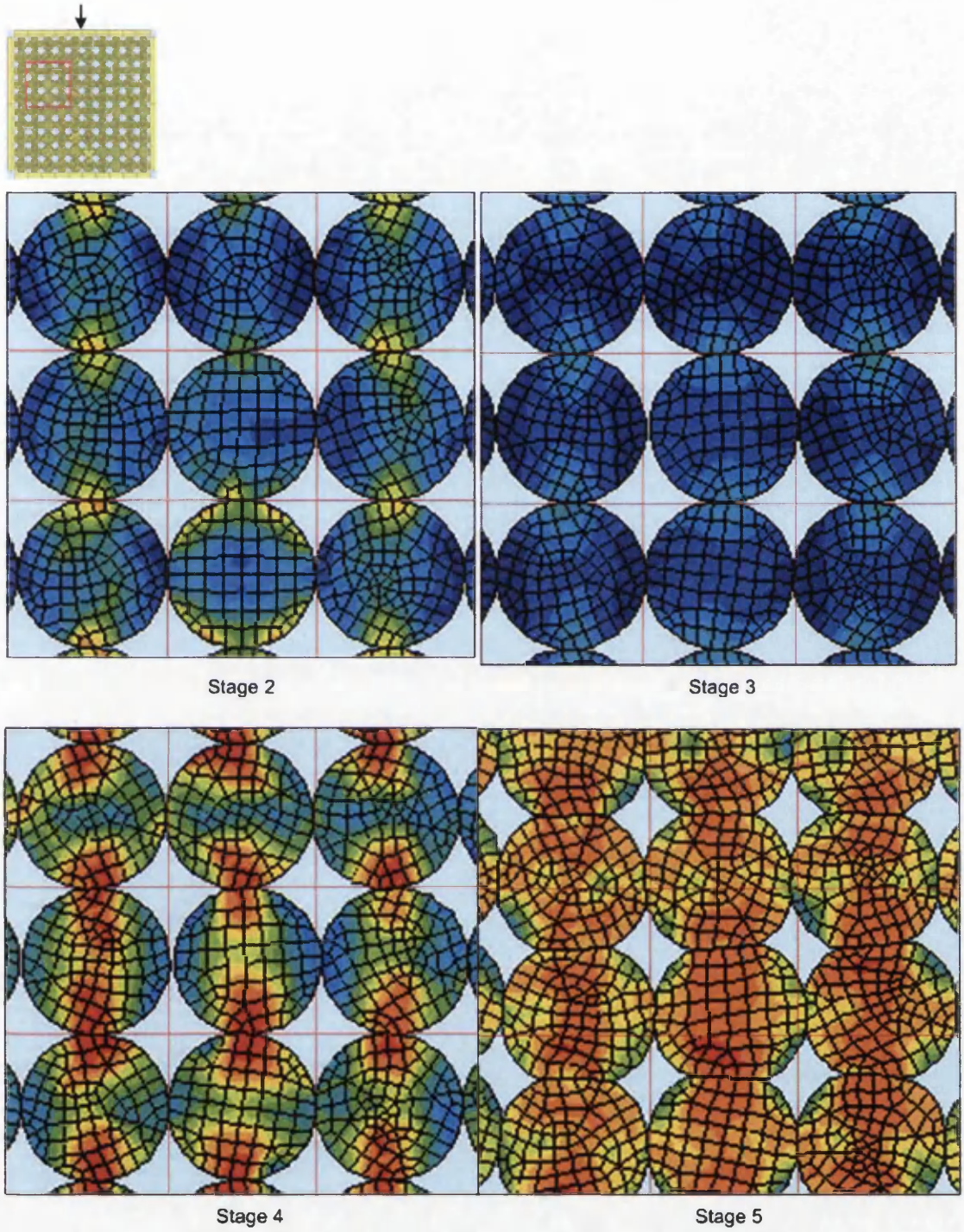

Figure 5. 13 Specific Investigation of Compaction Process

The mechanism present in this process may be mainly explained by a rearrangement of particles. Figure 5.13 describes a close up view of the particles

for the stages shown in Figure 5.12. The reaction force on top (TP) and bottom (BP) punch increases sharply in stage 1. However, once it reaches stage 2, the force (stress) value drops which are due to rearrangement and slipping of particles. This can be observed from stage 3 in Figure 5.13. Once the particles are settled to a new position, the force value starts to rise sharply again until stage 4. From then on, deformations of particles occur, also with slight rearrangement up to stage 5. This explains the gradual increase in force after stage 4. This process repeats with less impact due to more deformation until stage 6. As a check, the figure also demonstrates a consistent difference between top and bottom punch forces, arising from friction between the particles and die wall. The form of the difference exhibited is identical to that measured during the compaction of powder by downward movement of the top punch, the top punch force exceeds the reaction of the bottom punch.

The slipping could also be influenced by discretisation in the handling of contact between particles. Three scenarios exist corner-corner, corner-edge and edge-edge. Corner to corner and corner to edge contacts are particularly problematic. What happens at these contacts can have an influence on the outcome, particularly for a smaller discretisation count, where elements are therefore larger. To investigate this fully requires very precise control over mesh generation within the particles, even the smallest asymmetries in the mesh can lead to imbalance in the numerical sense and so generation of a 'perfect mesh' is not practical. For this reason, this was not pursued further at this point.

Prior to exploring the effects of process parameters on the compaction process, a model was constructed to emulate the documented work of [Procopio, 2005] [Redanz, 2001]. The loading was applied on both top and bottom punch with same amount of displacement and the coefficient of friction on the system was set at 0.001 (practically frictionless). In order to compare results in terms of relative density of the system, the method introduced in Figure 5.5 was used but with a difference of computing average density of the whole compact.

The difference in models are itemised in Table 5.4 below.

Models	Number of Particles	Nodes / Elements per Particle	Initial Relative Density	Initial Packing Geometry
[Redanz, 2001] (DEM)	1683 particles	1 / 1.95	0.823	Randomly packed
[Procopio, 2005] (Multi-Particle FEM)	At least 800 particles	169 / 132	0.803	Random
Compaction Modelling (DEM-ELFEN)	100 particles	162 / 141	0.798-0.8	Regular matrix

Table 5. 4 Parameters of Models in Comparison

The main difficulty in emulating the model was attempting to assimilate different initial relative density, defined by the ratio of the total cross-sectional area of the cylinders (particles) to that of the die. The value was 0.823 for [Redanz, 2001], where ballistic deposition method was used by dropping particles one by one from a random starting position into the die. The initial density for [Procopio, 2005] was 0.803 and it is reported that this increased value was due to exclusion of an external layer of two particle diameters along the outer surface of the particle assembly.

In the graphs shown below, stress ratio (Axial Stress / Yield Stress) was chosen as the variable to eliminate effect of material properties and cross section of the die. As mentioned before, the model was two-dimensional and therefore the force (F_y) was divided by the length of the punch (L) for the axial stress and

material properties of 316L from Table 5.1 was used with critical Δt of $0.57 \sim 0.76 \times 10^{-7}$. Both coefficients of friction were set as reported in [Procopio, 2005] ($\mu_1 = 0$, and $\mu_2 = 0.5$).

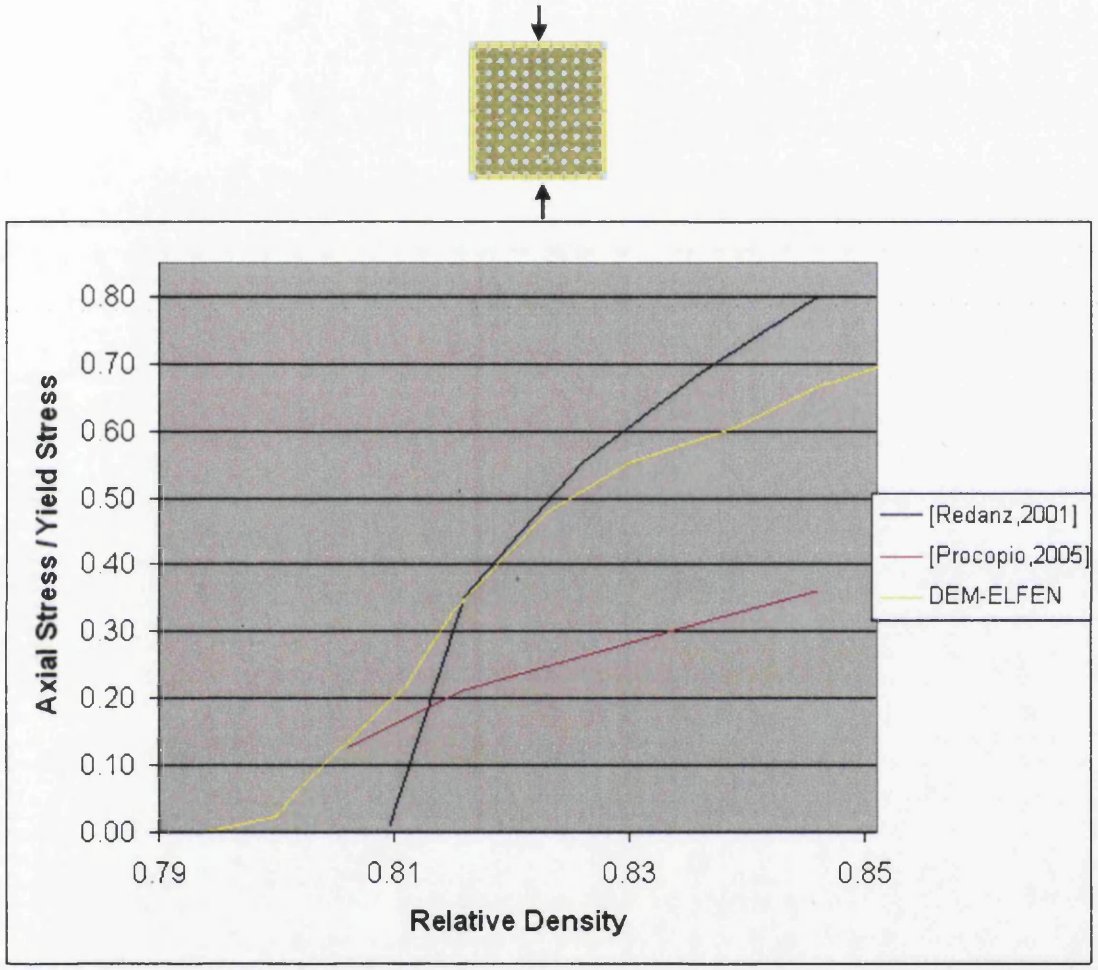

Figure 5. 14 Graphs of Relative Density against Stress Ratio for Models in Comparison

As explained above, the initial density values with previous models were higher and attempts were made to minimise the offset for making a more accurate comparison, by using MacroPac [MacroPac, 2001]. The process of particle generation and then the die shaken to settle was repeated in this packing method.

This meant all particles were whole and monosized with not all particles in contact with the tooling. Therefore, the largest initial density could be achieved by a regular matrix, 0.798-0.8. Despite of the offset issue, the behaviour of the DEM-ELFEN displays a good agreement with other models.

5.5 PROCESS PARAMETER EFFECTS

5.5.1 Friction Coefficient Parameter

Friction parameter effects were explored using a matrix comprising 100 particle that has been demonstrated to be adequate in the exploration of numerical simulation issues. These particles were identical and circular in geometry. In this section, the friction coefficient between the die wall and particles (μ_1) and the friction coefficient between the particles (μ_2) was considered.

Both friction coefficients (μ_1, μ_2) were set as having the same value and its effect was explored.

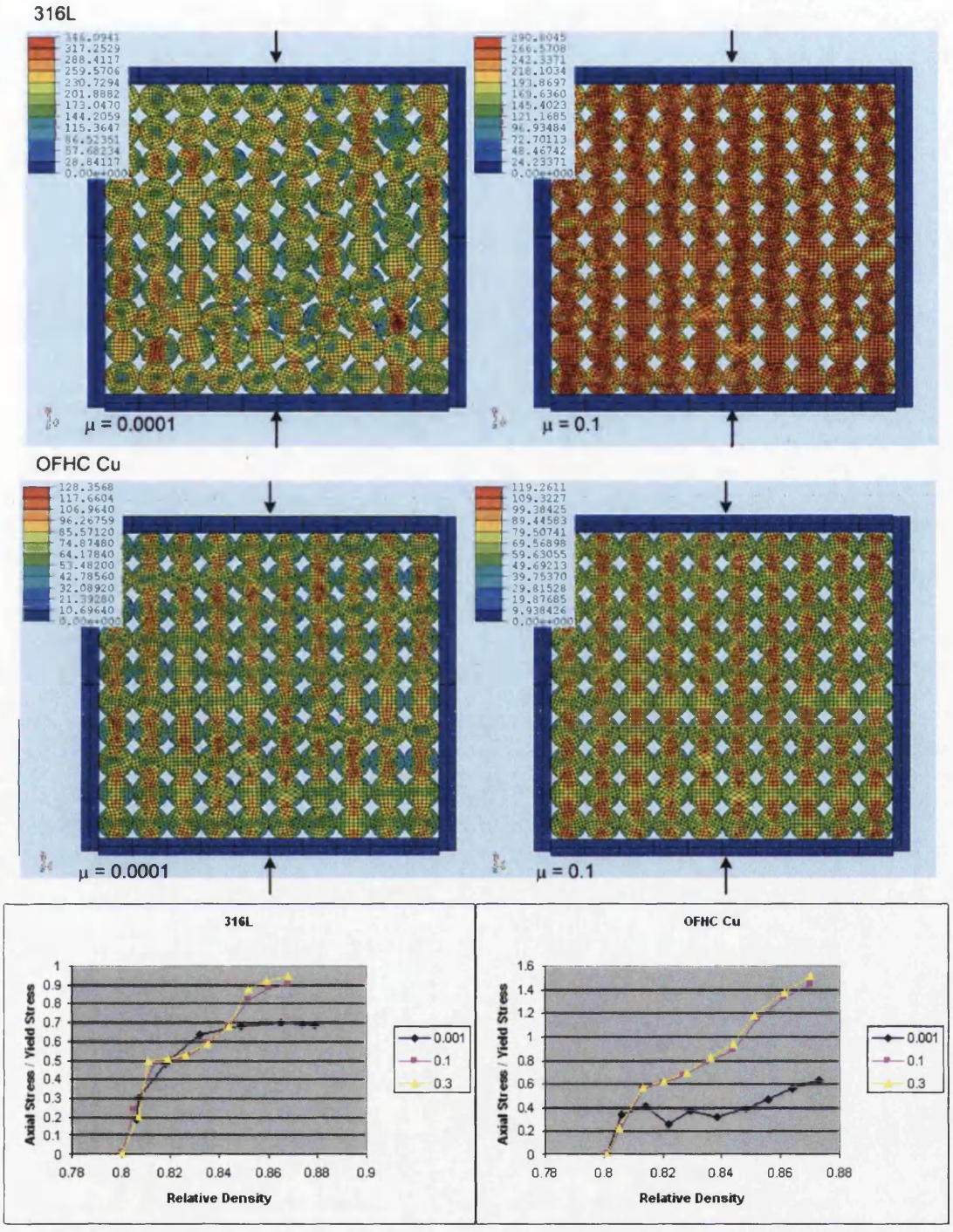

Figure 5. 15 Schematic Diagrams of Effective Stress for Two Materials with $\mu = 0.0001, 0.1$ *and Graphs of Relative Density against Stress Ratio with Variation of Global Friction Coefficient*

The contours presented in Figure 5.15 are all towards the end of the simulation where it is near enough to be considered the same stage. For both materials, although stress levels for the frictionless model seem to be higher than in the case with friction coefficient of 0.1, it is the range of stress level that is wider and not the actual stress levels, which is evident by its distribution. This is due to frictionless model allowing significant amount of particle movement, especially for harder ductile material, resulting in more deformation of certain particles.

Graphs in Figure 5.15 show that as the global friction coefficient increases the ratio between axial and yield stress increased. Frictionless state led to smooth increase in stress levels. Although much more rearrangement of particles was observed, it had very little impact on the stress, since the particle can slide more freely over each other. However, movement of particles becomes more influential with the introduction of friction between die wall and particles and inter-particles. Slight rearrangement was enough to affect the behaviour of stress in this case around 0.81 of relative density. Significant difference was observed between frictionless ($\mu_1, \mu_2 = 0.001$) and moderate friction ($\mu_1, \mu_2 = 0.1$) than between moderate and high friction ($\mu_1, \mu_2 = 0.3$). At this stage, this confirms the importance of friction. It will be explored further using force-displacement curves in the following sections.

In order to investigate the effect of wall and inter-particle friction in a systematic manner, different local friction coefficients (μ_1, μ_2) can be assigned and these were adjusted systematically in order to explore the relative importance of die wall and inter-particle friction.

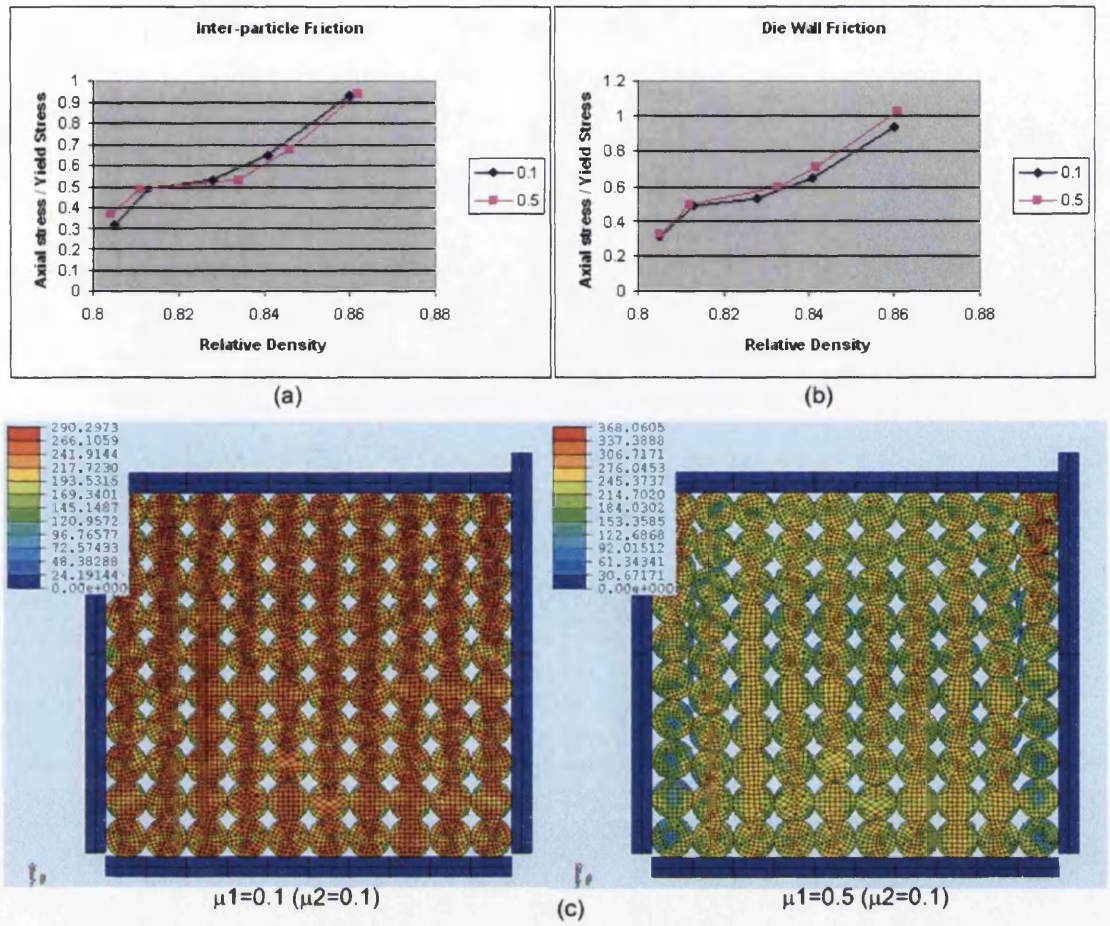

Figure 5. 16 Graphs of Relative Density against Stress Ratio (316L) with the Variation of (a) Inter-Particle Friction Coefficient (μ_2) (b) Die Wall Friction Coefficient (μ_1) and (c) Schematic Diagrams of Effective Stress (for μ_1)

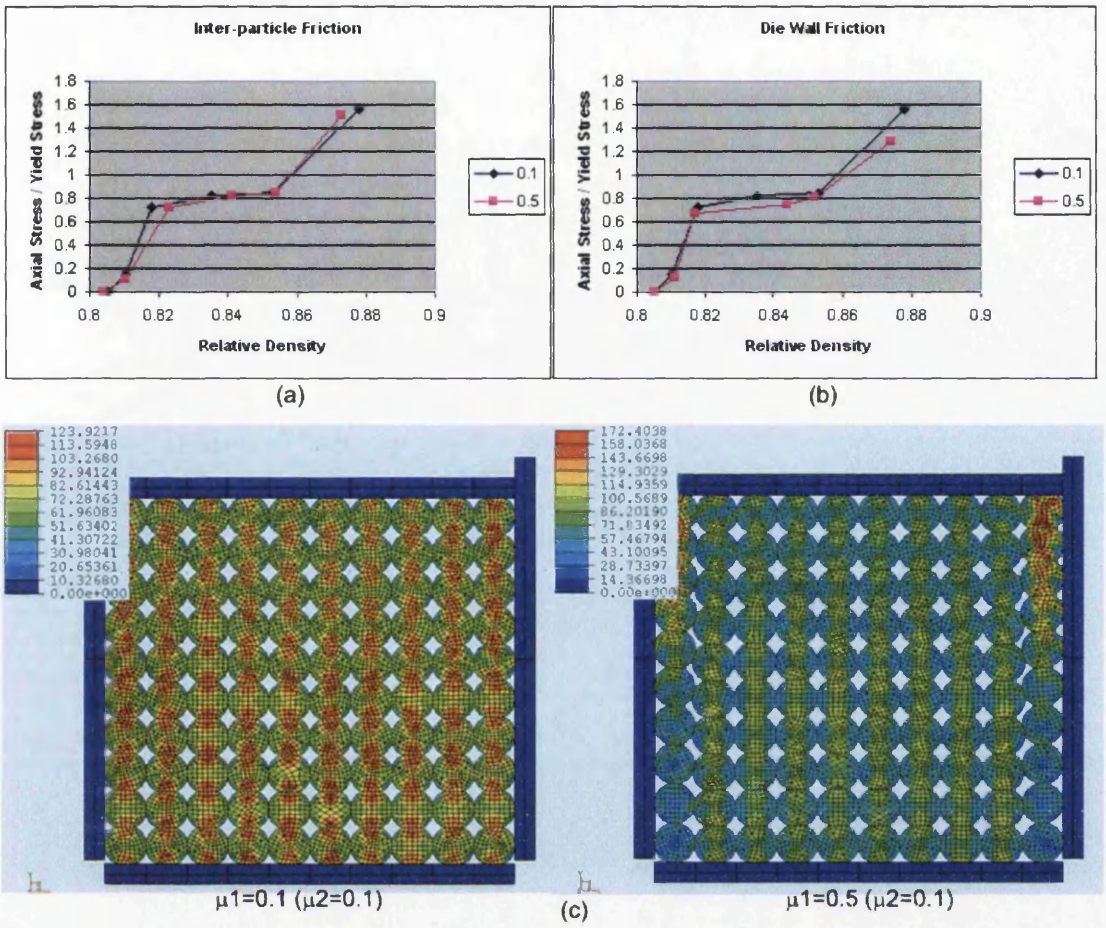

Figure 5. 17 Graphs of Relative Density against Stress Ratio (OFHC Cu) with the Variation of (a) Inter-Particle Friction Coefficient (μ_2) (b) Die Wall Friction Coefficient (μ_1) and (c) Schematic Diagrams of Effective Stress (for μ_1)

Figure 5.16 and 5.17 show the results for the hard and soft powder types. It can be clearly seen that the effect of friction between die wall and particles was more significant than that of inter-particle friction as the compaction proceeds. Compared to inter-particle friction coefficient having less effect, the friction between particles and tooling was apparent. For a better comparison, closer relative density values are needed. In this analysis, these were not controllable, however this may be established through additional data output and postprocessing. Also, from Figure 5.16, the ratio between axial and yield stress was higher throughout the process in the case of increased friction coefficient between die wall and

particles for the same degree of packing (relative density). This confirms the importance of friction between particles and tool set in die compaction. This is also supported by observing the stress contours (Figure 5.16(c)). However, for softer material, the stress ratio was slightly less when the friction coefficient between die wall and particles increased (Figure 5.17). This may be attributed to the deformation process taking place, which reduces the effect of increased friction coefficient. Similar results were reported by [Mallender, 1972], where experiments showed lubricated die wall was much more influential than lubricant on powders, i.e. highlights the importance of die wall friction compared to the inter-particle friction.

5.5.2 Initial Packing Geometry

In order to explore the effect of different initial packing geometry, two models were designed comprising a mixture of 50 large (10mm diameter) and 50 small (4mm diameter) circular particles. All the other constraints were identical for two cases except for the difference in initial packing geometry. The choice of two different particle sizes provides the opportunity to increase packing density, or when combined with an initial arrangement (defined via a random packing algorithm [MacroPac, 2001]) provides the opportunity to establish lower, possibly more realistic starting point density. Using this approach, the initial density achieved was around 0.7 and identical for two different initial geometry models.

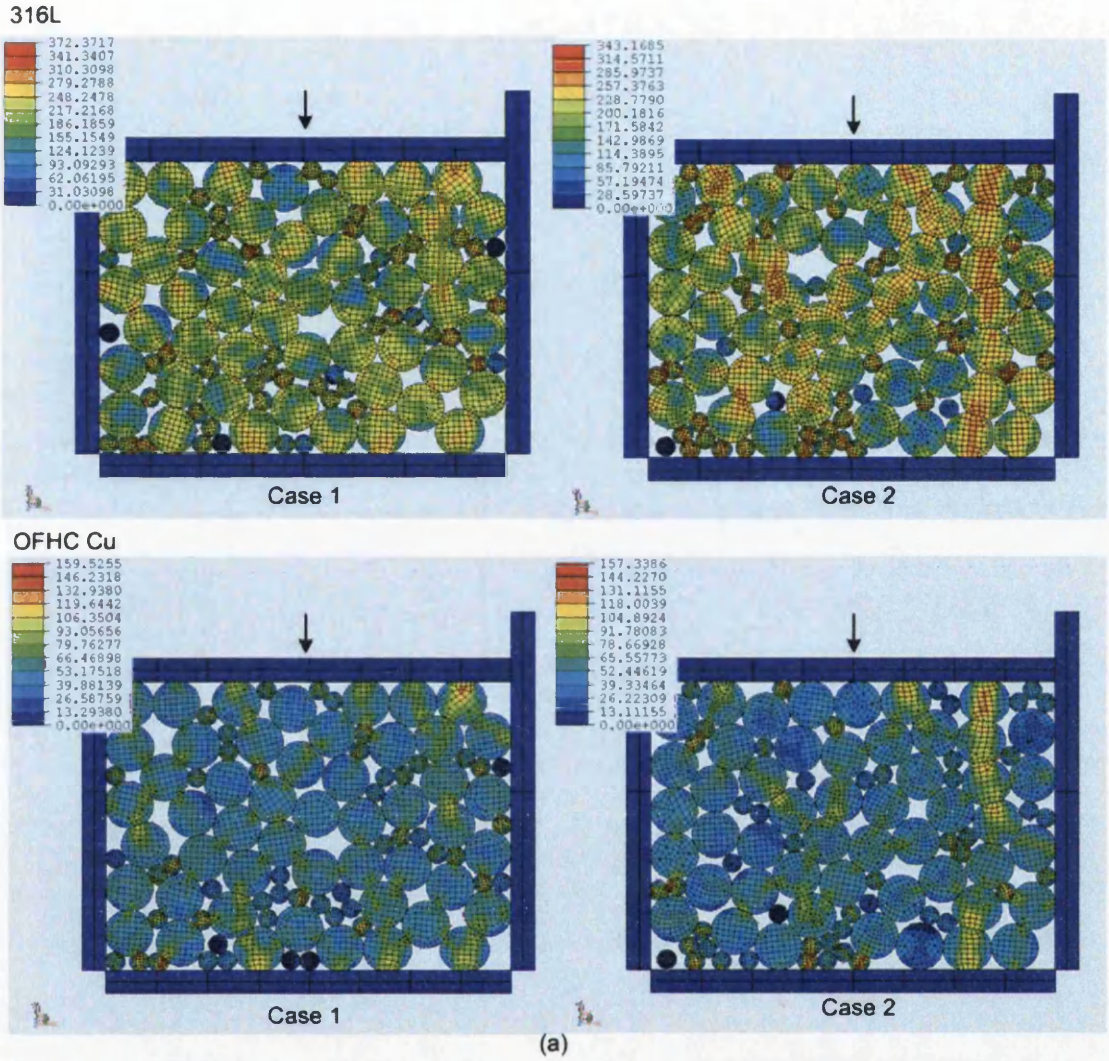

Figure 5. 18 (a) Schematic Diagrams of Effective Stress for Different Initial Packing Geometry (b) Graphs of Relative Density against Stress Ratio for Two Cases

Figure 5.18(a) show stress contours of two different initial packing geometry (case 1 and 2) for two materials at the end of the simulation process. The graphs illustrate a similar pattern for both cases, which seemed to mean that the simulation is less dependent on initial geometry in the case of 100 particles. These curves start to show a more clear increase in load as compaction proceeds.

The graphs agree well with the compression curves for experimental work in Chapter 3 (Figure 3.8 and 3.9). This highlights the need for initial random packing, rather than regular matrix that leads to a stiff response. This also confirms the ability of the model to reflect the conditions, randomly packed geometry and mixed size particles, of the actual experiment.

5.5.3 Particle Size

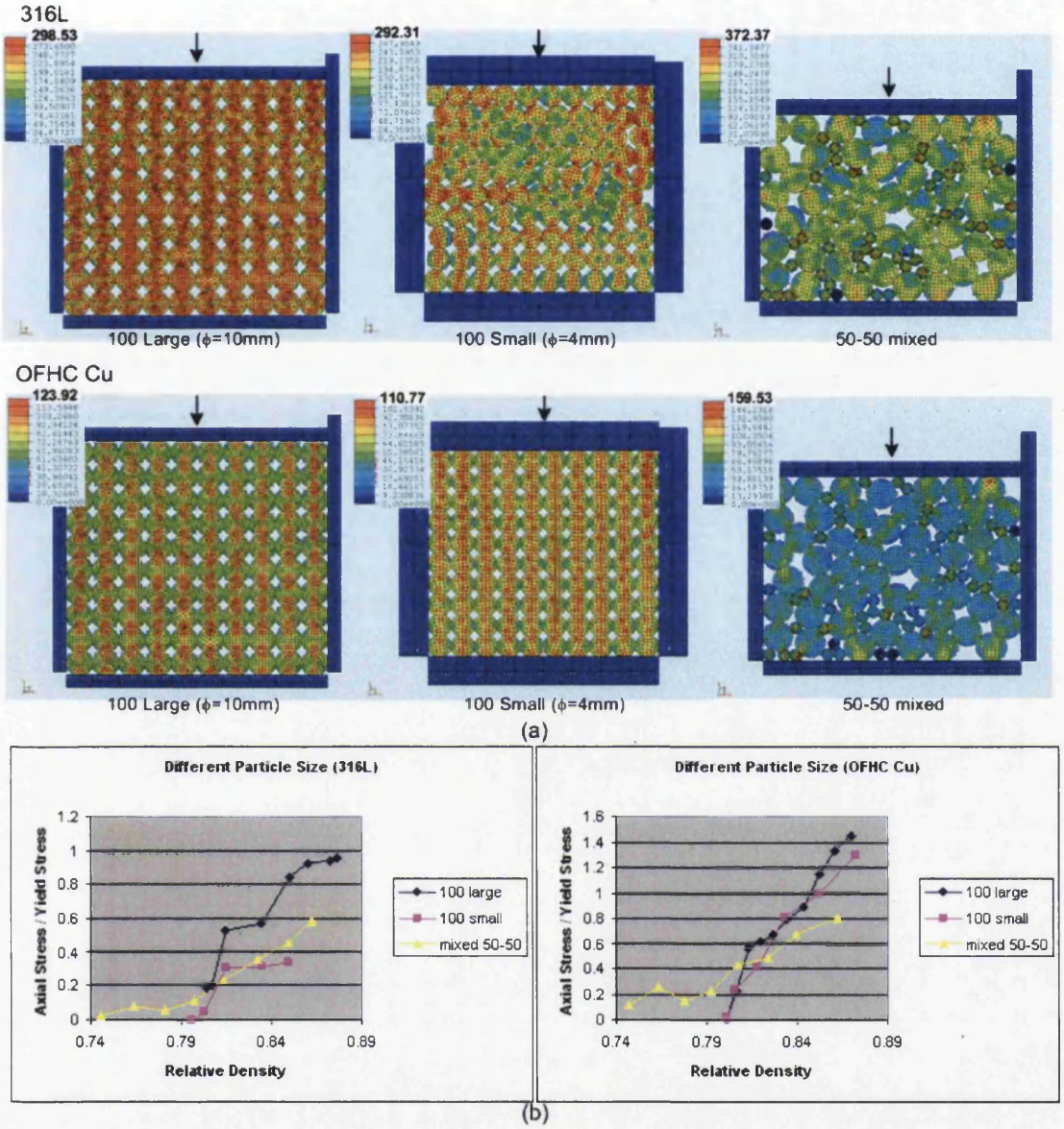

Figure 5. 19 (a) Schematic Diagrams of Effective Stress for Different Particle Size (b) Graphs of Relative Density against Stress Ratio for Different Size Cases

The comparison for models with different size of particles in a compact is illustrated in Figure 5.19. They were compacted by the same percentage (i.e.10 percent of the initial height) for the monosized particles in a regular matrix.

However, it was difficult to apply the same condition for the mixed model since not all particles were in contact with each other at the initial stage, i.e. different starting density and hence different force evolution. This can be clearly observed from Figure 5.19(b), where the initial relative density of the mixture of powders was much lower than the other two models. However, the mixed model reflects a more realistic experimental environment and therefore displays a similar force evolution pattern.

Change in size of the particles had significant impact on the stress levels for the harder ductile material, where for the softer material the difference was much less. This can be explained by comparing the stress contours of both materials for 100 small particles. In contrast to the model with softer material almost maintaining the original geometry, the model with harder material had numerous rearrangement processes taking place. This seems to be because the deformation process initiates much later in the case of harder particles allowing them to rearrange, slip and rotate in the mean time.

With a mixture of different sized particles, a gradual increase in axial stress can be seen in both cases.

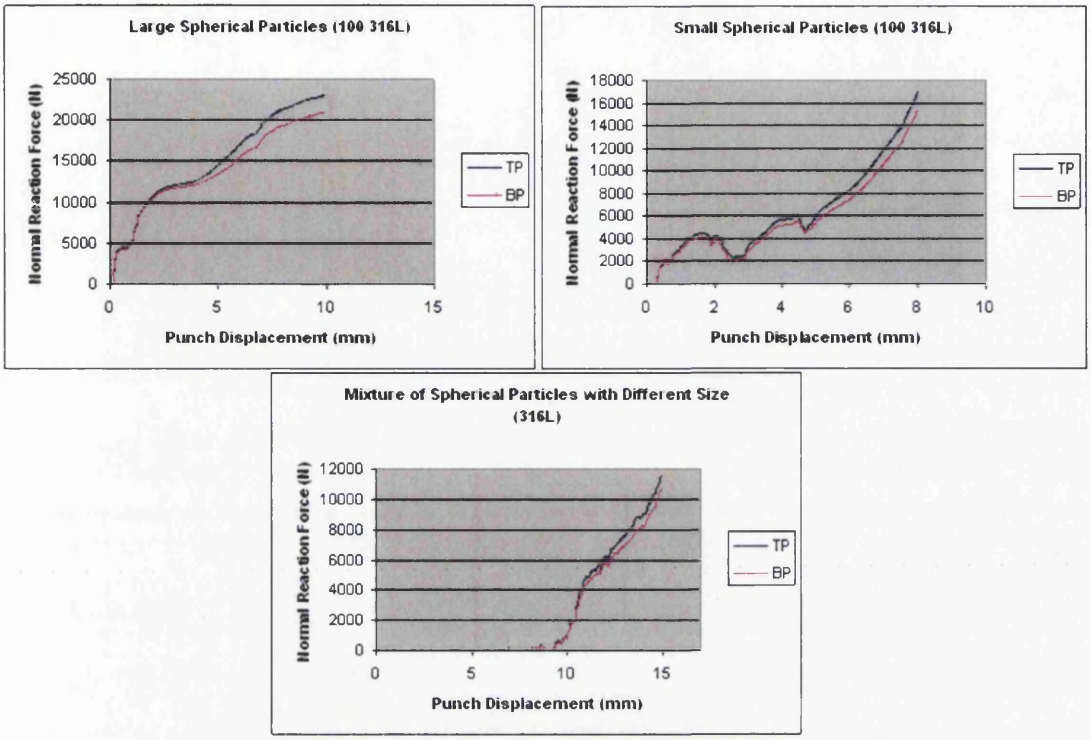

Figure 5. 20 Graphs of Punch Displacement against Normal Reaction Force for 100 Large, 100 Small and Mixture of Different Sized Particles (316L)

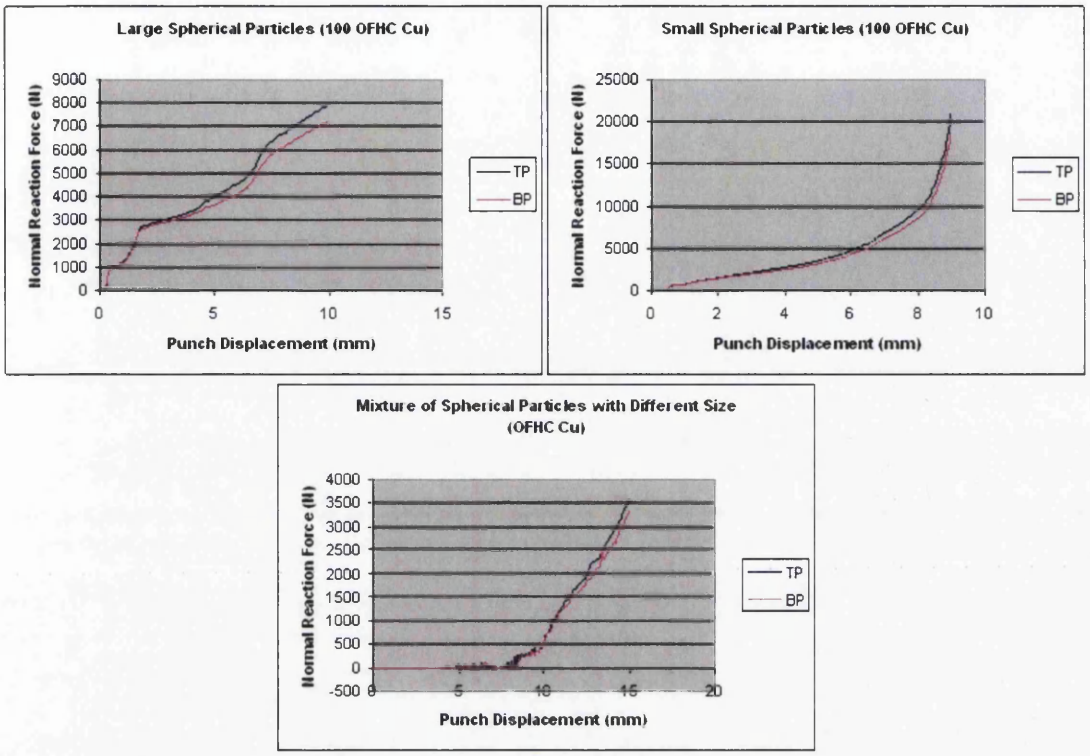

Figure 5. 21 Graphs of Punch Displacement against Normal Reaction Force for 100 Large, 100 Small and Mixture of Different Sized Particles (OFHC Cu)

Figure 5.20 and 5.21 show the behaviour of reaction force in normal direction on top and bottom punch (TP and BP) for two materials. As mentioned previously in relative density against stress ratio graphs, the model with mixture of particle size and randomly packed displays the smoother increase in force for both materials. The monosized regular matrix packed models (100 large and 100 small) show step increase in force as explained before in Figure 5.12. The model with 100 small particles for OHFC Cu displays a smooth increase in force, but this may be due to the soft particles deforming in response to the force levels.

5.5.4 Particle Shape

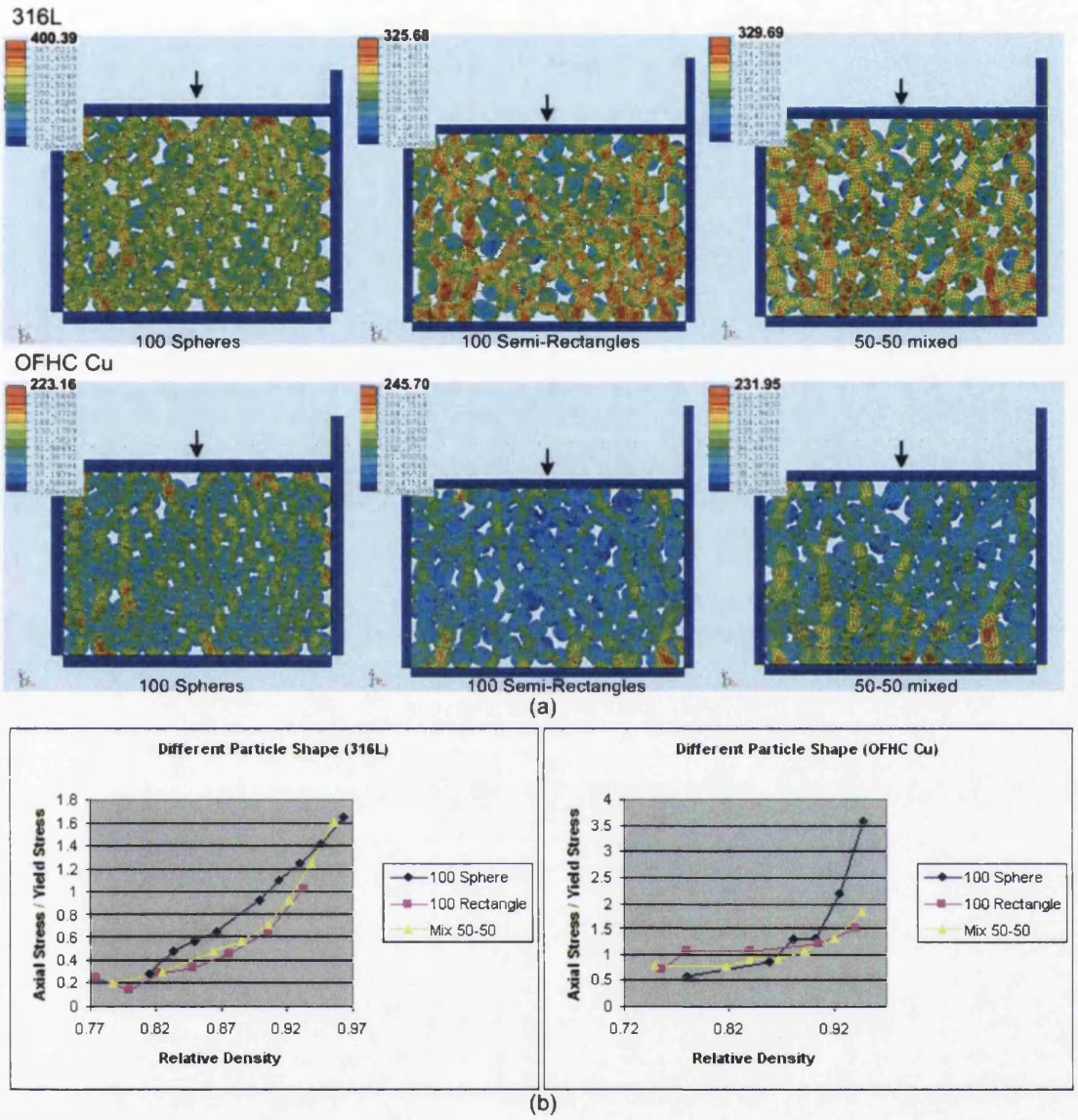

Figure 5. 22 (a) Schematic Diagrams of Effective Stress for Different Particle Shape (b) Graphs of Relative Density against Stress Ratio for Different Shape Cases

All the geometries for this investigation started from a random initial packing. Although the compaction response for each case is different, they show a similar pattern for both materials (Figure 5.22(b)). Comparing the two materials, the

average stress ratio for the softer material was higher and the particles have exhibited yielding.

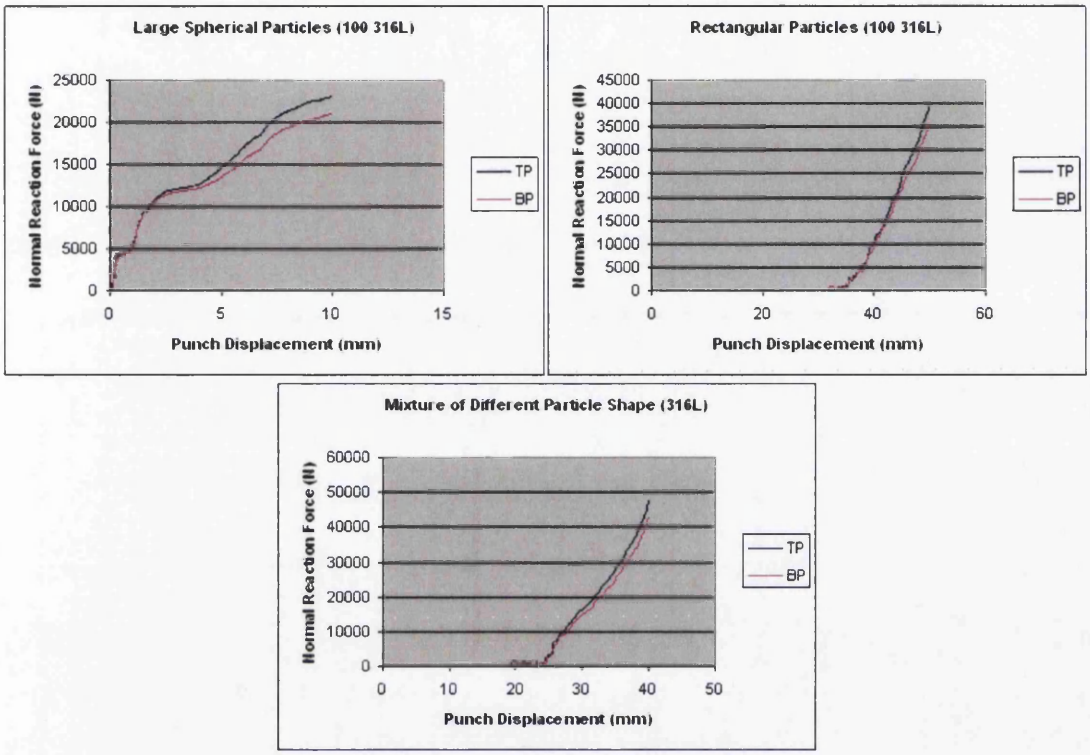

Figure 5. 23 Graphs of Punch Displacement against Normal Reaction Force for 100 Spherical, 100 Semi Rectangular and Mixture of Different Shaped Particles (316L)

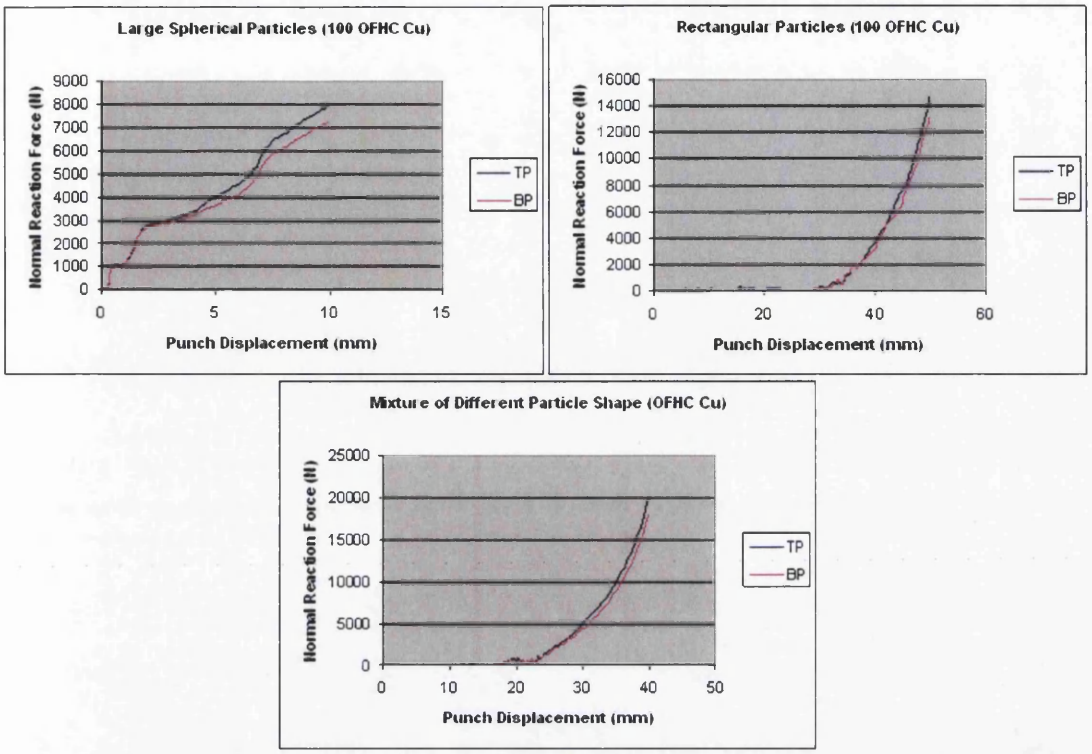

Figure 5. 24 Graphs of Punch Displacement against Normal Reaction Force for 100 Spherical, 100 Semi Rectangular and Mixture of Different Shaped Particles (OFHC Cu)

By observing both Figure 5.23 and 5.24, the general pattern for each case was similar for both materials. The force levels on both top and bottom punches were higher for the hard material (Figure 5.23) than the softer one. Additionally, the difference in reaction force between top and bottom punch was larger in the case of harder material. From the graphs, the model with a mixture of different shaped particles followed the pattern of the case with 'semi rectangular' particles. This seems to be due to irregular and complex shaped particles being more influential to the force output than the simple circular particles.

5.6 CLOSURE

Simulation by use of a combined discrete and finite element modelling for compaction has been reported in this chapter to further explore compaction mechanisms found in Chapter 3. Simulation as well as process related issues have been investigated, including comparison against other work where this is possible.

The key findings of this chapter are that the simulations are in agreement with previously published work.

Round regular packing leads to prescribing a high density and an uncharacteristic compaction response, exhibiting a stiff nature.

Random packing allows a more practical initial density and leads to a more characteristic compaction response.

6

FRICTION MODELLING

6.1 INTRODUCTION

As an extension of compaction modelling in Chapter 5, friction mechanisms, which were observed in the experimental work of Chapter 3 will be explored further by using the micro-mechanical modelling approach. This will be achieved by adapting the combined discrete and finite element numerical procedure reported in the previous chapter.

In this chapter, further verification and exploration of the friction behaviour observed in experimental findings will be attempted.

6.2 MODEL BUILD STRATEGY

Comparative to the study reported in Chapter 4, where friction mechanisms using the model of an AFM were explored, particles and the containing die has been modelled in this chapter.

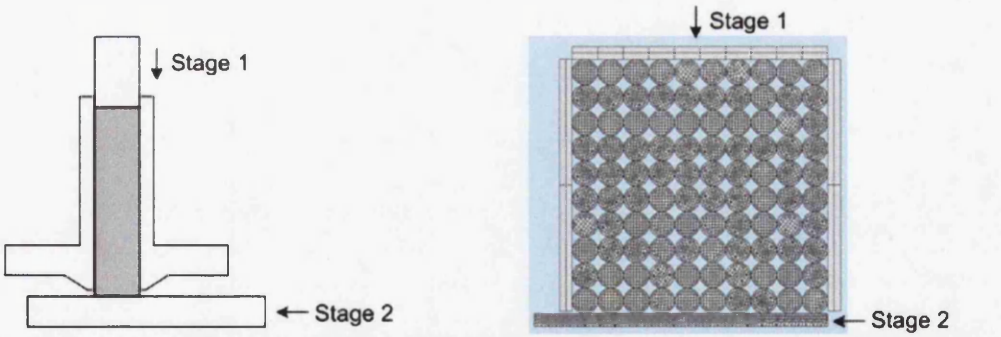

Figure 6. 1 Schematic Diagrams of (a) Tooling Surrounding the Powder for the Experiment (b) An Example of Friction Model

Figure 6.1(a) shows the schematic diagram of the experiment and Figure 6.1(b) shows an example of how it is represented using the DEM-ELFEN software.

For most of the models presented in this chapter, similar characteristics were used as for the compaction modelling in the previous chapter. Again, the models built in this chapter follow the generic steps as summarised in Chapter 4.

The contact in the models was detected automatically by the use of ELFEN software [ELFEN, 2001], which implements the DEM theory stated before. The model emulates the test fully through a compression stage followed by a shearing stage. The tools in the compaction process are considered to be rigid with all surfaces being perfectly smooth, and loads were applied by the displacement of the top punch. As it can be observed from Figure 6.1, the control parameter of applied load differs between the experiment and the simulation. Although better comparison might be possible with having an identical control parameter, the use of the software had limitations in that it is difficult to use the software to maintain a set force level. The force control parameter exists within the software, but by using this feature, the change in displacement will be very large over the initial stages and this will lead to computational difficulties. Consequently, the punch was displaced such that top punch pressure was similar to that used in the experiment (low load) only for the purpose of comparison with experimental data. The rest of the models for exploring process parameters adopted higher stress to investigate frictional effects at higher compact density.

For all the models, material properties of 316L as summarised in Table 5.1 was used, and therefore a von Mises criterion was applied to capture any plastic behaviour of the material. Specification of elastic properties, the yield stress and hardening response of the material were assigned to the model to capture the reaction as deformation occurs. The plastic material response was also linked with hardening for all the case studies.

The number of particles used in the simulation was 100 in total and a friction coefficient of 0.1 was assigned at all tool surfaces. Die walls were fixed in all directions of displacement and the top punch was allowed to move vertically. Similar to the dimensions used in the previous chapter, circular particles with 10mm in diameter and 1.5:1.0 ratio (15mm/10mm) semi-rectangular particles with rounding radius, 40% of the minimum particle side were also used. The validation study uses smooth particles in a regular packing. The packing is justified because the particles are round, the tool surface finish is good (Ra=0.1μm for the smoothest surface) and so the particles will arrange in their closest packing.

The regular matrix models require definition of position and geometry of each particle separately as well as defining the containing punch and die system and for the random packed models, the geometric packing software MacroPac [MacroPac, 2001] was used.

The factors explored in the case studies are itemised below in Table 6.1.

Factors Studied	Cases Studied (All Cases on Both Smooth and Rough Target Surfaces)
Particle size to surface roughness effects	- Large particles (diameter 10 units) - Small particles (4 units)
Initial packing geometry effects	- Regular matrix geometry - Randomly packed geometry
Particle shape effects (monosized)	- Spherical particles - Semi-rectangular particles
Particle shape effects (mixed)	- 50 large and 50 small spherical particles - 50 large spherical and 50 semi-rectangular particles

Table 6. 1 Case Studies for Friction Modelling

Prior to exploring the case studies, a validation model was used to compare the frictional force evolution with experimental trends at comparable stress levels.

6.3 RESULTS

6.3.1 Comparison with Experimental Data

In order to emulate the stress levels of the experimental work described in Chapter 3, a normal reaction force of 1kN for a punch diameter of 15mm was set as reference. This gives a stress value of $5.66N/mm^2$. The model used comprises

100 monosized circular particles in a regular matrix (Figure 6.1(b)), which is two-dimensional and it regards the particles as columns with thickness value of 1. Therefore, the stress in the model is the normal direction reaction force divided by the length of the top punch. Since the compaction was in the form of applied displacement, appropriate punch displacement was investigated to achieve $566N$ reaction force as shown below in Figure 6.2.

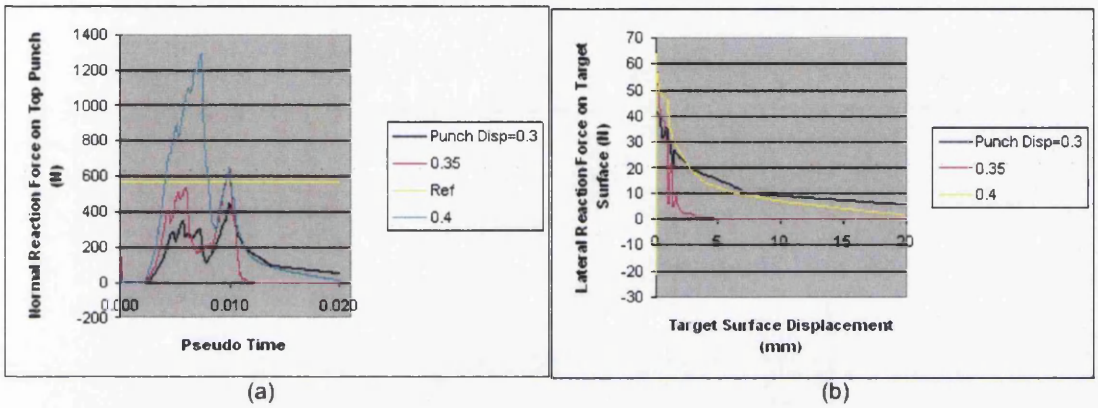

Figure 6. 2 Graphs of (a) Reaction Force in Normal Direction on the Top Punch against Test Time (b) Reaction Force in Lateral Direction on the Target Surface against Target Surface Displacement for Emulating Experimental Work

The compaction phase ends at test time 0.01, where the target punch displacement is achieved. It can be observed that with low loads applied, slight rearrangement of the particles results in fluctuating force levels on the top punch. The reduction in reaction force in the shear phase represents the force transmission to the particles. This differs from the experiment where it was maintained at a set level overall reflecting the fact that the press was controlled by a set force parameter. Consequently, the punch was displaced to compact the powder further during the shear stage in the experiment (see Figure 3.9). As a result, if the punch was moved downward within the simulation, a similar result could be obtained, however to do so in an automatic way is challenging and requires access to source code to programme this feature. Such access is not available in the software that

was used in this project. However, if it were possible to conduct the experiment with a fixed punch position, then a fall off in top punch force would have been detected. Consequently, the result from the experiment and simulation are in qualitative agreement. Unlike a continuum simulation approach, the numerical scheme is capable of capturing the phenomena that are exhibited in the experiments that are conducted at low pressure.

Figure 6.2(b) shows the shear reaction force on the target surface against its applied displacement. Although the shear stress reduced significantly due to load reduction arising from the fixed top punch, it can be seen that stress levels settle towards the end of the displacement process, which again agrees with the experimental observation. This may be attributed to the particles being circular since this geometry allows the particles to move more freely, which results in less reaction force on the top punch on both normal and lateral direction. This will be tested further when non circular particles are compacted.

6.3.2 Particle Size to Surface Roughness Effects

Real surfaces are rough and therefore the impact of this on friction is an important parameter to investigate in friction measurement for powder compaction. The initial work on surface roughness and hardness have been reported in [Cameron, 2002], where a number of different target surfaces were used. However, in order to achieve further understanding of the mechanisms that are present in terms of particle size to roughness wavelength, investigation using irregular particles and random packings will be presented for the first time.

The particle size to roughness ratio investigation was first reported by [Strijbos, 1976] and two main friction mechanisms were proposed, particles sliding over the surface and locked in the grooves for the ratio greater and smaller than 1 respectively. These mechanisms seem to exist in the experimental work reported

earlier (Chapter 3) and therefore the ratio of particle size to surface roughness was chosen as a factor to investigate.

In the simulations that follow, higher stress level compared to the level used in experiment was applied (around 200MPa for regular and 100-150 for irregular) to investigate frictional effects at higher compact density. 200MPa is a typical radial pressure in an axisymmetric part for a compaction pressure of about 400 to 500MPa. The latter is a modest but practically relevant value and thus the radial pressure setting of 200MPa is appropriate.

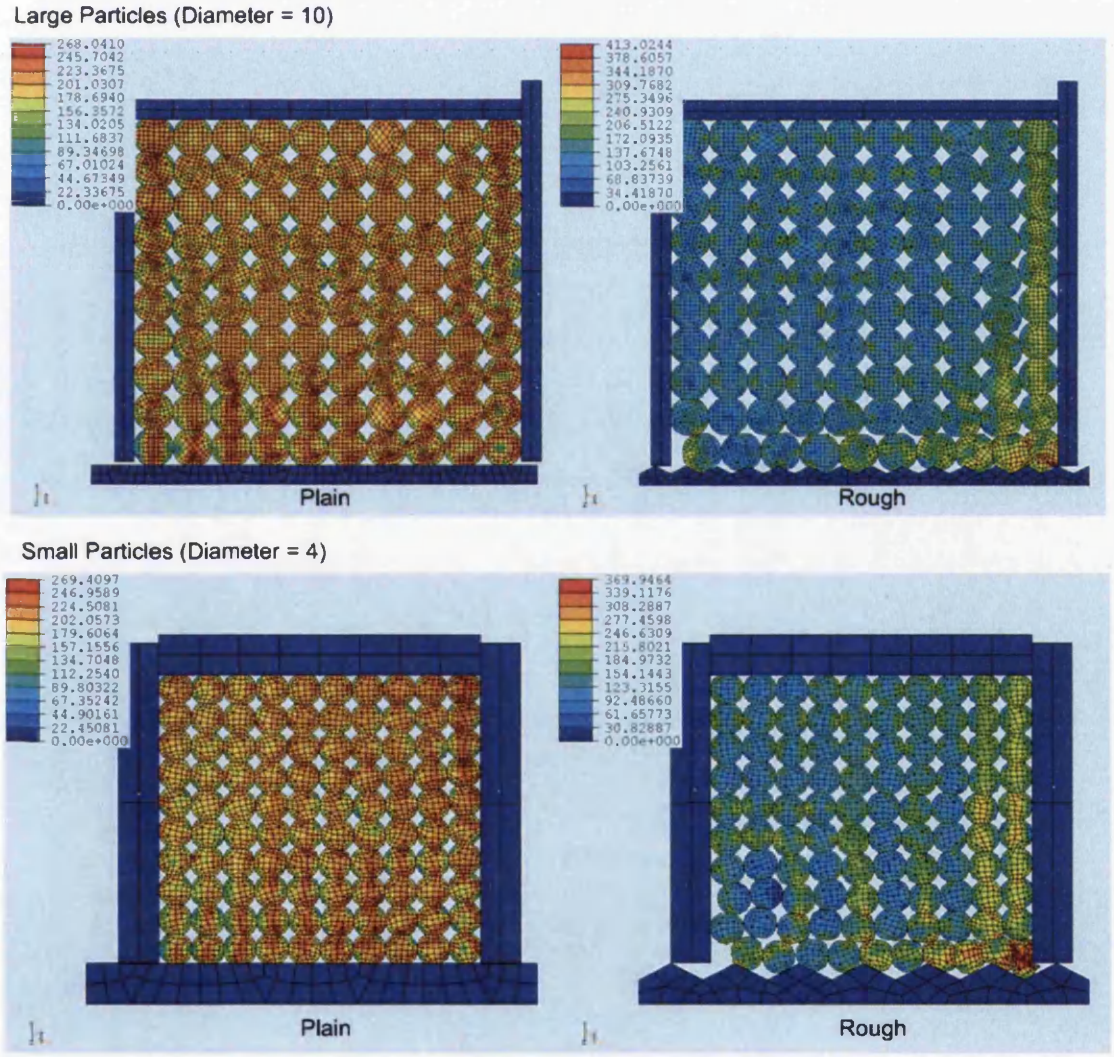

Figure 6. 3 Schematic Diagrams of Effective Stress for Large and Small Particles Model on Plain and Rough Surfaces

Figure 6.3 shows the stress contours at the end of the compaction and sliding process for large and small monosized particles in a regular matrix. First, it can be seen that for a smooth surface the stress levels within the particles are virtually identical, achieving nearly the same maximum value. The introduction of a rough target surface resulted in a higher stress in specific areas, principally in the region close to the right hand die wall, but leading to a reduction in the overall stress distribution. For the smaller particles, movement is more noticeable than for large particles, even for a smooth surface. This is particularly evident in Figure 6.3 in that the particle arrangement does not retain its initial columnar structure. The distance between peaks for the rough surface was 8 units, and therefore a maximum of 1 particle was locked in the groove for the large particle model, whereas for the small particle model, mostly two particles were fitted inside one groove. This seems to cause even more movement (i.e. rearrangement) for the particles. Additionally, the initial density of the compact for the rough surface model was lower (0.778) than the plain surface model (0.785) and hence allowed more freedom for particles to rearrange.

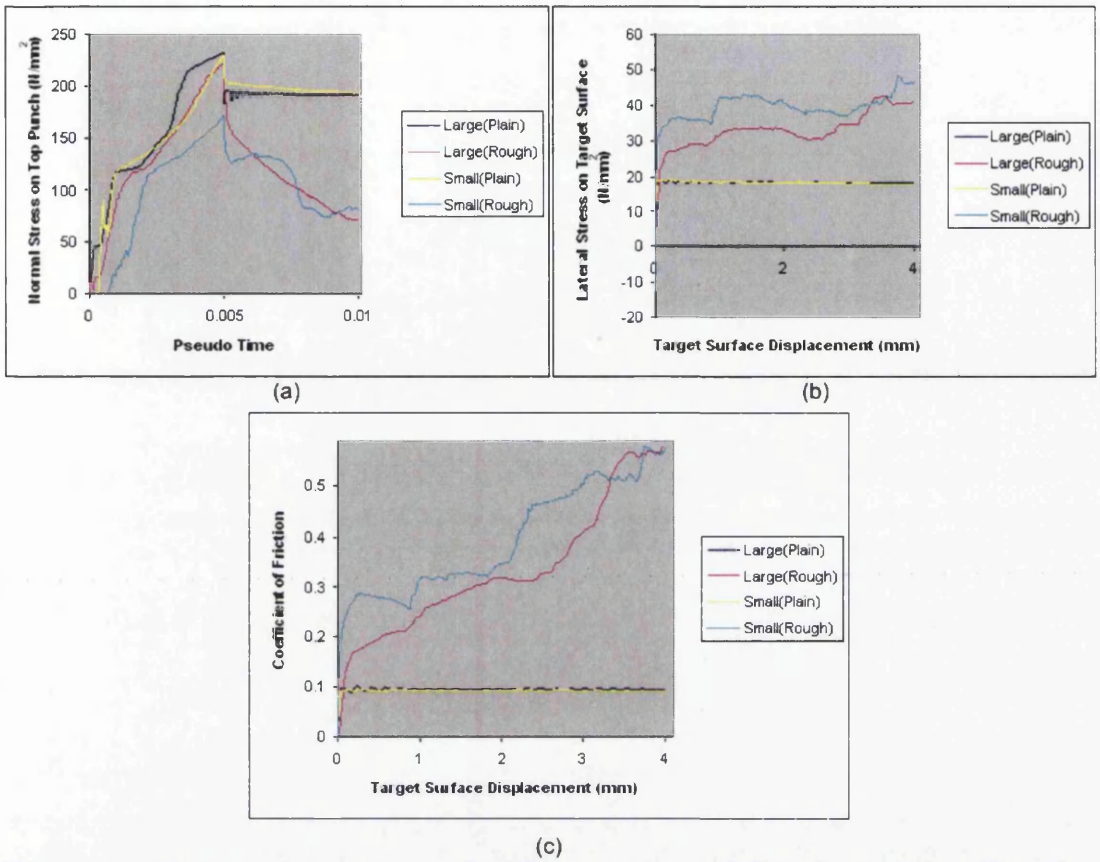

Figure 6. 4 Graphs of (a) Stress on Top Punch in Normal Direction against Test Time (b) Stress on Target Surface in Lateral Direction (c) Behaviour of Friction Coefficient against Target Surface Displacement for Particle Size to Surface Roughness Effects

From Figure 6.4(a), the normal stress level seems similar for the smooth (plain) surfaces for both particle sizes, whereas for the rough surface, the small particles model had a lower stress level than the other. This agrees with the observation of the stress contour above. As more rearrangement takes place, less stress will act on the top punch. Although the small particle model showed less stress in the normal direction, the lateral stress on the target surface was higher than for the large particle model (Figure 6.4(b)). This may be attributed to more particles being locked in grooves. Although [Strijbos, 1976] reported comparison between fine and coarse particles where the former was locked in the groove and the latter placed on top of the surface and slide, the particle size to roughness ratio exhibited in Figure 6.3 were both less than 1. As it was reported in [Cameron,

2000], friction was found to be greatly dependent on the position of the particles, this seem to be the main factor for higher friction coefficient as shown in Figure 6.4(c). With more movement allowed for the smaller particles, they were prone to be locked in a position where large deformation was observed. The friction coefficient for both models on a plain surface was 0.1 precisely correct as it was defined previously. However, as a consequence of the contribution due to roughness, the effective coefficient exceeds 0.1.

6.3.3 Initial Packing Geometry Effects

Principally the random packing allows the prescription of a more realistic initial density, plus it is a more realistic starting point since initial packing will not be on a regular matrix.

Similar to the random packed model reported in the compaction modelling chapter (Chapter 5), this will also be a first attempt at investigating its effects in friction modelling.

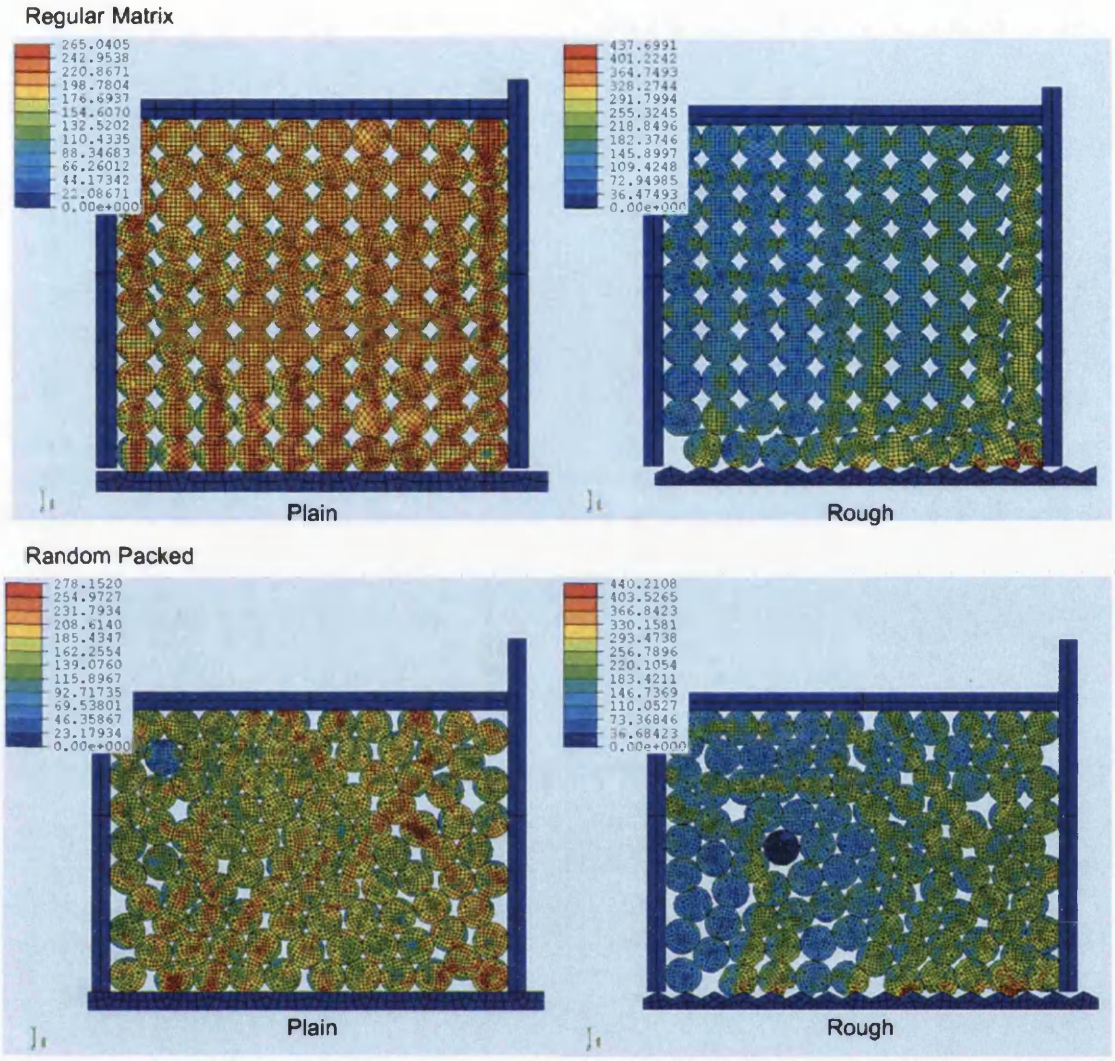

Figure 6. 5 Schematic Diagrams of Effective Stress for Initial Packing Geometry in Regular Matrix and Random Packed on Plain and Rough Surfaces

For comparison between regular and random packed geometry models, it is difficult to assimilate the compaction stress level for the two, since load was displacement controlled as mentioned previously. However, the effect of a rough target surface can be observed from Figure 6.5 where identical punch displacement was applied for both plain and rough surfaces. The distribution of stress is wider in the case of a random packed initial geometry model. This occurs because some initial packing results in particles being locked in place and these locked particles form the load transmission path. In the case of the rough target surface and a

random packing, the stress levels become more distributed through the matrix and this is in some contrast with the results from a smooth surface. In this instance, the rough surface provides sufficient disturbance such that the particles undergo further rearrangement and consequently the stress becomes more distributed through the matrix.

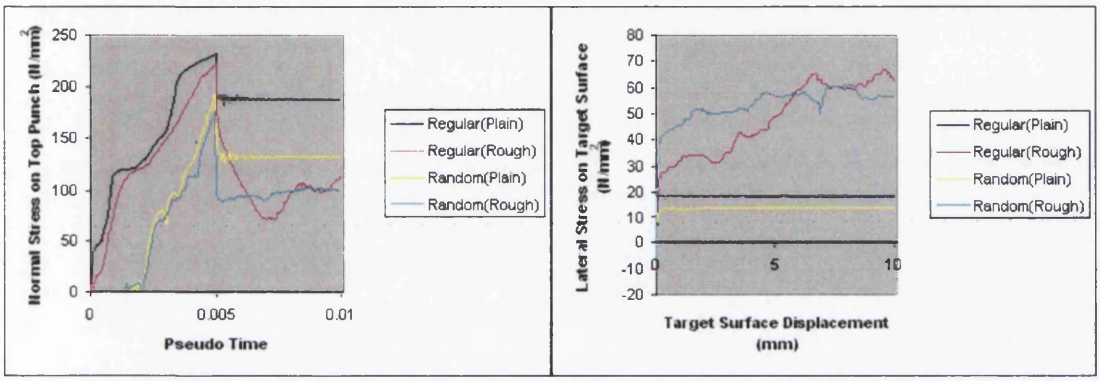

(a) (b)

Figure 6. 6 Graphs of (a) Stress on Top Punch in Normal Direction against Test Time (b) Stress on Target Surface in Lateral Direction against Target Surface Displacement for Initial Packing Geometry Effects

Apart from having differences in normal stress level, both regular and random packed models follow a similar pattern (Figure 6.6(a) and (b)). The main difference that can be observed is that the random packed model is already rearranged to settle, even though some particles are not perfectly in contact with each other. This results in a reduction of normal stress for the case of a rough target surface.

Observing both normal and lateral stress, the lateral stress in the rough surface is at a similar level for both cases.

With the random packing, the reduction in normal stress was much less than that of regular matrix when the shearing initiates, which shows a more realistic response that is closer to the experimental environment. This was also the case for lateral stress on the target surface where a smoother increase was observed.

6.3.4 Particle Shape Effects (Monosized)

Particles can exhibit shapes that are often linked to their manufacture, for example, gas atomised particles are generally spherical whereas particles such as sugar and salt are rectangular due to their crystalline nature. This section explores the effect of particle shape on compaction characteristics. In exploring particle shape, the cross sectional area of the rectangular particles are equivalent to the diameter of the round counterparts. Achieving near identical stress levels at the end of the compaction stage was again difficult due to random packing, where again a trial and error method was used to achieve this.

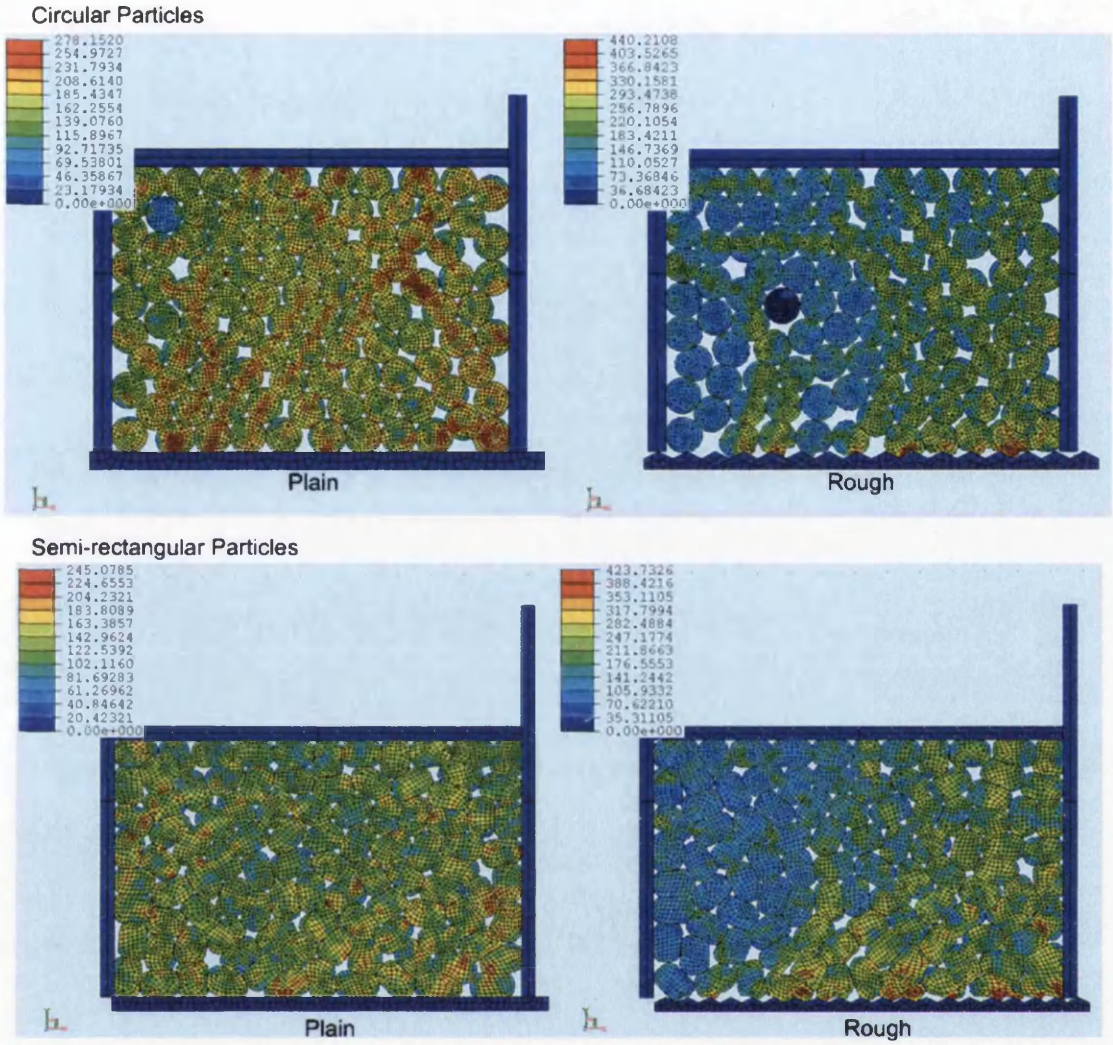

Figure 6. 7 Schematic Diagrams of Effective Stress for Different Particle Shape (Monosized) Models on Plain and Rough Surfaces

From observing Figure 6.7, the key difference is that the semi-rectangular particles have limitation in their movement, which has led to more deformation. With more deformations taking place, the relative density is higher even though the stress levels for both rough and smooth surfaces were both lower than the circular particle model.

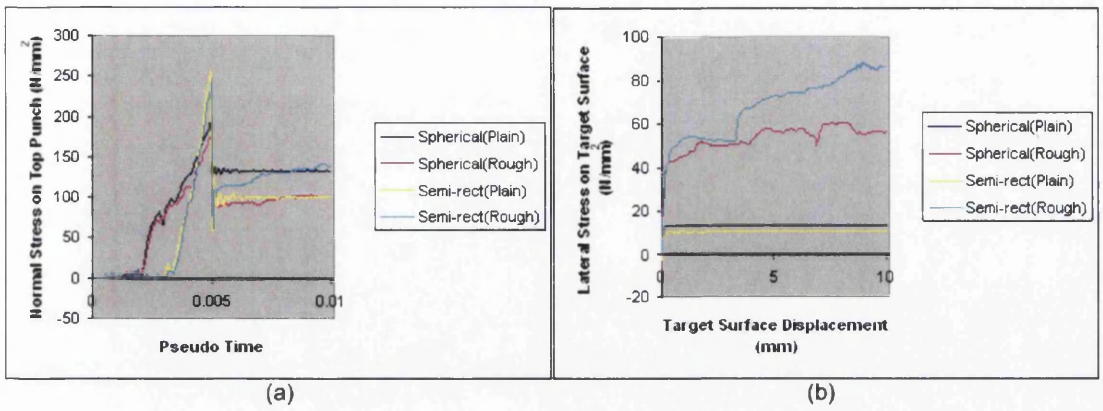

(a) (b)

Figure 6. 8 Graphs of (a) Stress on Top Punch in Normal Direction against Test Time (b) Stress on Target Surface in Lateral Direction against Target Surface Displacement for Different Particle Shape (Monosized) Effects

The effect of different shaped particles (semi-rectangular) on normal and lateral stress is shown in Figure 6.8(a) and (b). Differing from the previous results regarding circular particles, the normal stress on the top punch increased when the rough target surface was introduced and sliding initiated. This was due to geometric rearrangement, where the semi-rectangular particles are forced to move against each other and due to their aspect, they can become more firmly wedged against the top punch and so increase the force on this tool component. Thus, the increase in normal stress for a rough surface was only found in models with semi-rectangular particles (also in Figure 6.10(a) below). In the case of a fixed top punch loading, this would lead to a dilation mechanism in which there would be a local reduction in compact density. This is often regarded as an indicator of cracking within a powder compact.

6.3.5 Particle Shape Effects (Mixed)

In a more realistic point of view, perfectly monosized particles are difficult to manufacture, and thus a mixture of different particle shapes for the compact would reflect more of experimental conditions. The effect of mixed particle shape on compaction characteristics are explored in this section, where dimension of the particles followed that of the monosized particle shape investigation above.

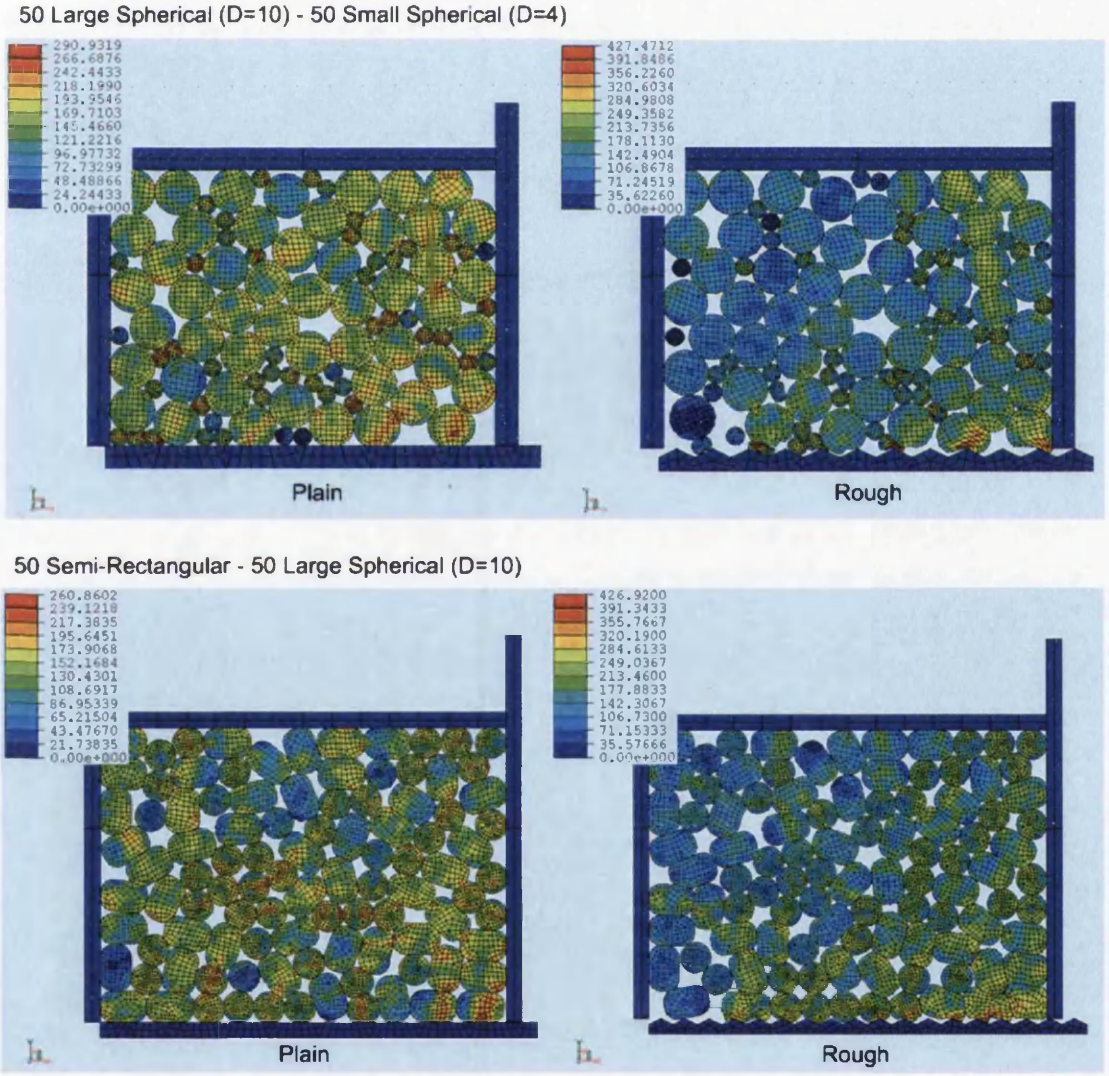

Figure 6. 9 Schematic Diagrams of Effective Stress for Different Particle Shape (Mixed) Models on Plain and Rough Surfaces

Figure 6.9 illustrates stress contours of mixed models for both plain and rough surfaces at the end of the process. Again, it shows that the model containing only circular particles are allowed more freedom than the mixed shaped model (i.e. lower relative density).

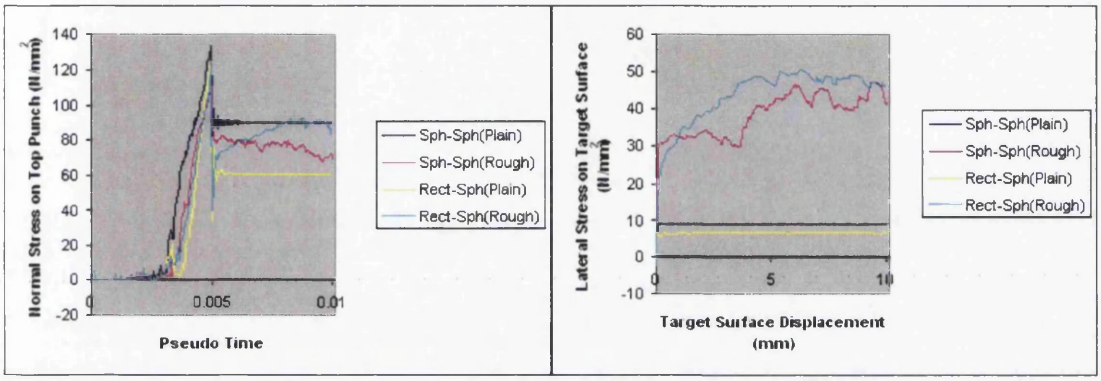

(a) (b)

Figure 6. 10 Graphs of (a) Stress on Top Punch in Normal Direction against Test Time (b) Stress on Target Surface in Lateral Direction against Target Surface Displacement for Different Particle Shape (Mixed) Effects

The mixture models display relatively smooth increase in normal stress during the compaction process as reported in Chapter 5. For the large and small circular particles mixture, it was observed that the normal stress decreased since more rearrangement was allowed than the model containing monosized circular particles. Although the semi-rectangular particles over rough surface were wedged again against the top punch resulting in increase of stress in both normal and lateral direction, the inclusion of circular particles reduced the rate of increase and eventually the stress level settled. These models may be the closest to the actual experimental conditions in terms of geometry as shown in Figure 3.5. Although the models in this chapter utilises material properties of 316L (hard ductile), they can be related to other materials purely in geometric point of view.

6.3.6 Behaviour of Friction Coefficient

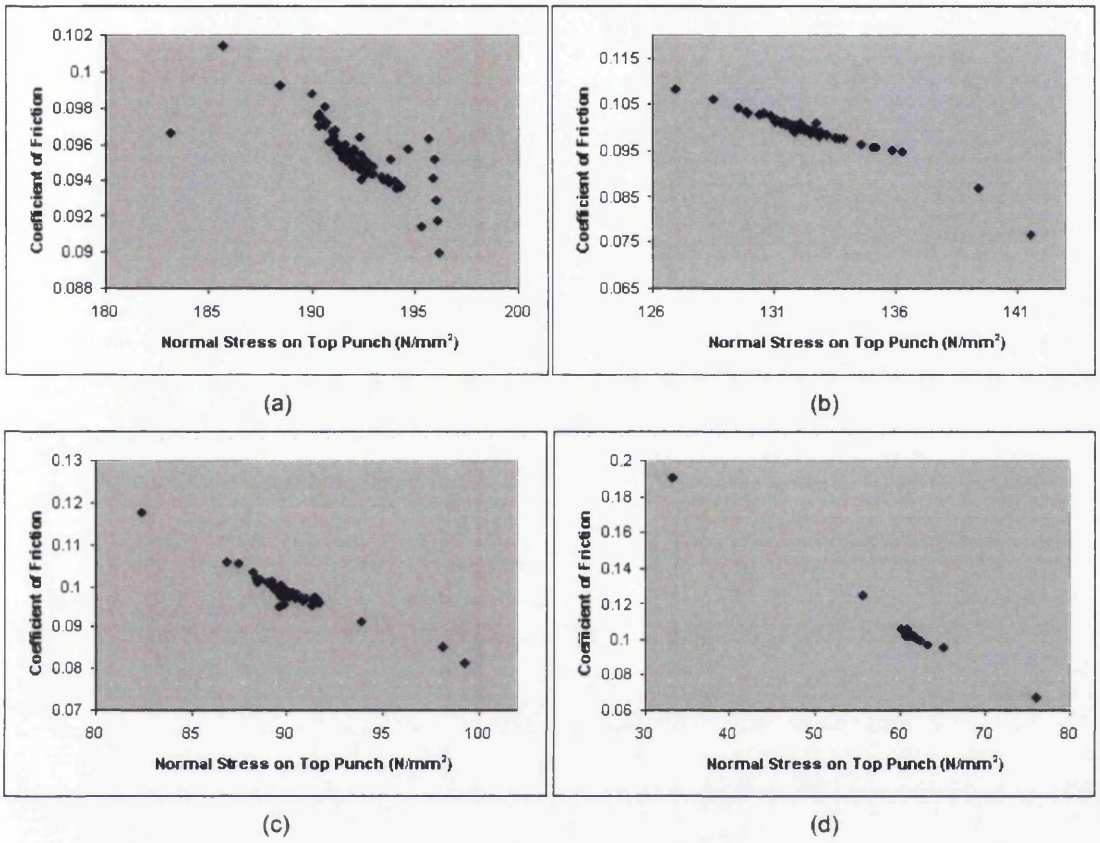

Figure 6. 11 Graphs of Coefficient of Friction against Stress on Top Punch in Normal Direction for (a) 100 Circular Particles in Regular Matrix (b) 100 Circular Particles in Irregular Matrix (c) 50-50 Circular Particles (Mixed Size) in Irregular Matrix (d) 50-50 Mixed Particles (Mixed Shape) in Irregular Matrix

Figure 6.11 shows distribution graphs of friction coefficient against stress in the normal direction. For all cases, it can be observed that the friction coefficient decreases as the stress increases. This behaviour was especially apparent for cases with irregular packing, which agrees well with experimental findings reported by a number of investigators [PM Modnet, 2002], [Solimanjad, 2003].

6.4 CLOSURE

A further investigation on friction mechanism was performed using two-dimensional discrete element model to understand experimental findings reported in Chapter 3.

The issues of importance identified from the experiments have been explored, i.e. particle size to roughness, initial packing geometry, particle shape (monosized and mixed) effects. These factors were explored on smooth and rough surfaces highlighting each effect.

The emulation of the sliding plate test was possible although the control parameter for load was different (force controlled in experiment and punch displacement for emulation model).

It was found out that the rough surface clearly leads to higher friction coefficient, where it contains both plain friction and topographical effects. Also, the rough surface leads to changes in the average stress distribution through the compact, i.e. higher distribution against the restraining wall.

In order to explore a more realistic behaviour of friction mechanism, the random packing models were introduced, which brings closer to experimental conditions. For the random packing over a rough surface, the stress distribution was spread wider than that of particles in a regular matrix due to further rearrangement taking place.

The irregular shaped particles can interlock in the case of a rough surface and lead to increases in punch loading, or dilation in the case where a punch load could be at a set value.

The behaviour of friction coefficient was explored as a function of stress and the results were in good agreement with the experimental findings.

7

CONCLUSIONS AND RECOMMENDATIONS

In this thesis, work has been undertaken in the following areas:

- Experimental Investigation of Friction Mechanisms (macro scale)
- Numerical Modelling of Micro Scale Friction Measurement Method (AFM)
- Numerical Modelling of the Compaction and Shear Process

7.1 MACRO SCALE FRICTION MEASUREMENT

Experimental investigation on friction mechanisms was proposed by using a newly designed extended sliding plate apparatus, featuring low load and longer sliding distance.

Prior to exploring the friction mechanisms, control stabilisation tests were performed and appropriate control parameters were found to assure smooth compression at the set loading rate. Also, the consistency of the equipment was tested and found to be very good.

The results from the experiments were examined to explore friction between powders and target surfaces with the variation of different powders, loads, surface finishes, and speed. The static and dynamic friction for both ductile and brittle powders was identified and its behaviour compared with previous work.

Important factors in friction mechanism were identified that included particle size, particle shape, material response (ductile or brittle), and surface topography (surface roughness).

7.2 ATOMIC FORCE MICROSCOPY MODELLING

Numerical modelling of the AFM experiment was carried out with the aim of exploring the micro scale friction mechanisms. For this purpose, the calibration of AFM was critical, which involves mechanical stiffness and detector (PSPD– position sensitive photodiode) calibration.

To explore mechanical response, models were built to simulate the operations of an AFM incorporating a standard and colloid probe tip and exploration of response in both normal and lateral direction was investigated. It was found that response in the normal direction was much more sensitive than that in the lateral.

The results from the model were compared to approximate mathematical models from previous work for both simple beam and V-shape cantilever. Results showed general agreement in trend, but with significant discrepancies in value for both normal and lateral stiffness.

For the purpose of friction measurement, twisting of the cantilever was identified as the main initial response for both cantilevers, but especially for the V-shaped design. The significant lateral bending for a beam design could not be neglected – it can represent typically 45 percent of the deflection. The overall process of lateral response for both cantilever designs was investigated and generically it was found that the order was twisting, bending (with twisting), and finally slipping.

The material properties of the cantilever were significantly influential for both normal and lateral response, even local yielding was found in the area of fixity and on the tip end. Additionally, the importance of particle fixing position and its proximity to the cantilever line of symmetry was highlighted leading to combined normal deflection and twisting when a normal load was applied.

An emulation model was designed to explore dynamic sensitivity by comparing with the previously reported experiment on friction loops on an inclined surface where the results showed good agreement in response pattern.

7.3 COMPACTION MODELLING

The compaction stage of the macro scale friction measurement experiment was numerically modelled by use of a combined discrete and finite element modelling to explore compaction mechanisms found from the experimental work further.

This investigation included exploration of simulation factors (particle count, time step, and particle discretisation) and process parameters (friction coefficient, initial packing geometry, particle size, and particle shape). Initial comparison with previously published work showed reasonable agreement and the simulations were then used to explore process response to the range of particle scale factors. Friction coefficient parameter was investigated and the importance of friction was confirmed, especially between particles and die set.

A characteristically stiff response was observed for a model that used a regular packing of round particles that already prescribes a high initial density. In contrast to this high density, a more practical initial density was observed from a random packing of the particles and this resulting in a more realistic response, exhibiting rearrangement and compression stages. Additionally, it was found that the irregular and complex shaped particle were more influential to the force output than the simple circular particles.

7.4 FRICTION MODELLING

The numerical modelling with combined discrete and finite element method was extended to explore frictional mechanisms by inclusion of the shearing process.

This was again the emulation of the experimental work using the extended sliding plate, and therefore the frictional response with similar stress level in the normal direction was first explored. The result was in qualitative agreement with the experiment, since similar pattern were observed.

The factors identified from the experiments were explored, i.e. particle size to roughness, initial packing geometry, particle shape (monosized and mixed) effects. These factors were explored on smooth and rough surfaces highlighting each effect. Key findings included that the rough surface clearly leads to higher friction coefficient since it accounts for both plain friction and topographical effects. In addition, the average stress distribution changed leading to a higher level against the restraining wall when the rough surface was introduced for the round regular packing.

As it was found from the compaction modelling, again random packing models showed capability to obtain better reflection of the experimental conditions. The stress distribution for the random packing showed a wider distribution since further rearrangement occurred.

For the irregular shaped particles on a rough surface, interlocking was observed and this led to increase in normal stress on the top punch. This would lead to dilation in the case where a punch was force level controlled as for the experiment.

7.5 RECOMMENDATIONS

In order to explore friction mechanisms further, the extended sliding plate apparatus could be used for very fine powders highlighting the particle size to roughness effects. However, special consideration would be required in die filling, punch mounting, and the issue of cleaning the embedded powders in the target surface especially when higher loads are applied.

For the numerical modelling of AFM experiment, the difficulties, definition of dynamic sensitivity and preparation of colloid probe tip, should be taken into consideration. Future work will need to mainly focus on establishing the PSPD (dynamic) response as a means of completing the calibration loop for the instrument, by combining with mechanical stiffness prediction reported in this thesis.

The particle scale numerical modelling could be explored with finer discretisation, larger number of particles, and various shapes of particles with random packing to reflect experimental conditions better and thus to provide further understanding of the mechanisms that are present for powder compaction, given that computational power will be available.

In friction modelling, future work could include programming a 'force controlled' feature for applying load in simulation, which will provide clearer representation of the experiment. Additionally, investigation of irregular particles with random packing on a wide range of surface roughness could be useful in achieving further understanding of the friction mechanisms.

References

Aime, J.P., Elkaakour, Z., et al. (1995). Role of the force of friction on curved surfaces in scanning force microscopy. Surface Science **329**: 149-156.

Ando, Y. (2000). The effect of relative humidity on friction and pull-off forces measured on submicron-size asperity arrays. Wear **238**: 12-19.

ASM Metals Handbook. (1986). Properties and selection: nonferrous alloys and pure metals. ASM International **2**.

Baer, M.R., Trott, W.M. (2002). Theoretical and experimental mesoscale studies of impact-loaded granular explosive and stimulant materials. Sandia National Laboratories.

Beaulieu, L.Y., Godin, M., et al. (2007). A complete analysis of the laser beam deflection systems used in cantilever-based systems. Ultramicroscopy **107**: 422-430.

Bhushan, B., Sundararajan, S. (1998). Micro/nanoscale friction and wear mechanisms of thin films using atomic force and friction force microscopy. Acta mater **46**(11): 3793-3804.

Bowen, W.R., Lovitt, R.W., et al. (2001). Atomic force microscope studies of stainless steel: surface morphology and colloidal particle adhesion. Journal of Material Science **36**: 623-629.

Bowen, R., Wright, C. (2001). Atomic force microscopy: defining biotechnological processes. tce 34-36.

Cante, J.C., Oliver, J., et al. (2005). On numerical simulation of powder compaction processes: powder transfer modelling and characterisation. Powder Metallurgy **48**(1): 85-92

Cameron, I.M. (2000). Powder characterisation for compaction modelling. Department of Mechanical Engineering Swansea, University of Wales.

Cameron, I.M., Gethin, D.T., et al. (2002). Friction measurement in powder die compaction by shear plate technique. Powder Metallurgy **45**(4): 345-353.

Clifford, C.A., Seah, M.P. (2005). The determination of atomic force microscope cantilever spring constants via dimensional methods for nanomechanical analysis. Nanotechnology **16**: 1666-1680.

Cocks, A.C.F. (2006). Private Domain / Communication

Cundall, P.A., Strack, O.D.L. (1979). A discrete numerical model for granular assemblies. Geotechnique **29**(1): 47-65.

Demetry, C.A., Souto, F.S., et al. (1998). Tactile sensing of density uniformity in powder beds after die filling. Powder Technology **99**: 119-124.

Doremus, P., Pavier, E. (1998). Friction: experimental equipment and measuring. Proceedings of World Congress Powder Metallurgy 1998

Doremus, P., Toussaint, F., et al. (2001). Investigation of iron powder friction on tungsten carbide tool wall. Powder Metallurgy **44**(3): 243-247.

ELFEN User Manual 3.0. (2001). Rockfield Software Limited

EPMA Website. (2006). http://www.epma.com.

Fleck, N.A., Kuhn, L.T., et al. (1992). Yielding of metal powder bonded by isolated contacts. Journal of The Mechanics And Physics of Solids **40**(5): 1139-1162

Fuentes, R., Rubio, E., et al. (2003). Wear behaviour of a self-lubricating aluminium/graphite composite prepared by powder metallurgy. Industrial Lubrication and Tribology **55**(4): 157-161.

Gethin, D.T., Tran, V.D. (1994). An investigation of powder compaction processes. International Journal of Powder Metallurgy **30**(4): 385-398.

Gethin, D.T., Ransing, R.S., et al. (2001). Numerical comparison of a deformable discrete element model and an equivalent continuum analysis for the compaction of ductile porous material. Computers and Structures **79**: 1287-1294.

Gethin, D.T., Lewis, R.W., et al. (2003). A discrete deformable element approach for the compaction of powder systems. Modelling and Simulation in Materials Science and Engineering **11**: 101-114.

Gibson, C.T., Watson, G.S., et al. (1997). Lateral force microscopy-a quantitative approach. Wear **213**: 72-79.

Green, C.P., Lioe, H., et al. (2004). Normal and torsional spring constants of atomic force microscope cantilevers. Review of Scientific Instruments **75**(6): 1988-1996.

Guyoncourt, D.M.M., Tweed, J.H., et al. (2001). Constitutive data and friction measurements of powders using instrumented die. Powder Metallurgy **44**(1): 25-33.

Haggblad, H., Oldenburg, M. (1994). Modelling and simulation of metal powder die pressing with use of explicit time integration. Modelling and Simulation in Materials Science and Engineering **2**: 893-911.

Khan, A., Philip, J. (2004). Young's modulus of silicon nitride used in scanning force microscope cantilevers. Journal of Applied Physics **95**(4): 1667-1672.

Khoei, A.R. (2002). Numerical simulation of powder compaction processes using an inelastic finite element analysis. Materials and Design **23**: 523-529

Korachkin, D. (2006). Measurement methods for the determination of powder properties for compaction modelling. Department of Mechanical Engineering Swansea, University of Wales.

Liu, Y., Wu, T., et al. (1994). Lateral force microscopy study on the shear properties of self-assembled monolayers of dialkylammonium surfactant on mica. Langmuir **10**: 2241-2245.

MacroPac Intelligensys Website. (2001). http://www.intelligensys.co.uk/.

Mak, K.W. (2003). Discrete element modelling of particulate systems for industrial applications. School of Engineering Swansea, University of Wales.

Mallender, R.F., Dangerfield, C.J., et al. (1972). Friction coefficients between iron powder compacts and die wall during ejection using admixing zinc strearate lubricants. Powder Metallurgy **15**(30): 130-152.

Meine, K., Schneider, T., et al. (2002). The influence of roughness on friction, part 1: the influence of a single step. Wear **253**: 725-732.

Molecular Imaging Website. (2005). http://www.molec.com.

Munjiza, A. (2004). The combined finite-discrete element method. John Wiley and Sons Ltd

Nickel Institute Website. (2006). http://www.nickelinstitute.org.

Neumeister, J.M., Ducker, W.A. (1994). Lateral, normal and longitudinal spring constants of atomic force microscopy cantilevers. Review of Scientific Instruments **65**(8): 2527-2531.

Noldus Website. (2006). http://www.noldus.com.

Noy, A., Frisbie, C.D., et al. (1995). Chemical force microscopy: exploiting chemically-modified tips to quantify adhesion, friction, and functional group distributions in molecular assemblies. J. Am. Chem. Soc **117**: 7943-7951.

Ogletree, D.F., Carpick, R.W., et al. (1996). Calibration of frictional forces in atomic force microscopy. Review of Scientific Instruments **67**(9): 3298-3306.

PM Modnet Research Group (2002). Numerical simulation of powder compaction for two multilevel ferrous parts, including powder characterisation and experimental validation. Powder Metallurgy **45**(4): 335-344.

Procopio, A.T., Zavaliangos, A. (2005). Simulation of multi-axial compaction of granular media from loose to high relative densities. Journal of the Mechanics and Physics of Solids **53**: 1523-1551.

Ransing, R.S., Gethin, D.T., et al. (2000). Powder compaction modelling via the discrete and finite element method. Material and Design **21**: 263-269.

Ransing, R.S., Lewis, R.W., et al. (2004). Using a deformable discrete-element technique to model the compaction behaviour of mixed ductile and brittle particulate system. Phil. Trans. R. Soc. Lond. A **362**: 1867-1884.

Redanz, P. (1998). Numerical modelling of cold compaction of metal powder. Int. J. Mech. Sci **40**(11): 1175-1189.

Redanz, P., Fleck, N.A. (2001). The compaction of a random distribution of metal cylinders by the discrete element method. Acta mater **49**: 4325-4335.

Riedel, H., Sun, D.Z. (1992). Numerical methods in industrial forming processes. NUMIFORM **92**: 883-886.

Rowe, R.C., Roberts, R.J. (1995). The mechanical properties of powders. Advances in Pharmaceutical Sciences **7**: 1-62.

Sinka, I.C., Cunningham, J.C., et al. (2003). The effect of wall friction in the compaction of pharmaceutical tablets with curved faces: a validation study of the Drucker-Prager Cap model. Powder Technology **133**: 33-43.

Skrinjar, O., Larsson, P.L. (2004). On discrete element modelling of compaction of powders with size ratio. Computational Materials Science **31**: 131-146.

Solimanjad, N. (2003). New method for measuring and characterisation of friction coefficient at wide range of densities in metal powder compaction. Powder Metallurgy **46**(1): 49-54.

Song, Y., Bhushan, B. (2006). Simulation of dynamic modes of atomic force microscopy using a 3D finite element model. Ultramicroscopy **106**: 847-873.

Strijbos, S. (1976). Friction between a powder compact and a metal wall. Science of Ceramics **8**: 415-427.

Ultra Hard Materials Website. (2006). http://www.ultrahardmaterials.co.uk.

Veeco Website. (2006). http://www.veeco.com.

Veeco Probes Website. (2007). https://www.veecoprobes.com/.

Vishay Website. (2006). http://www.vishay.com.

Wikman, B., Solimanjad, N., et al. (2000). Wall friction coefficient estimation through modelling of powder die pressing experiment. Powder Metallurgy **43**(2): 132-138

Wu, C.Y., Cocks, A.C.F. (2004). Flow behaviour of powders during die filling. Powder Metallurgy **47**(2): 127-136.

Wu, C.Y., Ruddy, O.M., et al. (2005). Modelling the mechanical behaviour of pharmaceutical powders during compaction. Powder Technology **152**: 107-117

Zwick Website. (2006). http://www.zwick.co.uk.

APPENDIX

A.1 PRESS CONTROL STABLISATION

The stablisation of press control was required prior to undergoing the experiments to ensure smooth compression.

The control parameters are itemised below in Table A.1.1.

Powders	Normal Forces (N)	Holding Time (s)	P-portion force control steps	Compaction rate for all steps (N/s)
OFHC Cu	250	60	0.6	500
	500	60	0.5	750
	750	60	0.4	750
	1000	60	0.3	750
316L	250	60	0.6	250
	500	60	0.3	500
	750	60	0.2	500
	1000	60	0.1	500
Salt			Same configuration as 316L	
Sugar			Same configuration as OFHC Cu	
Alumina			Same configuration as OFHC Cu	

Table A.1.1 Parameters for Control Stabilisation Experiments

A.2 AFM EXPERIMENTS

A.2.1 Introduction

Atomic Force Microscopy (AFM) is a versatile tool for investigating local mechanical properties. AFM can function both as an imaging device and force sensor with nanometre resolution. It generates a topographical image by systematically moving a tip, fixed at the end of a cantilever, across the target surface. As the tip scans the surface, a force occurs between the tip and the surface, which causes the cantilever to bend. This deflection of the cantilever is captured by a laser light reflected from the gold-coated plate on the back of the cantilever. The reflected laser beam is admitted to a position sensitive photodiode (PSPD), which can measure changes in position of the incident laser as small as 1 nm (Figure A.2.1).

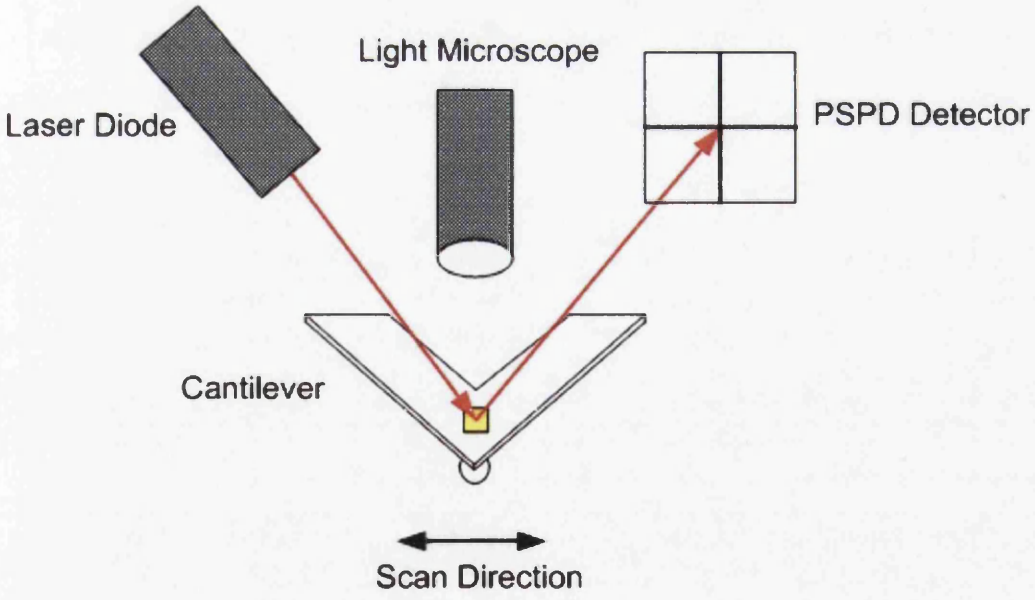

Figure A.2.1 Schematic Representation of AFM Measurement [Bowen and Wright, 2001]

The deflection of the cantilever subjected to force in the normal and lateral direction is captured by the PSPD detector then it can be analysed as seen from Figure A.2.2 below.

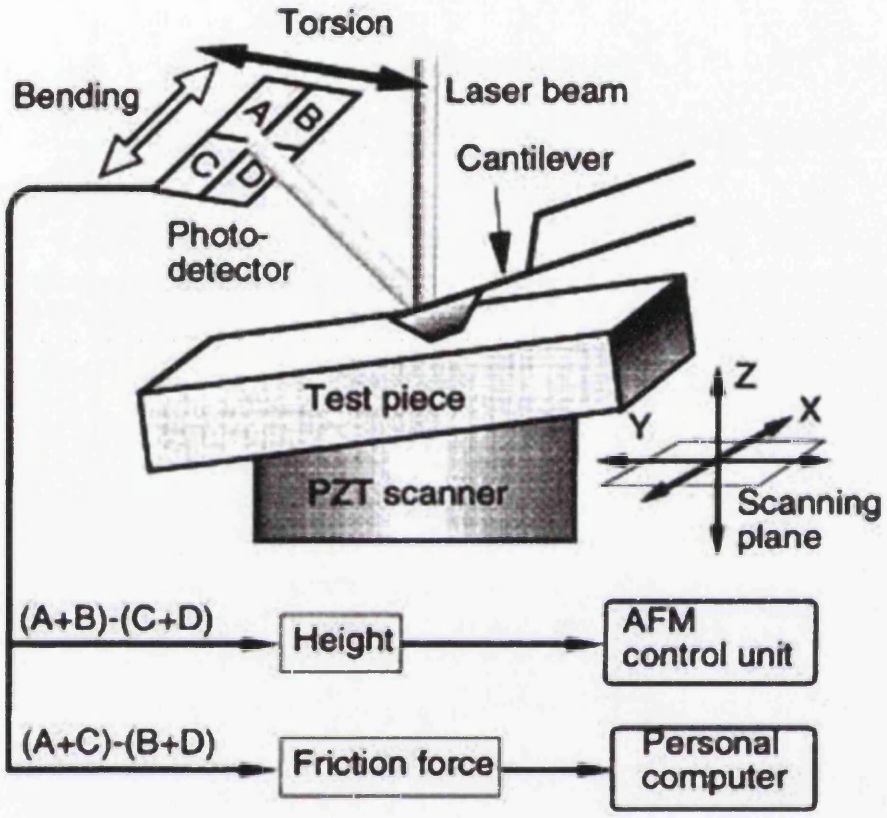

Figure A.2.2 Schematic Diagram of AFM for Normal and Frictional Force [Ando, 2000]

A.2.2 Experiment

The experiments were performed on two sets of different occasions at different locations, both using Veeco Model Dimension 3100 AFM [Veeco website, 2006].

Cantilevers and Tips

The geometry of cantilevers used in the experiments was reported in Figure 4.1 and 4.24 (for the two experiments respectively) with the material properties in Table 4.1. All of the cantilevers were from [Veeco Probes Website, 2007].

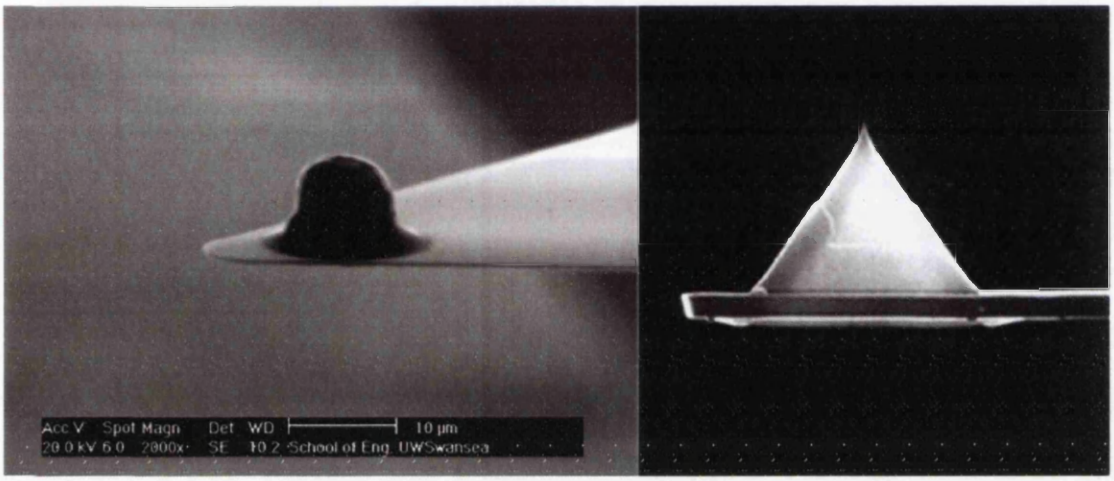

(a) (b)

Figure A.2.3 (a) Image Taken with Scanning Electron Microscopy (SEM) for Colloid Probe and (b) Image of Cone Shaped tip from [Veeco Probes Website, 2007]

For the first set of experiments, a tipless cantilever was used to enable a particle to be attached separately, where for the verification experiment, a cantilever with cone shaped tip, commercially available, was used.

The two ductile powders used in macro scale experiment (Chapter 3), i.e. 316L and OFHC Cu were chosen to be used as a colloid probe and silicon nitride tip for the next experiment.

Target Surfaces

Some of the target surfaces (Ra = 0.25 and 1.0 μm) shown in Chapter 3 (Figure 3.13) were used for the colloid probe tip and a silica surface (smooth) for the cone tip.

A.2.3 Results

Prior to exploring the results, the experimental procedure will be discussed.

In order to prepare a cantilever with a colloid probe tip, a bed of powders was spread on a microscope slide. Then using the microscope a particle was chosen and imaged (to measure its size) for the tip. The cantilever was lowered to apply fixity at the end and then the selected particle was fixed. Finally, it was left under ultra violet light to dry. For the cone shaped tip, cantilever preparation procedure is not required.

Once the cantilever was ready, it was mounted to the AFM apparatus. The calibration of the laser deflection was required for every experiment to ensure the PSPD accuracy. The AFM programme was started by the software Nanoscope [Veeco Website, 2006], where the tip was lowered until it was in contact with the surface and then normal and lateral scanning was performed as defined by the software.

The output from the AFM experiment was in units of volts (V) and this was representing the deflection of the cantilever. However, since the voltage output should be converted, generation of a force curve for normal force measurement was required. The force curve involved the repetition of approach and retraction of the cantilever where its slopes give the relationship between volts and nanometers.

Lateral force calibration is less straightforward to achieve an absolute measure of force and no well defined procedure exists for a commercial scanning device. However, the AFM is capable of providing an output that is an indicator of lateral load, which may be used for example as a comparator. The work in [Ogletree, 1996] suggests that performing a hysteresis scan can be used to calibrate and the practicality of doing this is explored in this appendix.

First, experimental results with a standard cantilever tip were explored for verification purposes.

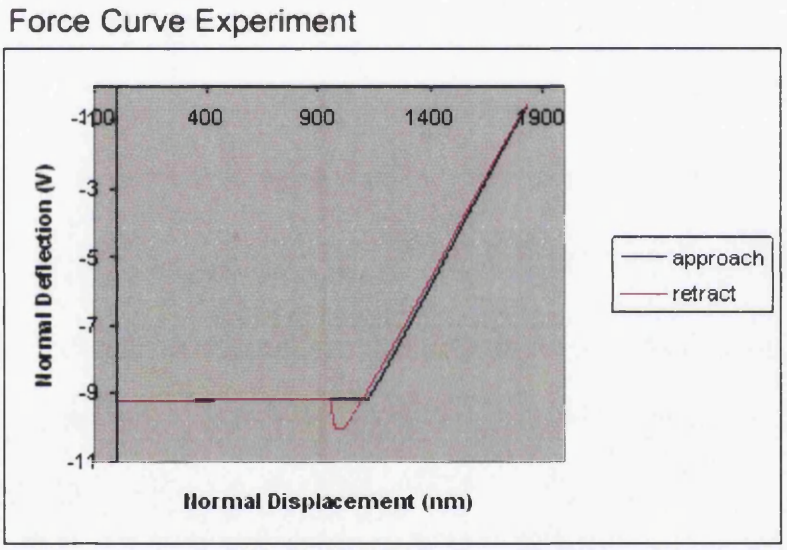

Figure A.2.4 Graph of Displacement against Deflection in Normal Direction for Force Curve Experiment (Standard Tip)

The result of the force curve experiment is shown in Figure A.2.4, where linear increase in normal deflection was observed. An adhesion force can be seen in the retraction stage. The behaviour shown in Figure A.2.4 agrees very well with the reported behaviour of adhesion study [Bowen, 2001]. From the slope of linear increase the relationship between voltage output and displacement can be deduced, leading to a sensitivity of 0.0125 V/nm.

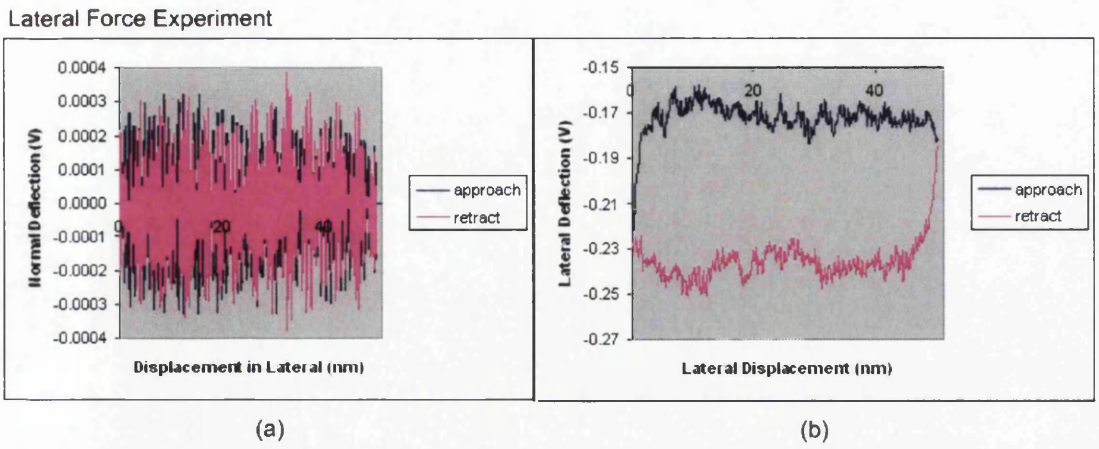

Figure A.2.5 Graphs from Lateral Force Experiment with (a) Normal and (b) Lateral Deflection against Lateral Displacement with Standard Tip

Figure A.2.5 shows results form a standard conical tip. The figures show the deflection in the normal and lateral direction respectively for the LFM experiment as the probe is moved laterally over the target surface and a clear friction loop was observed in (b). From the slope section in the friction loop, the sensitivity of the detector can be found at approximately 0.0294 V/nm. However, calculation using these sensitivities and using the data derived from the lateral force experiments suggests that the lateral deflection was significantly greater than the normal. Additionally, the normal deflection exhibited fluctuation during scanning in the lateral direction, and these showed similar magnitude but in the opposite direction. This seems to be due to very low normal load being applied, as the normal deflection level was very low compared with the lateral counterpart.

For the cantilever with the particle tip, experiments were performed with 316L and OFHC Cu particles used to form the colloid probe scanning over surfaces of Ra = 0.25 and 1.0 μm in the transverse direction. The diameter of the particles chosen for the experiment was in range of 7.5 – 50μm.

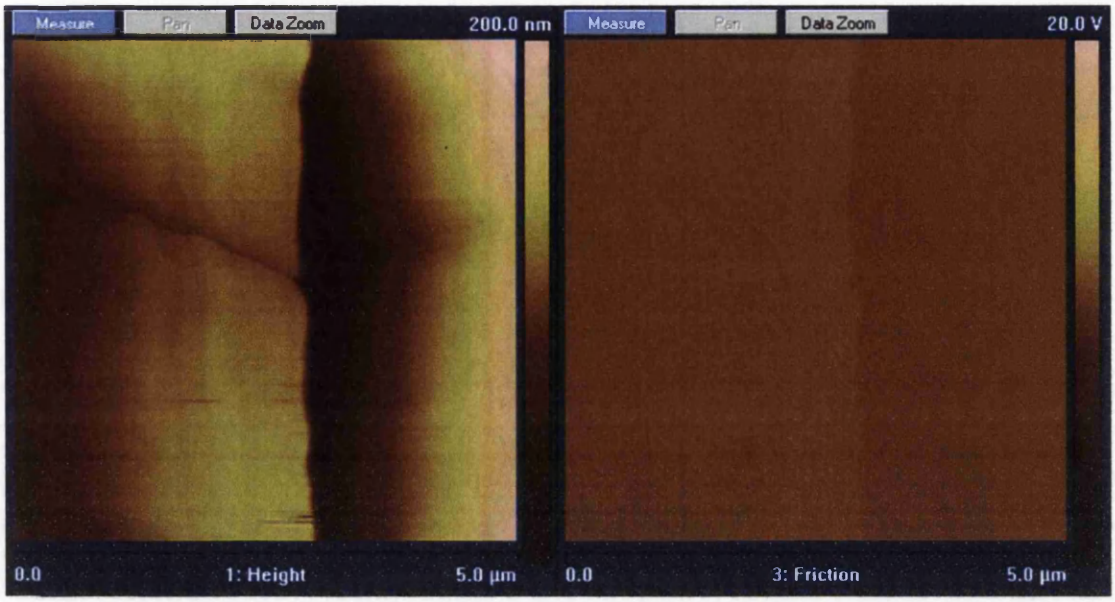

Figure A.2.6 Contours of Height and Lateral Force for OFHC Cu Probe (9µm Diameter) against Ra=0.25µm Surface (Left to Right Respectively)

Figure A.2.6 shows contours of the topographical ('height') and lateral deflection ('friction') data. It can be seen that the frictional response reflects the pattern of the topography.

For the topography above (Figure A.2.6), the LFM results are shown below in Figure A.2.7.

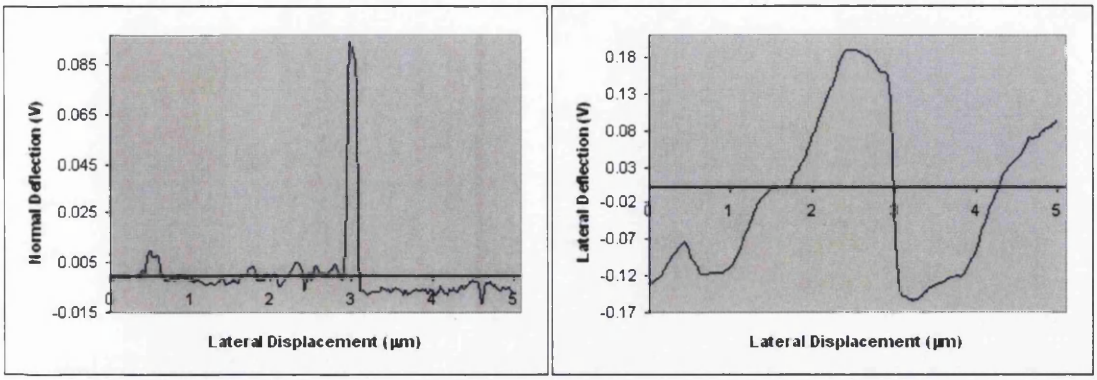

(a) (b)

Figure A.2.7 Graphs from Lateral Force Experiment with (a) Normal and (b) Lateral Deflection against Lateral Displacement with Colloid Probe Tip (OFHC Cu Probe (9µm Diameter) against Ra=0.25µm Surface)

By comparing the graphs with the topographical image in Figure A.2.6(a), the normal deflection (shown inverted) captures the surface topography. Although the deflection signals seem to reflect the topographical effects, difficulties were encountered in obtaining a friction loop. This was then investigated more fully and was traced to the preparation of the colloid probe tip.

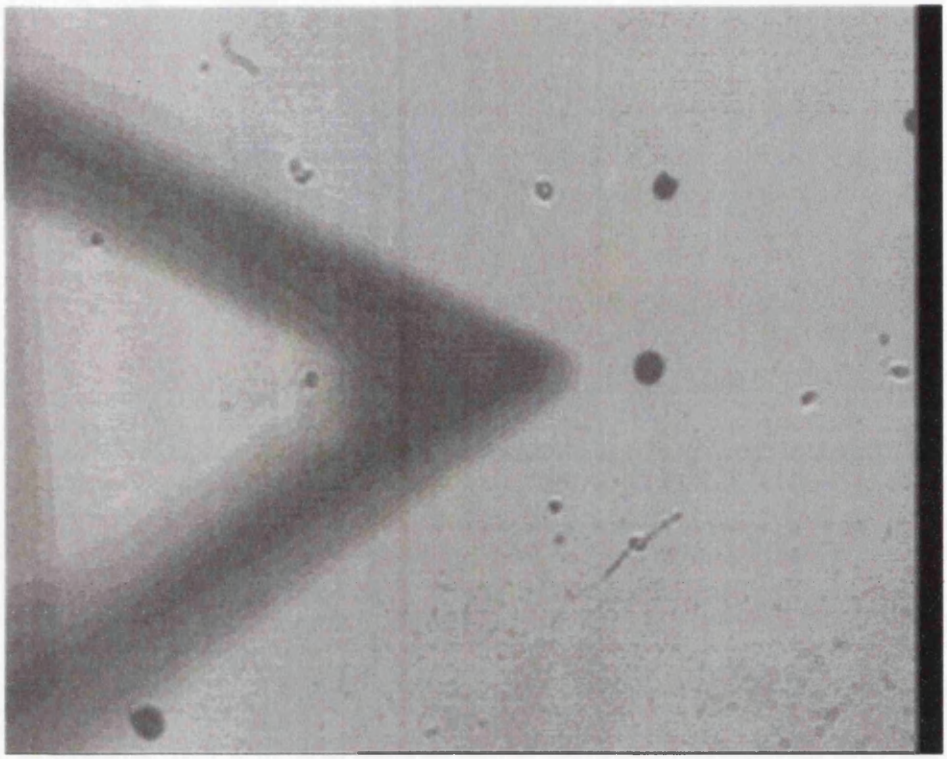

Figure A.2.8 Image of the Colloid Probe Selection Process

Figure A.2.8 shows the cantilever on top of the particle bed during the selection for the probe tip. In order to make a successful selection, the particle should have some space around (for easy pick up) and be as spherical as possible. The image shows that the view was restricted in the normal direction, and therefore some difficulties exist in choosing a spherical particle and further attaching it to the cantilever tip.

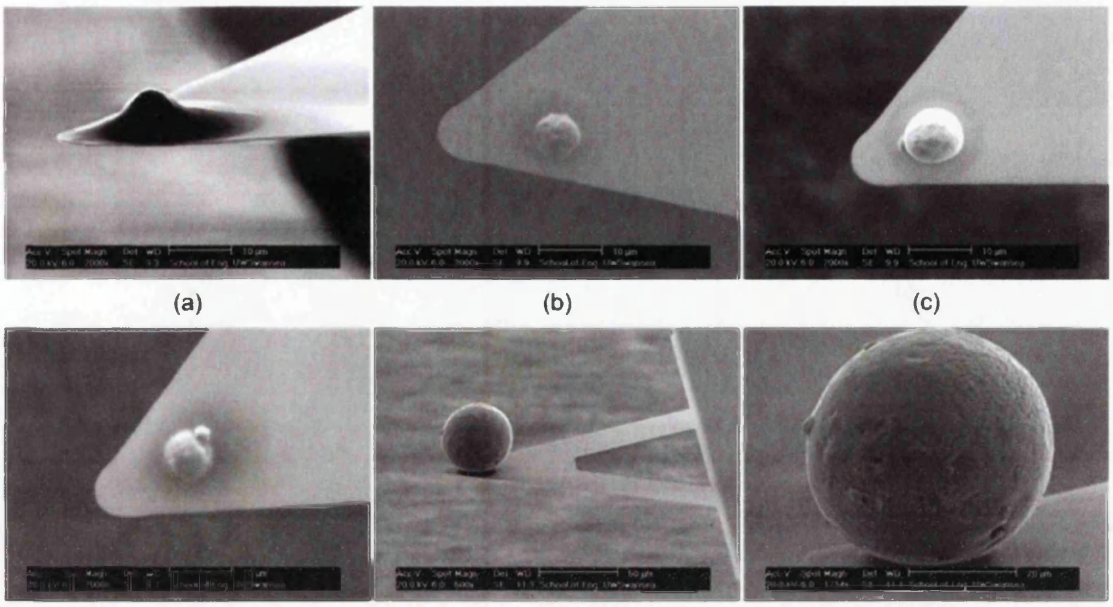

Figure A.2.9 SEM Images Taken for Colloid Probe Tip with (a) Overuse of Adhesive (b) Wrong Position (c) Imperfect Particle Shape (d) Clustered Particles (e) and (f) Large Particle

Figure A.2.9 shows SEM images of prepared tips, illustrating the various difficulties encountered while attempting to prepare a colloid probe. These included the amount of adhesive applied, positioning of the particle, particle not being perfectly spherical, particle being a cluster, and size of the particle. Each of these issues are likely to significantly affect the outcome producing inaccurate results. Additionally, taking SEM images requires fixing the fragile and sensitive cantilever on the test bed and detaching it afterwards, which may damage it and therefore had to be performed after the experiment.

These examples highlight the difficulties associated with attaching a particle to the cantilever tip and it is unlikely that a 'perfect colloid probe' may be manufactured easily. This, a potential route for data processing from these probes is to use simulation to assist with results interpretation and this motivated the work that is described in Chapter 4.